UNIVERSITY OF CALIFORNIA

Los Angeles

Modification of spontaneous emission in photonic crystals

A dissertation submitted in partial satisfaction of the

requirements for the degree Doctor of Philosophy

in Physics

by

Mikhail Boroditsky

1999

The dissertation of Mikhail Boroditsky is approved.

_____

Steven Kivelson

_____

Karoly Holczer

_____

Eli Yablonovitch, Committee Co-Chair

_____

Stuart Brown, Committee Co-Chair

University of California, Los Angeles

1999

Table of Contents

Table of Figures

Figures to Appendices:

Acknowledgements

The author is very grateful to everyone he worked with during this project and discussed its various aspects. Special thanks to Roberto Coccioli for help with computer simulations, Thomas Krauss for nanofabrication, and Rutger Vrijen for help in measurements. Different stages of this work were supported by ARO, NSF, and Hewlett-Packard MICRO grants.

VITA

10/09/68	**Born**
03/93	**M.S. in Physics, St. Petersburg Technical University**
12/96	**M.S. in Physics, University of California Los Angeles**
10/94-04/96	**Teaching Associate**
10/94-12/98	**Graduate Research Assistant,**
	University of California Los Angeles

Publications and Presentations

M. Boroditsky, R. Ragan, E. Yablonovitch, "Absorption enhancement in Ultra-thin textured AlGaAs films", to be published in Solar Energy and Solar Cell Materials.

M. Boroditsky, R. Coccioli, E. Yablonovitch, “Analysis of photonic crystals for light-emitting diodes using the finite difference time domain technique”, Proceedings of Photonics West ’98, San Jose, CA, Jan 20-24, 1998 (in print)

M. Boroditsky, E. Yablonovitch, ”Spontaneous Emission Engineering in Light Emitting Diodes”, Proceedings of LEOS ’97, **2**, p 7.

M. Boroditsky, E. Yablonovitch, “Photonic Crystals Boost Light Emission”, Physics World, July 1997, p.53.

M. Boroditsky, E. Yablonovitch, “Light extraction efficiency from light-emitting diodes”, SPIE, **3002** (1997), p.119-22.

M. Boroditsky, E. Yablonovitch “Light extraction efficiency from visible light-emitting diodes”, Conference on Lasers and Electro-Optics, Technical Digest Series, **9** (1996), p.141-2.

M.L.Boroditsky, A.E.Dul`kin, I.V.Kochnev, D.A.Livshits, N.O.Sokolova, E.U.Rafailov, I.S.Tarasov, Yu.M.Shernyakov, B.S.Yavich. “High Power Single-Mode InGaAsP/GaAs Lasers (λ=0.98mm) MOCVD grown,” Pis`ma v ZhTF, **20**(6), pp.62-66 (1994).

M.L.Boroditsky, D.Z.Garbuzov, A.Y.Gorbachov, N.D.Ilinskaya, D.A.Livshits, D.N.Marinsky, E.U.Rafailov, A.L.Stankevich, I.S.Tarasov. “High Power Single-Mode Buried InGaAsP/GaAs SC DHS Lasers,” Pis`ma v ZhTF, **19**(21), pp.78-81 (1993).

M.L.Boroditsky, D.Z.Garbuzov, D.A.Livshits, E.U.Rafailov, “Mode composition control in high power buried InGaAsP/GaAslasers”, SPIE's OE/LASE '94, January 22-29, 1994, Los-Angeles.

R. Coccioli, M. Boroditsky, K. Kim, Y. Rahmat-Samii, E. Yablonovitch, “What is the Smallest Possible Electromagnetic Mode Volume in a Dielectric Cavity?” to be published in IEE Proceedings – Optoelectronics, January 1999.

R. Coccioli, M. Boroditsky, E. Yablonovitch, T. Itoh, “Planar Geometry Electromagnetic Crystals for Optical and Millimeter-Wave Applications” (invited) International workshop on Contemporary Photonic Technology, January 12-14, 1999, Sendai Japan.

D. Garbuzov, G.-J. Shiau, V. Bulovic, M. Boroditsky, C.-P. Chao, S.R. Forrest, “Photoluminescence study of excess carrier spillover in 1.3 μm wavelength strained multi-quantum-well InGaAsP/InP laser structures,” Applied Physics Letters, **66**, (1995), p.1307.

D.Z.Garbuzov, M.L.Boroditsky, N.D.Il'inskaya, D.A.Livshits, D.N.Marinskiy, E.U.Rafailov, “Controlling the mode composition of high-power buried InGaAsP/GaAs lasers with a wavelength of 0.8μm,” Semiconductors **28**(2), pp.191-194 (1994).

T. Krauss, M. Boroditsky, R. Coccioli, O. Painter, A. Scherer and E. Yablonovitch, "Photonic crystal microcavity enhanced LEDs", CLEO/Europe, Paper CWA4, Glasgow, September 1998.

ABSTRACT OF THE DISSERTATION

Modification of spontaneous emission in photonic crystals

by

Mikhail Boroditsky

Doctor of Philosophy in Physics

University of California, Los Angeles, 1999

Professor Eli Yablonovitch, Co-chair

Professor Stewart Brown, Co-Chair

The modification of spontaneous emission in a semiconductor photonic crystal and in a semiconductor microcavity at room temperature is the subject of this thesis. The broad spectral linewidth of semiconductors together with large surface recombination velocities make the observation of these effects an interesting and challenging task.

A quantum electrodynamical model is used to estimate enhancement of spontaneous radiation rates in photonic crystals and microcavities. Extensive numerical computations were employed to calculate the band structure of thin slab photonic crystals and the properties of microcavities. The minimal achievable effective mode volume, a

crucial parameter for cavity enhancement of spontaneous emission was shown to be $\approx 2(\lambda/2n)^3$ where λ is the resonant wavelength and n is the refractive index. Five-fold enhancement of spontaneous emission was shown to be physically possible in InGaAs nanocavities.

Photoluminescence measurements of surface recombination velocity were used in the search of material system most suitable for fabrication of such a photonic crystal. The InGaAs and InGaN material systems were shown to be good candidates for luminescent photonic bandgap structures.

Angular resolved photoluminescence measurements were used to experimentally measure the band structure of so-called electromagnetic conduction bands of such a photonic crystal.

The enhancement of spontaneous emission extraction from a thin slab photonic crystal was demonstrated. It was shown that emission into the leaky bands of the photonic crystal has the same benefit as cavity-enhanced spontaneous emission, provided these bands are flat enough relatively to the spectral emission bandwidth of the material. Recommendations for novel LED designs were worked out based on the results of this study.

1. Introduction

For a long time the spontaneous emission rates were believed to be an intrinsic property of a material. It was later understood that spontaneous emission also depends strongly on the surrounding environment through the density of states and local strength of the electromagnetic modes[1]. First works on enhancement and suppression of spontaneous emission in the microwave regime were performed in 1980's by Haroche and Kleppner[2].

It was predicted by Purcell[3] that an atom in a wavelength-size cavity can radiate much faster than in the free space. This effect was measured in a cavity formed by two parallel mirrors by Haroche *et al.*[4]. All these measurements were performed on single atoms. A similar effect can be observed in semiconductor materials, even though a smallest chunk of the semiconductor we can imagine consists of thousands of atoms. Enhancement of the spontaneous emission rate was recently observed at low temperature in Vertcal Cavity Surface Emittin Laser (VCSEL) structures of small lateral dimensions[5].

Photonic crystals, artificially created, multi-dimensionally periodic structures are known for a forbidden electromagnetic bandgap. For that reason, they can be used to modify spontaneous emission. Initially, it was proposed to use photonic crystals to inhibit spontaneous emission[6], but they can be employed to enhance it as well.

Modification of spontaneous emission in photonic crystal and enhancement of spontaneous emission in a semiconductor microcavity making use of photonic crystal at room temperature is the subject of this thesis.

In the second chapter the quantum theory of spontaneous emission will be presented. The behavior of an atom in a cavity will be discussed, and Purcell's enhancement factor will be re-derived for the particular case of the quantum well active material in a microcavity.

Electromagnetic simulations of photonic bandgap materials will be discussed in the third chapter including band structure calculations and the study of defect modes. Enhancement of the spontaneous emission rate in the resonant mode of a microcavity is inversely proportional to the volume occupied by this mode. This makes cavity optimization an important part of this project, requiring extensive numerical work. It will be shown that a single-mode nanocavity can be built with semiconductor material with cavity volume as low as $\approx 2(\lambda/2n)^3$, where n is the refractive index of the semiconductor, and λ is the resonant wavelength.

Observation of spontaneous emission from such cavities require relatively low non-radiative surface recombination. Identification of suitable material systems using photoluminescence measurements on samples with exposed edges is described in detail in the fourth chapter.

Chapter five of the thesis is about photoluminescence from photonic crystals without nanocavities. The relative frequency of the photonic and electron bandgap is shown to change the photoluminescence spectrum and directionality of the spontaneous emission from the sample compared to an unetched reference sample.

The results of photoluminescence measurements on thin film photonic crystal will be presented in the chapter five. In this way, the band structure of the photonic crystal can be directly measured.

Enhancement of spontaneous emission from the nanocavities is of considerable practical interest. Indeed, Light-Emitting Diodes (LED's) are a class of opto-electronic devices based on spontaneous electron-hole recombination in semiconductors. The biggest problem in design of such a device is the difficulty of extracting light from the high-refractive index material. The principle of resonant-cavity enhancement can be used to enhance light emission. The use of one-dimensional Distributed Bragg Reflectors to realize high efficiency planar microcavity LEDs was proposed by F. Schubert *et al*.[7], and was most successfully realized by De Neve *et al.*[8]. However, only three-dimensional cavities can provide a really significant improvement in the light extraction. We will show in chapter five that even though a five-fold spontaneous emission enhancement is possible in a 3-d nanocavity, a similar enhancement can be obtained from a thin slab photonic crystal, if the spontaneous emission from the active material is tuned to the leaky conduction bands of the photonic crystal.

Thin film photonic crystals are also a possible tool for efficient light extraction. We studied the external scattering of guided waves by photonic crystal and their potential application in the light-emitting diodes in the chapter six.

2. Theory

2.1. Two-level systems

Spontaneous recombination in semiconductors is a complicated process. The consideration of a simple two level system gives many good insights into this process. Downward transition in a simple two-level system can be spontaneous or stimulated. It is easy to see that spontaneous emission accounts for most of the radiative recombination in thermal equilibrium at room temperature. Indeed, the detailed balance for such a system is:

$$\dot{N}_1 = -B_{12}N_1\rho(\omega_0) + B_{21}N_2\rho(\omega_0) + A_{21}N_2 = 0\,. \qquad (1)$$

A_{12} and B_{21} and are Einstein's coefficients and ρ(ω) is the density of electromagnetic modes.

Using $B_{12}=B_{21}$ and $\frac{N_1}{N_2} = e^{-\hbar\omega/T}$ we get

$$\frac{\text{Stimulated}}{\text{Spontaneous}} = \frac{B_{21}N_2\rho(\omega_0)}{A_{21}N_2} = \frac{1}{e^{\hbar\omega/T}-1} \sim e^{-30}, \qquad (2)$$

with kT=0.27eV and hω=1eV. So the world we live in is mostly the world of spontaneous emission and it is interesting to see if we can tailor the properties of this process according to our needs.

2.2. Quantization of the electromagnetic field

Quantization of the electromagnetic field is necessary for a correct understanding of the nature or spontaneous emission and its engineering. The quantization procedure in

the case of a media with a non-uniform distribution of the dielectric constant ε(r) is the same as for the free space, but the vector potential operator A(r,t) does not consist of plane waves anymore.

The classical Maxwell equations

$$\begin{aligned} &\nabla \cdot \vec{B} = 0 \\ &\nabla \cdot (\varepsilon(\vec{r})\vec{E}(\vec{r})) = 0 \\ &\nabla \times \vec{E} + \frac{1}{c}\frac{\partial \vec{B}}{\partial t} = 0 \\ &\nabla \times \partial\vec{B} - \frac{1}{c}\frac{\partial \vec{E}}{\partial t} = 0 \end{aligned} \qquad (3)$$

can be transformed by introduction of a vector-potential $\vec{A}$ such that $\vec{E} = -\frac{1}{c}\frac{\partial \vec{A}}{\partial t}$ and $\vec{B} = \nabla \times \vec{A}$. It yields the wave equation in the form of

$$\nabla(\nabla\vec{A}) - \nabla\vec{A} - k^2\varepsilon\vec{A} = 0 \qquad (4)$$

In the case of the uniform dielectric constant, its solutions are plane waves, however, these solutions can be quite complicated function in the arbitrary cases. Nonetheless, the canonical quantization procedure still can be applied by the introduction of operators satisfying the commutation relations.

Then, the operator of the vector-potential for a given mode becomes

$$\vec{A}(\vec{r},t) = \left(\frac{2\pi c^2\hbar}{\omega}\right)^{1/2}[a(t)\vec{A}_0(\vec{r}) + a^+(t)\vec{A}_0^*(\vec{r})] \qquad (5)$$

where operators a(t) and $a^+(t)$ are photon annihilation and creation operators correspondingly, and $A_0(r)$ describes the spatial distribution of the classical eigenmode of

frequency ω. Operators of electric and magnetic fields are readily derived from the definition of A(r,t):

$$\begin{aligned}\vec{E}(\vec{r},t) &= i\left(2\pi\hbar\omega\right)^{1/2}[a(t)A_0(\vec{r}) - c.c.] \\ \vec{B}(\vec{r},t) &= \nabla\times\vec{A}_0(\vec{r})\end{aligned}. \qquad (6)$$

Obviously, for any state with n photons the diagonal matrix elements of the electromagnetic field operators are equal to zero:

$$\left\langle n\left|\vec{E}(\vec{r})\right|n\right\rangle = \left\langle n\left|\vec{B}(\vec{r})\right|n\right\rangle = 0 \qquad (7)$$

While diagonal matrix elements of the square of the electric field is

$$\left\langle n\left|\vec{E}^{\,2}(\vec{r})\right|n\right\rangle = 4\pi\hbar\omega\left|\vec{A}_0(\vec{r})\right|^2(n+1/2), \qquad (8)$$

and can be rewritten as a sum of a classical part, corresponding to n photons in the mode and a purely quantum mechanical contribution, called also zero-point fluctuations of the field:

$$\left\langle n\left|\vec{E}^{\,2}(\vec{r})\right|n\right\rangle = 4\pi\hbar\omega\left|\vec{A}_0(\vec{r})\right|^2 n + \left\langle\vec{E}^{\,2}(\vec{r})\right\rangle_0. \qquad (9)$$

That means that even when the system is in the state with no photons, the net mean square fluctuations of the electric field are not zero.

The Hamiltonian H_F of the electromagnetic field becomes that of a harmonic oscillator after we plug Eq (6) into $H = \frac{1}{8\pi}(EE^+ + HH^+)$:

$$H_F = \hbar\omega(a^+a + 1/2). \qquad (10)$$

If we work with a classical multi-mode system, its quantum Hamiltonian is just a sum over allowed electromagnetic modes, including the polarization:

$$\vec{A}(r,t) = \sum_n \left(\frac{2\pi c^2 \hbar}{\omega} \right)^{1/2} [a(t)\vec{A}_n(r) + a^+(t)\vec{A}_n^*(r)] \qquad (11)$$

In this way the Hamiltonian of the field becomes a sum of the photon energy in all modes. Importantly, from the viewpoint of spontaneous emission, even when the average electric field is zero when there are no photons in the mode, the mean square of the electric field is not zero but equals to $\langle n|\vec{E}^2(\vec{r})|n\rangle = \frac{1}{2} 4\pi\hbar\omega \left|\vec{A}_0(r)\right|^2$. That is we can say that fluctuations in the mean square of the field are distributed in the same way as the classical field.

Many important features of spontaneous emission in semiconductors can be obtained from the analysis of a two level system coupled to one or many electromagnetic mode(s). For a single mode system:

$$H = \tfrac{1}{2}\hbar\omega_0\sigma_z + \hbar\omega a^+ a + i\hbar C[a + a^+][\sigma - \sigma^+], \qquad (12)$$

The coupling constant $C = \omega_0 \left(\frac{2\pi}{\hbar\omega V} \right)^{1/2} \left| e\vec{x}_{12} \cdot \hat{\mathrm{E}} \right| \approx \left(\frac{2\pi}{\hbar\omega V} \right)^{1/2} \left| \vec{d}_{12} \right|$ is Rabi frequency and it sets an important time scale in the atom-light interaction.

For the near-resonant interactions, the rotating wave approximation can be used. The higher order terms (the ones that do not explicitly preserve the energy of the system) are omitted and the Hamiltonian can then be diagonalized:

$$H = \tfrac{1}{2}\hbar\omega_0\sigma_z + \hbar\omega a^+ a + i\hbar C[a^+\sigma - a\sigma^+], \qquad (13)$$

The solution for the simplest case when $\omega=\omega_0$ is so-called vacuum Rabi oscillations, that is a photon is emitted into the modes and then reabsorbed and re-emitted again.

When the atom is coupled to a continuum of modes, so that the interaction Hamiltonian is $H_{\text{int}} = \sum_{k,\lambda} i\hbar C_{k,\lambda}[a^{+}_{k,\lambda}\sigma - a_{k,\lambda}\sigma^{+}]$, then the exited state $|2\rangle|0,0,..,0\rangle$ shows exponential decay $P_2(t) = e^{-A_{21}t}$, where $A_{21} = \frac{4\omega_0^3\left|\vec{d}_{12}\right|^2}{3\hbar c^3}$, which is exactly the classical expression for the spontaneous emission rate. It's interesting to see that this emission rate can be found approximately from dimensional considerations as A_{21}~$C^2\rho(\omega)$.

For a dipole located at the arbitrary point *r* of the mode, the transition rate would be

$$A_{12}(\vec{r}) = \frac{4}{3}\frac{n|d|^2\omega^3}{\hbar c^3}\left|\vec{A}_0(r)\right|^2 V \qquad (14)$$

with normaization $\int \varepsilon(r)\left|\vec{A}_0(r)\right|^2 d^3r = 1$.

Placing an atom in a lossy (leaking or absorbing) cavity can produce different effect on the spontaneous emission process. The cavity by itself brings in another time scale $\tau_{av} = \frac{Q}{\omega_0}$ describing the photon lifetime in the cavity, with Q being the quality factor of the cavity and ω_0 being its resonant frequency. Depending on the relation between the cavity lifetime, and the vacuum Rabi oscillations period in the same cavity without losses there can be two simple extreme cases:

$\tau >> t_R$ Damped Rabi oscillations

Leakage from the cavity is much slower then the Rabi oscillation so that the exponential decay is an envelope for the Rabi oscillations: $P_2 = e^{-\frac{Q}{\omega}t}\cos^2 C$

$\tau << t_R$ Overdamped cavity (E.Purcell, 1946)

This case is of special interest for us, so we will derive recombination rate below and then will apply the results to the semiconductor's emission in order to estimate the maximum achievable spontaneous emission enhancement in a dielectric microcavity.

2.3. Purcell effect

The Purcell enhancement factor[2] needs to be modified when considering generation of light in semiconductor quantum well (QW) structures.

The classical electric field of the cavity mode $\mathbf{E}(\mathbf{r})$ has to be normalized $\mathbf{E} \to \alpha\mathbf{E}$ with the normalization factor α so that

$$\frac{1}{4\pi}\int \varepsilon(\mathbf{r})\left(\alpha\mathbf{E}(\mathbf{r})\right)^2 d^3\mathbf{r} = \frac{\hbar\omega_0}{2}, \qquad (15)$$

where ε is the material dielectric constant and ω_0 is the resonant frequency of the cavity. This gives the normalization factor

$$\alpha^2 = \frac{2\pi\hbar\omega_0}{\int \varepsilon(\mathbf{r})\mathbf{E}^2(\mathbf{r})d^3\mathbf{r}} \qquad (16)$$

In the above equations the integration extends over the quantization volume. The spontaneous emission rate at frequency ω, into the resonant mode cantered at ω_0, at a given point **r**, follows from Fermi's golden rule and equals to

$$\Gamma(\mathbf{r}) = \frac{2\pi}{\hbar}\left\langle\left(\mathbf{d}\cdot\alpha\mathbf{E}(\mathbf{r})\right)\right\rangle^2 \frac{\Delta\omega g}{2\pi\hbar((\omega-\omega_0)^2 + (\Delta\omega/2)^2)}, \qquad (17)$$

where **d** denotes the atomic moment dipole, $\Delta\omega$ is the cavity linewidth, and g is the degeneracy of the cavity mode. The last term in Equation (17) represents the Lorentzian lineshape of electromagnetic modes – there are g modes in the frequency range $\Delta\omega$. The dot product ($\mathbf{d}\cdot\alpha\mathbf{E}(\mathbf{r})$) has to be averaged over the possible orientations of the atomic dipole moment. At this point we need to take the specific account of optical transition in semiconductor quantum wells. First, electron-heavy hole transitions are the major contributor to the spontaneous emission. Second, these transitions are only allowed if the dipole moment of the transition lies in the plane of the quantum well, so that $<d_x^2>=<d_y^2>=\mathbf{d}^2/2$, $<d_z^2>=0$. Then, if the mode's electric field is also in the QW plane, as happens for TE modes, the average $\left\langle\left(\mathbf{d}\cdot\alpha\mathbf{E}(\mathbf{r})\right)\right\rangle^2 = (1/2)\mathbf{d}^2(\alpha\mathbf{E}(\mathbf{r}))^2$. Note that in the case of bulk semiconductor, or for interaction with random modes, the pre-factor above would have been 1/3.

If the active material is placed in the point of maximum electric field of the mode, the emission rate is

$$\Gamma = \frac{2\pi}{\hbar}\frac{\mathbf{d}^2}{2}\left(\alpha\mathbf{E}_{\max}\right)^2 \frac{\Delta\omega g}{2\pi\hbar((\omega-\omega_0)^2+(\Delta\omega/2)^2)} \qquad (18)$$

If the linewidth of the cavity $\Delta\omega$ is much smaller than emission spectrum width of the active material $\Delta\omega_m$, integration over the frequencies leads to

$$\Gamma = \frac{2\pi}{\hbar}\frac{\mathbf{d}^2}{2}\left(\alpha\mathbf{E}_{\max}\right)^2 \frac{g}{\hbar\Delta\omega_m} \qquad (19)$$

Plugging in the value of the normalization factor α^2 gives

$$\Gamma = \frac{\omega_0}{\Delta\omega_m}\frac{2g\pi^2\mathbf{d}^2}{\hbar}\frac{\mathbf{E}_{\max}^2}{\int\varepsilon(\mathbf{r})\mathbf{E}^2(\mathbf{r})d^3\mathbf{r}} \tag{20}$$

The unenhanced spontaneous emission rate in the bulk can be calculated using the classical formula[9]

$$\Gamma_0 = \frac{4n\mathbf{d}^2\omega^3}{3\hbar c^3} = \frac{4n\mathbf{d}^2 8\pi^3}{3\hbar\lambda^3} \tag{21}$$

Thus, the overall enhancement factor, which can be used as a figure of merit for optimization of a resonant-cavity structure becomes

$$\frac{\Gamma}{\Gamma_0} = Q_m g\frac{3\lambda^3}{16\pi n}\frac{\mathbf{E}_{\max}^2}{\int\varepsilon(\mathbf{r})\mathbf{E}^2(\mathbf{r})d^3\mathbf{r}}, \tag{22}$$

where we call $Q_m = \frac{\omega_0}{\Delta\omega_m}$ is the material quality factor. Introducing the mode volume V_{eff}

$$V_{eff} = \frac{\int\varepsilon(\mathbf{r})\mathbf{E}^2(\mathbf{r})d^3\mathbf{r}}{\left(\varepsilon(\mathbf{r})\mathbf{E}^2(\mathbf{r})\right)_{\max}}, \tag{23}$$

the enhancement of spontaneous emission rate can be recast in the following form:

$$\frac{\Gamma}{\Gamma_0} = \frac{3Q_m g(\lambda/2n)^3}{2\pi V_{eff}} \tag{24}$$

This expression differs from the one originally derived by Purcell by a degeneracy factor g and a factor of $\pi/4$ which follows from integrating over the Lorentzian cavity lineshape, and polarization averaging in the quantum well structures.

It will be shown in chapter 5, surprisingly, that a plain photonic crystal without any nanocavities gives rise to the same effect. This requires weak dispersion of the photonic conduction bands, and their coupling of spontaneous emission to external plane waves.

3. Electromagnetic computations

The spontaneous emission rate of an atom can be increased or decreased by changing its environment. It has been known since 1946 that the enhancement of spontaneous emission rate, or Purcell effect, can be achieved in very tiny electromagnetic cavities[10]. It is tempting to apply the Purcell effect to the spontaneous emission of opto-electronic materials[11], such as III-IV semiconductors. Several examples has recently appeared: a five-fold increase in the radiative rate was demonstrated at low temperatures in VCSEL-type micro-cavities by Gerard *et al*[5]. Likewise, layered 1-dimensional Bragg micro-cavities increase the efficiency of planar light emitting diodes (LED's) as proposed by F. Schubert *et al*.[7], and most successfully realized by De Neve *et al*[8]. It was shown in the chapter 2 that the enhancement of spontaneous emission rate in a semiconductor nanocavity structure with a quantum well active region is:

$$\frac{\Gamma}{\Gamma_0} = \frac{3Qg(\lambda/2n)^3}{2\pi V_{eff}}, \tag{25}$$

where Q is the quality factor of the cavity, n is the refractive index of the semiconductor, λ is the mode's wavelength, g is the mode degeneracy factor, and V_{eff} is the mode volume defined as

$$V_{eff} = \frac{\int \varepsilon(\mathbf{r})\mathbf{E}^2(\mathbf{r})d^3\mathbf{r}}{\left(\varepsilon(\mathbf{r})\mathbf{E}^2(\mathbf{r})\right)_{\max}}. \tag{26}$$

The integration in Equation (26) is performed over the quantization volume.

It is possible to build a very high Q dielectric cavity using photonic crystals, but once the spectral width $\Delta\nu = \nu/Q$ of a resonant cavity is smaller than the spontaneous emission linedwidth $\Delta\nu_m$ there is no further significant increase in the spectrally integrated spontaneous emission rate. The normal spontaneous emission bandwidth of opto-electronic semiconductors at room temperature limits the useable cavity Q to Q>10 or Q>40 depending on the specific material. Looking at Equation (26), a significant enhancement of spontaneous emission rate in semiconductors at room temperature requires building the smallest possible electromagnetic cavities, or, in other words, reducing the effective volume V_{eff} . This makes the search for the smallest mode volume achievable with the dielectric material an important question. The value of $V_{eff}=2.55(\lambda/2n)^3$ was previously reported by Foresi *et al.*[12,13] for a 1-dimensional bridge photonic crystal. Is it possible to do better?

The minimal size of a dielectric cavity mode is the subject of this chapter. We have used the Finite Difference Time Domain (FDTD) method to compute the smallest achievable effective volume. The FDTD method has been chosen, among the many available, because of its capability to deal with complicated structures such as those analyzed here. Using different kinds of boundary conditions, the method allows one to deal with many different types of problems: computation of the dispersion diagram, computation of resonant frequency, effective mode volume, Q, and mode pattern in the nanocavity. FDTD was used by Sakoda[14] to study modal properties of defects in infinite 2D photonic crystals without considering mode volume. Indeed, the method proved to be very effective in this calculation because it provides a wealth of data from which it is possible

to derive all the quantities of interest for the design of nanocavities. The code implemented in our work has been extensively tested against data available in the literature. Using this valuable numerical tool, we will show that an effective volume as low as $V_{eff} \approx 2(\lambda/2n)^3$ is achievable. As a complementary result, Painter *et al.*[15] have demonstrated that very high Q≈4000 can be achieved in similar thin-slab PBG cavities at the price of slightly larger mode volume.

We have thoroughly analyzed numerous possible configurations of the dielectric cavity created by introduction of a defect into a 2-dimensional photonic crystal. Our baseline 2-D photonic crystal consisted of a thin slab with a triangular array of holes. Our choice of such a structure in Fig. 1(a) is justified by the following considerations: This type of 2-D photonic crystal structure shows a large bandgap for TE polarization, providing good horizontal confinement. Guided modes in such a structure are well confined vertically by the slab refractive index and total internal reflection, so the vertical dimension of the mode is small. This structure is much easier to fabricate at the optical wavelength scale than three-dimensional photonic crystals.

We have considered only donor modes, that is modes created by adding some extra material to the photonic crystal. In such donor mode cavities, the electromagnetic field tends to be concentrated in the regions where dielectric material has been added. For spontaneous emission there has to be a good overlap between the electromagnetic field and the semiconductor light emitter. Thus donor mode cavities are preferred. In all our computations we considered a thin semiconductor slab with refractive index 3.5 bonded on a glass substrate with refractive index 1.5.

In the following Section we will consider the problem of computing the dispersion diagram frequency, ν versus wave vector **k** of the structure shown in Figure 1(a). In Section 3 we will show how, by introducing a defect, we can create a nanocavity whose resonant frequency is in the forbidden gap of the photonic crystal structure. Conclusions are drawn in Section 4.

3.1. Numerical Results: Dispersion Diagram

Computation of the dispersion diagram of the photonic crystal shown in Figure 1(a) requires electromagnetic wave propagation in the infinite space, tiled with identical cells in the *xy*-plane. The solution of Maxwell's equations must satisfy Bloch periodic conditions:

$$\mathbf{E}(\mathbf{r}+\mathbf{a},t)=\mathbf{E}(\mathbf{r},t)e^{i\mathbf{k}\cdot\mathbf{a}} \qquad \mathbf{H}(\mathbf{r}+\mathbf{a},t)=\mathbf{H}(\mathbf{r},t)e^{i\mathbf{k}\cdot\mathbf{a}} \qquad (27)$$

with **a** standing for a primitive lattice vector, and **k** denoting the wave vector. At any instant of time, the phase shift $e^{i\mathbf{k}\cdot\mathbf{a}}$ is the only difference between the eigenmode's fields at corresponding points in different cells. Consequently, the computational domain for the analysis may be restricted to a single unit cell of the crystal, delimited by the constant coordinate surfaces $x=\pm a/2$, $y=0$, and $y=a\sqrt{3}/2$ (Fig. 1b). At those surfaces, the periodic Bloch boundary conditions (27) must be applied to the tangential component of the electric and magnetic fields, where now the lattice vector **a** connects corresponding points at the opposite sides of the unit cell. The thin dielectric film with a triangular lattice of holes (Fig. 1a), is infinite in the vertical direction. To simulate that, the

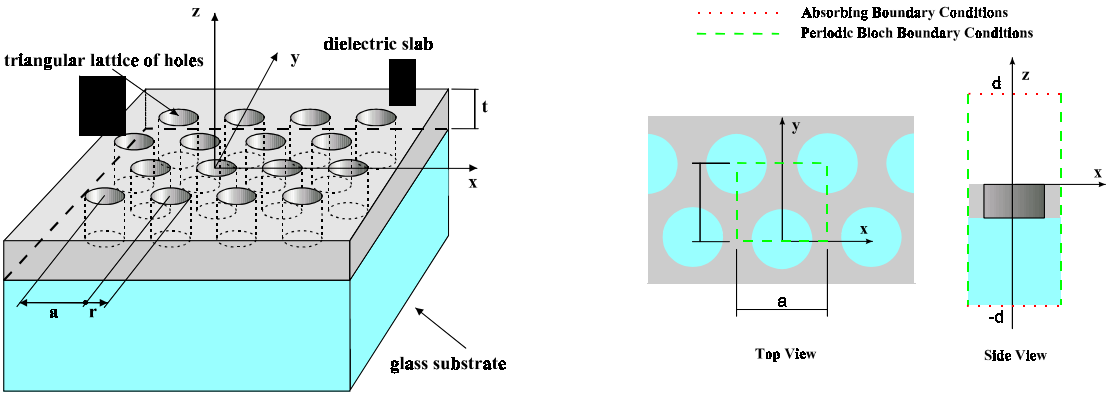

Figure 1. *(a)* A small section of an infinite dielectric slab with a triangular array of through holes resting on a glass substrate; *(b)* Unit cell used for the computation of the frequency ν vs. wave-vector **k** dispersion relationship of the infinite photonic crystal corresponding to (a).

computational domain shown in Fig. 1(b) is terminated using Absorbing Boundary Conditions (ABC) at the surfaces $z = \pm d$. Both Mur's first order boundary conditions[16] and Anisotropic Perfectly Matched Layer absorbing boundary conditions[17,18] (PML) have been used in this work.

The structure can be excited either with some initial electromagnetic field distribution or with one or mutiple arbitrarily oriented dipoles using a Gaussian pulse in time. If a localized source is used to excite the structure, its spectrum must be wide enough to cover the frequency range of interest. The Finite Difference Time Domain (FDTD) marching-in-time scheme is applied to compute the electromagnetic field in the computational domain. Because of the Bloch periodic boundary conditions (27), the electromagnetic field will reach a steady state after all radiative modes are absorbed by the ABC's. For each value of the wave vector **k**, the Maxwell's equations are solved and the field is observed at certain points in the unit cell. These are chosen away from the

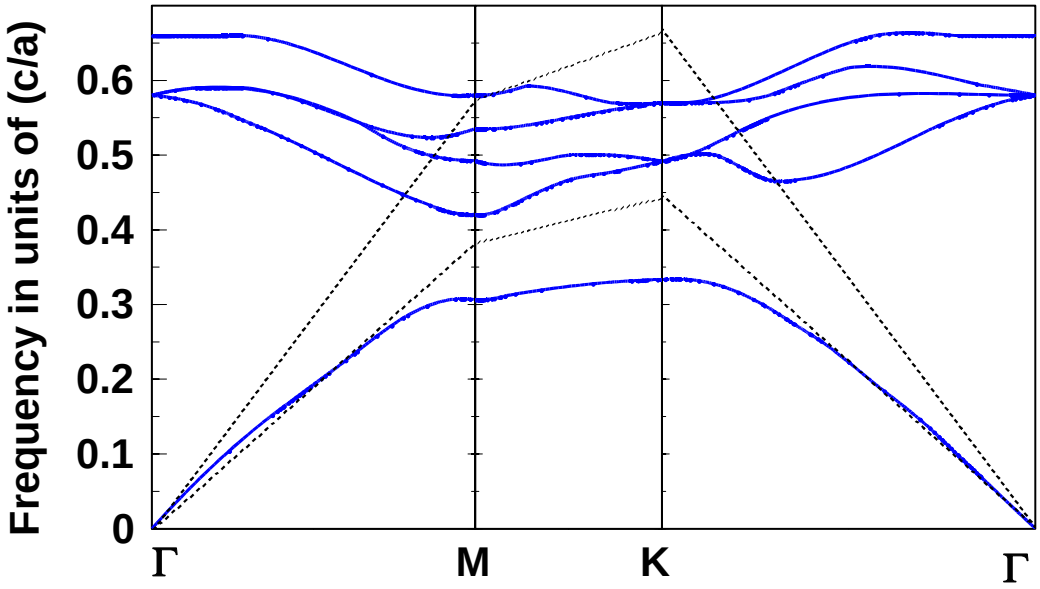

Figure 2. Dispersion diagram of TE-like modes of the infinite photonic crystal shown in Fig. 1*(a)*. To set the horizontal scale, $\Gamma M = \frac{2\pi}{\sqrt{3}a}$. The dashed line represents the upper limit to the modes which are confined to the slab and can not leak into the glass substrate.

symmetry planes of the lattice, (unless some particular symmetry class of the modes is under consideration,) to avoid the possibility of probing the field in the node of a mode. The Fourier Transform of the computed signal has peaks at frequencies of the vertically confined modes that can propagate in the structure with the given wave vector **k**. The computational time must be long enough to allow the desired frequency resolution.

We have computed the dispersion diagram ν versus *k*, of a perforated dielectric slab (ε=12) sitting on a glass substrates (ε=2.25) sketched in Fig. 1(a) using this technique. Wave propagation in a similar freestanding structure was previously calculated using the plane wave expansion method with the super-cell approach[19].

Figure 2 shows the dispersion diagram for the TE-like guided modes of the structure when the propagation vector **k** lies in the x-y plane. The ratio between the thickness t of the slab and the lattice constant a was chosen to be $t/a = 0.333$, while the radius r of the holes was chosen to be $r = 0.40a$. These parameters seem to give the smallest possible mode volume. A wide forbidden gap for the TE-like modes exists in the range of normalized frequencies $0.33c/a \leq \nu \leq 0.43c/a$. As will be shown below, this 2-dimensional photonic band-structure can be used as a reflecting medium to create a cavity with a very small mode volume.

Another important feature of the band structure is that all upper bands are relatively flat. We can say that modes with different values of the wave vector are have limited disperison. As will be discussed in the Chapter 5, this leads to the angle-integrated resonant enhancement of the emission into the leaky modes.

3.2. Numerical Results: Investigation of candidate nano-cavities

Introduction of an irregularity in the periodic structure of a photonic crystal, often referred to as a defect, may cause localization of one or more electromagnetic modes around the defect itself. To completely characterize these localized resonant modes, we have considered a finite sized photonic crystal with a defect close to its center, and we have employed the FDTD using absorbing boundary conditions on all boundaries of the computational domain.

The Fourier Transform of the electromagnetic field at observation points inside the cavity gives the resonant frequencies of the cavity, while the Q of each mode can be

estimated from the decay rate of the energy stored in the cavity. It must be noted that the numerical computation of the cavity Q is very sensitive to several parameters. In particular, to the value of the dielectric material, the kind of absorbing boundary conditions used to terminate the computational domain, and to the distance between the open dielectric cavity and the boundary of the computational domain.

As was mentioned before, to achieve high enhancement of spontaneous emission rate the resonant mode of a cavity must have the smallest possible volume while its Q must be larger than $Q_m=\nu_m/\Delta\nu_m$ of the active material[20], where ν_m and $\Delta\nu_m$ are the frequency and linewidth of the material transition. A Figure-of-Merit for the cavity optimization is the mode's effective volume normalized to the cubic half wavelength of the resonant mode $(\lambda/2n)^3$ in the medium of refractive index *n*:

$$\frac{V_{eff}}{(\lambda/2n)^3}=\frac{\int \varepsilon(\mathbf{r})\mathbf{E}^2(\mathbf{r})d^3\mathbf{r}}{(\lambda/2n)^3\left(\varepsilon(\mathbf{r})\mathbf{E}^2(\mathbf{r})\right)_{\max}} \qquad (28)$$

The FDTD algorithm allows the computation of the effective volume either in the time domain or in the frequency domain by post-processing the computed data. Particular care must be exercised to deal with some numerical issues when computing the effective mode volume. The integration in equation (28) must be performed over a volume enclosing the geometrical defect and large enough to enclose also the mode's electromagnetic energy that spills outside the slab. Also, the search for the maximum value of the electric energy must be carried out in the same volume and preferably along the symmetry planes of the structure. This is to avoid the numerical artifact of high

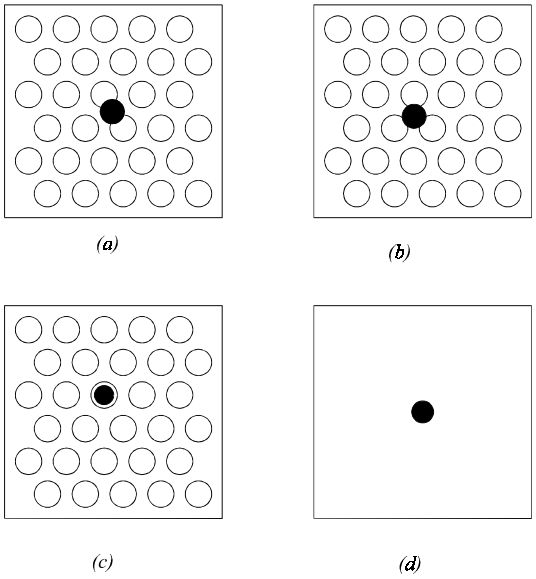

Figure 3. Four different cavity configurations in the finite size photonic crystal were analyzed: (a) A defect is introduced by adding extra material to the bridge between two holes; (b) A defect is introduced in the spot between three holes; (c) The defect consists of added material in the center of a hole; (d) A dielectric cylinder resting on a glass slab (for comparison).

electric field at certain dielectric interfaces due to the discretization of geometry necessary for the Finite Difference computation.

When these considerations are kept in mind, the FDTD technique is a flexible tool to calculate resonant frequencies, field and energy distribution of resonant modes, as well as their Q and effective volume. All this information is necessary for a proper design of efficient cavity-enhanced light-emitting diodes.

3.3. Analyzed structures

A traditional way of creating a donor defect mode is to fill one hole with semiconductor material. However, there are two other high-symmetry points in the Wigner-Seitz cell in addition to the center of a hole that may be a good location for a defect. We studied modes created by adding some extra material in the middle of the bridge between two holes, in the spot between three holes, and in the center of a hole, as shown in Figure 3(a),(b),(c). Those Figures also show the finite lateral size of the photonic crystal in the actual structures investigated. For comparison, we have also studied the properties of the fundamental mode of a single dielectric cylinder (ε=12)

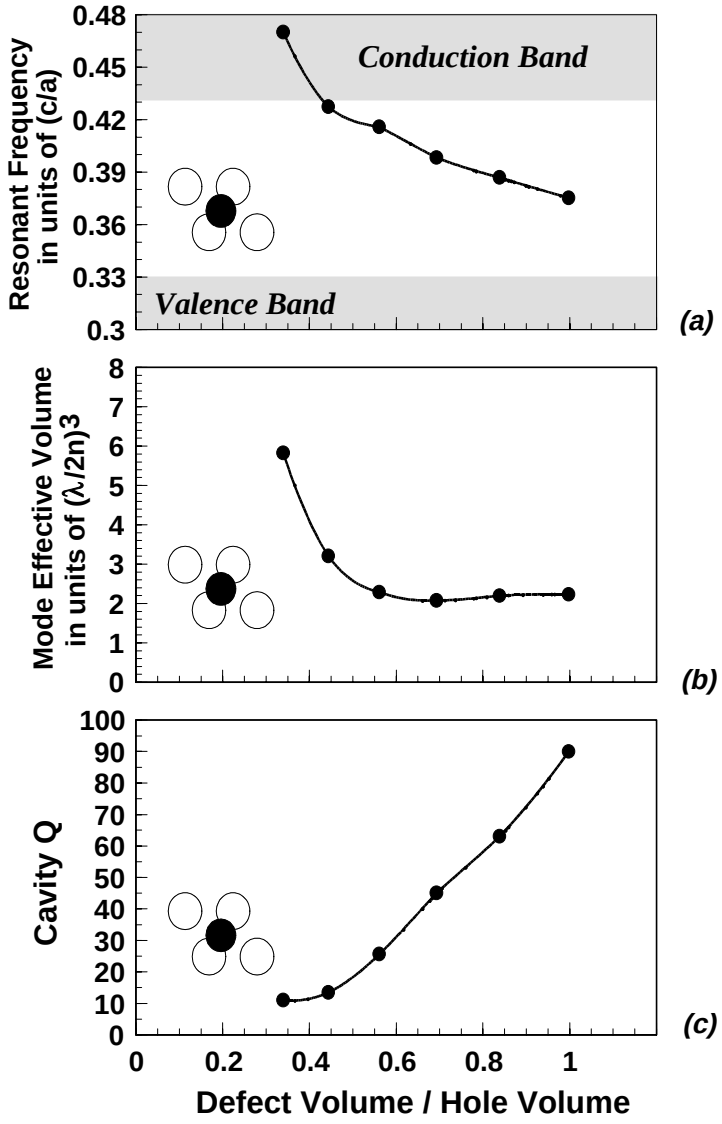

Figure 4. Evolution of the localized mode frequency, effective volume and cavity Q for the defect placed on the bridge between two holes: (a) Resonant frequency of the mode; (b) Effective mode volume in units of $(\lambda/2n)^3$; (c) Cavity Q-factor

located on the same glass substrate (ε=2.25) supporting the 2-D photonic crystal (Figure 3d). These structures can be described by three independent dimensionless parameters: normalized thickness *t/a*, normalized radius of the holes *r/a* and normalized radius of the

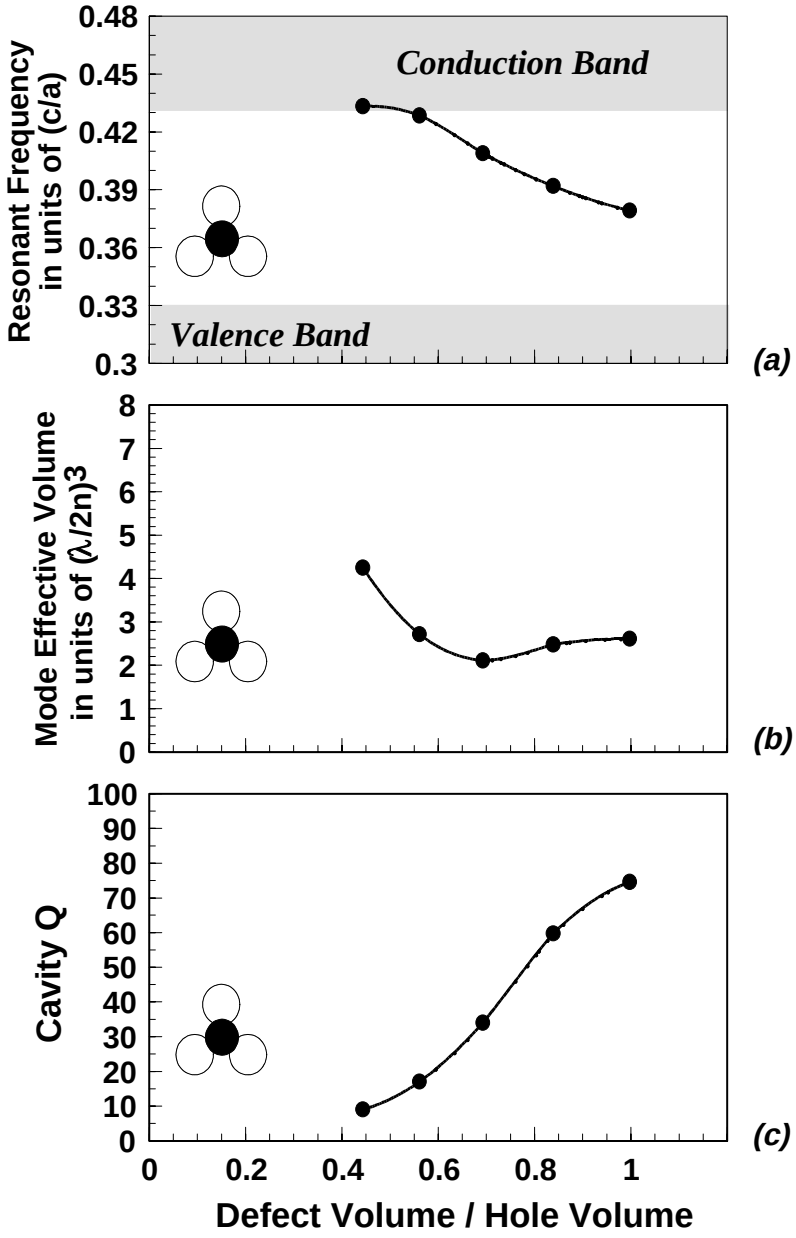

Figure 5. Same as Fig. 4 for the defect placed between three holes.

defect r_d/a. Therefore, optimization of the dimensionless effective volume f has to be performed in the three-dimensional parameter space.

3.4. Cavity Characteristics

Relative thickness, *t/a*, of the structure did not influence the mode volume results much. For all the studied geometries, the best effective volume was achieved at *t/a*~1/3. For technological reasons, the walls between holes should not be too thin. We have chosen *r/a*=0.4, even though larger values of *r/a* may produce slightly better results. Figures 4, 5 and 6 show the variation of frequency, the normalized effective volume, and the Q of the lowest order resonant modes versus the defect size for the different cavity geometries. Typically for all donor modes, the frequency of the mode emerges from the conduction band-edge at 0.43*c/a* and decreases towards the frequency of 0.33*c/a* of the valence band. As can be seen from these Figures, the resonant frequencies of all structures with the same defect size are roughly the same. This suggests an alternative viewpoint: The defect mode is the mode of a single cylindrical resonator "tuned" to the forbidden gap of the photonic crystal, to provide additional mode confinement and higher Q. For small defect size, quality factors are normally on the order of 10. As the mode volume reaches its minimum, Q goes up to 40 or even up 90 as in the case of the bridge defects. It is typical for all modes to have cavity Q increasing as mode volume goes down. Indeed, the more tightly localized the mode, the smaller its tails outside of a finite sized photonic crystal. By comparison, the cavity Q of an isolated cylinder[21] is $0.016\times n^3\approx 7$ and mode volume is $4.52(\lambda/2n)^3$, under our conditions. Probably the most interesting feature is that the minimum of the effective volumes is about $V_{eff}\approx 2(\lambda/2n)^3$ for all three defect types. This make us wonder if there is a fundamental lower limit on the volume size achievable with a certain dielectric material! We believe the mode volume

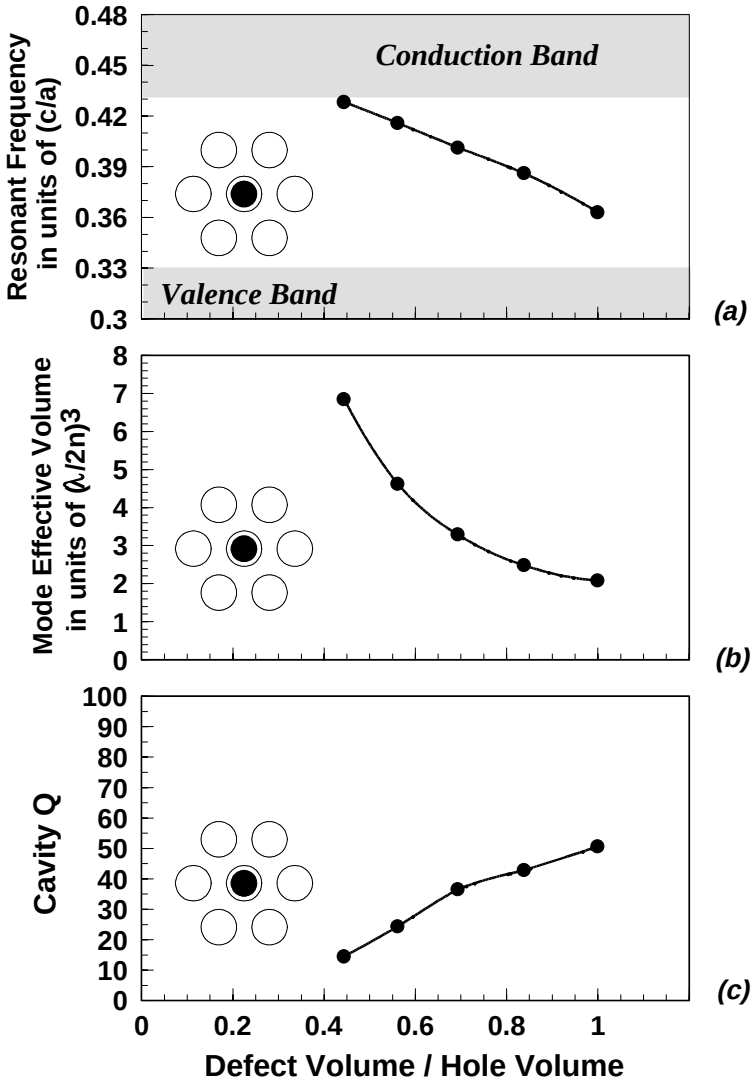

Figure 6. Evolution of the localized mode frequency, effective volume and cavity Q for the defect placed on the center of a hole: (a) Resonant frequency of the mode; (b) Effective mode volume in units of $(\lambda/2n)^3$; (c) Cavity Q-factor.

results for 3-d photonic crystal structures with full 3-d confinement would actually be quite similar, since index guiding provides commensurate vertical confinement. In addition, the case of 1-d periodicity with index guiding in the other two dimensions leads to a volume only 25% higher than $2(\lambda/2n)^3$. Computation of the flux of the Poynting

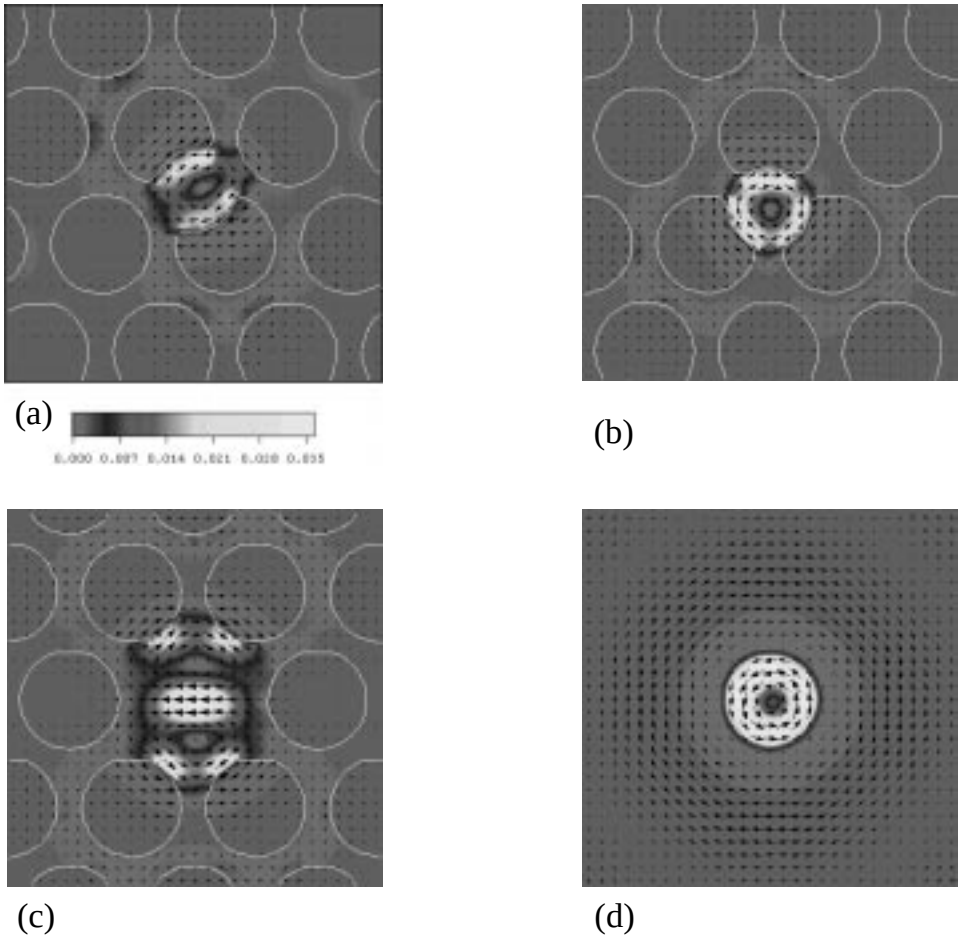

Figure 7. Mode pattern of resonant modes, in the plane of the structure, for the modes with the smallest effective mode volume. Energy density distribution in the xy plane is coded with colors, in-plane electric field is shown as a vector plot. In all cases the concentration of electric energy happens in those regions where some material was added: (a) Added material in the bridge between two holes; (b) Added dielectric material in the spot between three holes; (c) A hole plugged up with dielectric material; (d) A single dielectric cylinder on a glass substrate. The cavity Q~7 and the effective mode volume ~4.5(λ/2n)3 for a cylinder with the same dimensions as defects in Figs. 7(a,b).

vector through a surface enclosing the slab reveals that most of the energy of the defect mode leaks in the vertical direction, rather than being guided by the slab. Therefore increasing the lateral size of the crystal is not likely to increase the cavity Q by much.

The limited required size is a valuable feature in view of possible applications of this type of resonant cavity in light emitting diode, where many such cavities might need to be crowded together.

Figure 7 shows the electric field and energy density distribution of the modes with the smallest effective volumes for all studied configurations, along a *z=const* plane in the middle of the slab. The electric energy density reaches its maximum almost in the center of the dielectric slab. Electric energy density is coded with colors in Fig. 7, and the corresponding projection of the electric field onto the horizontal plane is shown as a vector plot. All these modes are predominantly TE, that is electric field mostly oscillates in the *xy* plane. Due to different locations of the defect, these modes have different symmetries. Structures with a defect introduced into the bridge between two and tree holes, have C_{2v} and C_{3v} symmetry respectively, and their resonant modes are not degenerate. These modes bear close resemblance with the "donut" mode $TE_{01\delta}$ of a cylindrical cavity, shown in Figure 7d.

Considering the case of a defect created by adding material to the center of a hole, the smallest effective mode volume is surprisingly achieved for r_d/a=0.4, that is when the hole is completely plugged. The electric energy distribution of the resonant mode (Figure 7c) has a maximum in the center, which makes the mode a prospective candidate for use in resonant-cavity LED applications, where the active material is placed in the center of the filled hole. Moreover, since this structure has C_{6v} symmetry, the resonant mode is doubly degenerate. According to Equation (25), this fact implies g=2 into the formula of the enhancement factor. For example, in the semiconductor light emitter $In_{0.53}Ga_{0.47}As$,

with Q_m=10 at room temperature, plugging $V_{eff}=2(\lambda/2n)^3$ into Equation (25) gives a five-fold spontaneous emission enhancement Γ/Γ_0=5.

3.5. Summary of numerical results

In this chapter we have described how the band structure of the thin slab photonic crystal was calculated. It was shown that the photonic conduction bands of the photonic crystal are above the light cone and are relatively flat. The defect modes in a dielectric slab photonic crystal have been numerically optimized with respect to the mode volume using the Finite Difference Time Domain algorithm. A record low value of only $2(\lambda/2n)^3$ is shown to be achievable in either of three different configurations. This small mode volume can lead to a significant enhancement of spontaneous emission rates in semiconductor nano-cavities due to the Purcell effect. As will be shown later, a similar effect can be achieved in a perfectly periodic photonic crystal without defects when the emission line of the material is tuned to the leaky conduction bands above the photonic bandgap.

4. Surface Recombination Measurements on Candidate Materials for Nano-cavity Light Emitting Diodes

As the size of opto-electronic devices becomes smaller, surface effects begin to influence their performance. Surface recombination imposes limitations on the efficiency of nanocavity light-emitting diodes, VCSEL's with oxidized apertures, and other devices which require the size of the active region to be comparable to the diffusion length of minority carriers. In this study we concentrated on surface characterization of different material systems, and we identified those suitable for the fabrication of active opto-electronic devices. This chapter is organized as follows: first we describe the experimental setup and the absolute calibration technique, then we introduce the recombination properties we are measuring or modeling. A radiative transport model based on the photon gas[22] approximation is used to extract internal quantum efficiency from the photoluminescence measurements in the context of an $In_xGa_{1-x}N$ sample. The same model with slight modification was used for two other systems - $In_{0.5}(Ga_{1-x}Al_x)_{0.5}P$ and $In_xGa_{1-x}As$. Gallium nitride and chemically passivated InGaAs will be shown to possess a relatively low surface recombination velocity (on the order of 10^4cm/s) while the InGaAlP material system has surface recombination velocity an order of magnitude higher. We show also that surface damage produced by chemically-assisted ion beam etching can be cured by a gentle wet etching and chemical passivation.

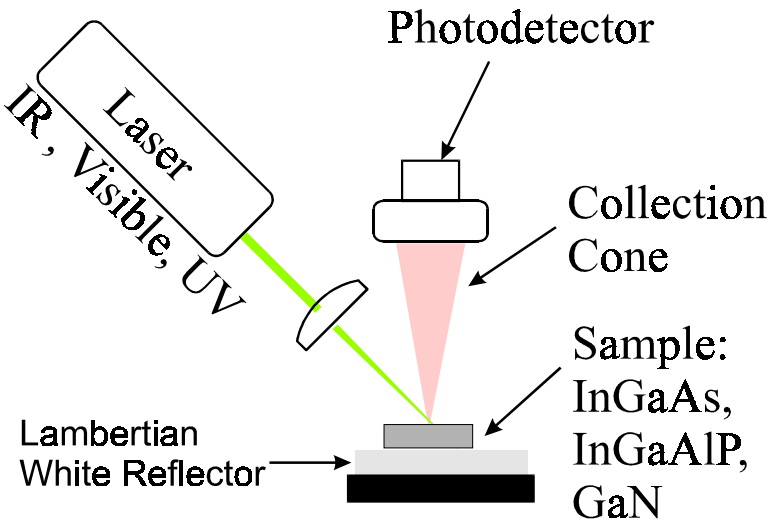

Figure 8. Experimental setup for photoluminescence measurements. The absolute external quantum efficiency is measured by calibrating the measured photoluminescence from the sample against the reading measured from the laser scattered off a perfect white Lambertian reflector. The collection cone is the same for both measurements, so that only a correction for the system wavelength dependence of detector quantum efficiency has to be taken into account.

4.1. Experimental setup

Values of surface recombination velocity were determined by absolute photoluminescence efficiency measuremets, using a setup as shown in Figure 8. Samples are optically pumped with the appropriate laser photon energy above the bandgap. The absolute external quantum efficiency is calibrated by referencing the measured photoluminescence against the scattered light reading from a perfect white Lambertian reflector[25]. In this way, the collection cone of the photodetector is identical in both measurements. Corrections are made for different transmission through the optical setup and the detector quantum efficiency ratio at the photoluminescence and pump

wavelengths. A radiative transport model is used to obtain the internal quantum efficiency of the active material from the measured external quantum efficiency. Furthermore, comparison of the internal quantum efficiency from double heterostructure samples against that from the samples with an exposed active region provides information on the surface recombination velocity of exposed surfaces.

4.2. Radiative transport model

We begin with some definitions:

1) External quantum efficiency η_{ext} is defined as a ratio of the number of PL photons coming out of the sample to the number of photons absorbed in the sample. This is a quantity we can measure.

2) Internal quantum efficiency η_{int} is the probability that an electron-hole pair created in the active region will recombine radiatively. Internal radiative quantum efficiency is a Figure-of-merit for an opto-electronic material.

3) Light extraction efficiency $\eta_{extraction}$ is the fraction of internally generated PL photons that manage to escape from the sample. It depends strongly on the geometry of the sample. It also depends on the internal quantum efficiency if reabsorption in the active region has to be taken into account. For certain simple geometries, light extraction efficiency can be easily calculated.

4) Finally, if optical pumping creates electron-hole pairs outside of the active region, we define collection efficiency η_{coll} as a fraction of carriers that diffuse to the active region.

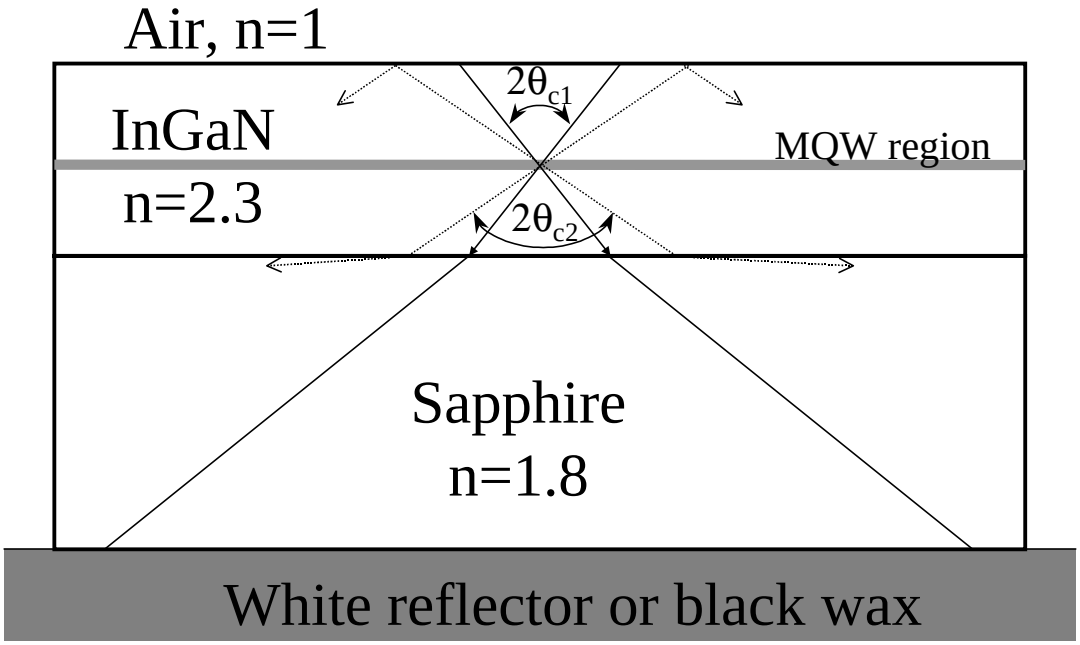

Figure 9a. The semicinductor structure corresponding to the radiative transport model consists of a thin semiconductor film sitting on a sapphire substrate.

If all carriers are collected in the active region η_{coll} =1.

Combining all these definitions, external quantum efficiency can be expressed in terms of three other quantities, which can be measured or calculated:

$$\eta_{external} = \eta_{coll}\eta_{\text{int}}\eta_{extract} \tag{29}$$

Initially we will describe radiative transport model used to calculate internal quantum efficiency in GaN. (For InGaAlP and InGaAs the models employed are almost identical, except they take into account sample's structure such as an absorbing substrate in the case of InGaAlP.) As can be seen from the Figure 9a, the InGaN model considers a film of (refractive index n_{GaN}=2.3) grown on the sapphire substrate with refractive index n_S=1.8 . There are two critical angles and two escape cones associated with them: total

internal reflection at the semiconductor-air interface $\theta_{c1}=\arcsin(1/n_{GaN})$ and at the semiconductor-sapphire interface $\theta_{c2}=\arcsin(n_S/n_{GaN})$. We employ geometrical optics to calculate escape and re-absorption probabilities. Spontaneous emission is assumed to have an isotropic angular distribution. Since the GaN film is relatively thick compared to the wavelength of light in material, a statistical ray optics model[22] is justified and the calculation of emission into individual modes[23] is not necessary.

Suppose N_{inc} photons are incident on the sample. $N_{inc}T_{inc}$ electron-hole pairs are created in the cap layer of the sample, where T_{inc} is Fresnel transmission for the incident wave. $N_1=N_{inc}T_{inc}\eta_{coll}$ of them will reach the active region. If the material's internal efficiency is η_{int}, then $\eta_{int}N_1$ photons are emitted, $E\eta_{int}N_1$ photons escape, and $Z\eta_{int}N_1$ photons are reabsorbed, where E is the escape probability of an emitted photon and Z is the re-absorption probability. Then re-absorbed photons are re-emitted in the amount $Z\eta_{int}^2N_1$. Absorption and re-emission continues leading to a number of escaped photons N_{ESC} given by the sum of a geometric series:

$$N_{esc} = E\eta_{\text{int}} N_1 + E\eta_{\text{int}} (Z\eta_{\text{int}} N_1) + E\eta_{\text{int}} (Z\eta_{\text{int}})(Z\eta_{\text{int}} N_1) + \ldots = \frac{E\eta_{\text{int}} N_1}{1 - Z\eta_{\text{int}}} \qquad (30)$$

It is clear from the Eq. (30) that re-absorption plays a significant role only if internal quantum efficiency is high.

Keeping in mind that external quantum efficiency η_{ext} , the quantity that we measure, is the ratio of the number of escaped photons to the number of photons incident on the sample, i.e. $\eta_{ext}=N_{esc}/N_{inc}$, we can invert Equation (30) and solve it for η_{int}:

$$\eta_{\text{int}} = \frac{(\eta_{ext} / ET_{inc})}{\eta_{coll} + Z(\eta_{ext} / ET_{inc})}, \tag{31}$$

The escape probability, E, is given by the fraction of the escape cone in 4π steradian and Fresnel transmission probablility T(θ):

$$E = \frac{1}{4\pi}\int_0^{2\pi} d\varphi \int_0^{\theta_{c1}} T(\theta)\sin\theta d\theta \cong \frac{\langle T \rangle}{4n_{GaN}^2} \approx 0.07, \tag{32}$$

where <T> stands for the transmission coefficient averaged over the escape cone. Now we will address the re-absorption probability Z.

The diameter of the pump laser beam is about 50 microns, which is much larger than thickness of the InGaN film (2 microns) and both much less thick than the sapphire substrate. We will show that photons reabsorbed outside of the optically pumped region are re-emitted very inefficiently. Therefore, absorption and re-emission is a factor only for photons bouncing inside the thin InGaN film, while photons reflected from the bottom sapphire surface can not be recycled. Then the fraction Z of reabsorbed photons becomes the sum of three terms:

$$Z = \frac{1}{4\pi}\left(\int_0^{2\pi} d\varphi \int_0^{\theta_{c1}} \left(1 - e^{-\alpha d/\cos\theta}\right) R(\theta)\sin\theta d\theta + \int_0^{2\pi} d\varphi \int_{\theta_{c1}}^{\theta_{c2}} \left(1 - e^{-\alpha d/\cos\theta}\right)\sin\theta d\theta + \int_0^{2\pi} d\varphi \int_{\theta_{c2}}^{\pi-\theta_{c2}} \sin\theta d\theta \right), \tag{33}$$

representing 3 cone angle zones $0 \to \theta_{c1}$, $\theta_{c1} \to \theta_{c2}$, and $\theta_{c2} \to (\pi - \theta_{c2})$. The photons beyond $(\pi - \theta_{c2})$ transmit to the bottom of the sapphire substrate and are assumed not to contribute to the re-emission and not to reach the photodetector. In Eq. (33), R(θ) is polarization-averaged reflectivity of the GaN-air interface, α is re-absorption coefficient of the active region material at the photoluminescence wavelength, and d is the overall

thickness of the absorbing quantum wells. The first term in Eq. (33) describes to the re-absorption within the inner escape cone θ_{c1}. The second term corresponds to re-absorption of photons emitted within the second escape cone θ_{c2} but outside of the first. These photons cross the active region once before they go into the substrate. The third term refers to re-absorption of totally internally reflected light in the semiconductor film. This last term dominates re-absorption and is simply $\sqrt{1-n_s^2/n_{GaN}^2} \cong 0.62 \approx Z$, while the two other terms are merely corrections. In this analysis we have assumed that light reflected from the sapphire-air interface is re-absorbed outside of the optically pumped region and does not contribute efficiently to further photoluminescence.

There is a problem with Eq. (31), since the η_{coll} on the right hand side is not exactly known, but is surely less then 1. Therefore Eq. (31) is merely a lower limit to η_{int}:

$$\eta_{\text{int}} \geq \frac{(\eta_{ext} / ET_{inc})}{1 + Z(\eta_{ext} / ET_{inc})}, \tag{34}$$

Likewise, Eq. (31) can be solved for the collection efficiency η_{coll}:

$$\eta_{coll} = \frac{(\eta_{ext} / ET_{inc})(1 - Z\eta_{\text{int}})}{\eta_{\text{int}}}, \tag{35}$$

Once again, η_{int} on the right hand side of Eq. (35) is not exactly known, but it's surely less then 1. Therefore Eq. (35) places a lower limit on carrier collection efficiency:

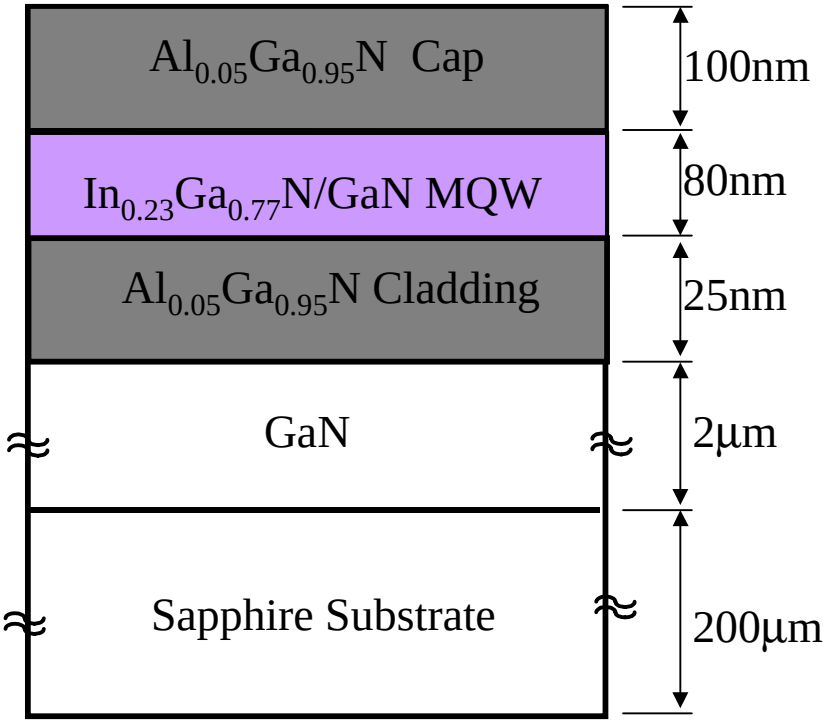

Figure 9b. The schematics of the AlGaN/InGaN MQW structure grown by MOCVD on a C-plane sapphire substrate.

$$\eta_{coll} \geq (\eta_{ext} / ET_{inc})(1 - Z) \qquad (36)$$

Thus a measurement of η_{ext} can place a lower limit on η_{int} through Eq. (34) and a lower limit on η_{coll} through Eq. (36). This procedure will be useful if the experimental results for η_{ext} point to limits on η_{int} and η_{coll} that are reasonably close to 1. For InGaN for example, the limits are $0.87<\eta_{int}<1$ and $0.87<\eta_{coll}<1$, constraining the experimental values very tightly.

4.3. Gallium Nitride

The InGaN MQW structure schematically shown in the Figure 9b was grown using MOCVD on a C-plane sapphire substrate.[24] It was optically pumped using the 325nm line of a continuous wave HeCd laser.[25] The lower limit on internal quantum efficiency, η_{int}, measured and analyzed by Eq. (34) ranges from 40 to 87% for different samples. Variation in the sample quality was correlated with the number of quantum wells in the InGaN MQW region and was not attributed to the properties of the GaN cap layer. Such high internal quantum efficiencies allowed us to calculate the upper limit on the surface recombination at GaN surface using the following considerations:

The optical absorption length for the 325nm wavelength in the GaN cap layer is only 80nm[26]. It is comparable to the cap layer thickness. Therefore all pump light is absorbed everywhere throughout the cap layer of the GaN, and all electron-hole pairs generated near this surface need to diffuse into the quantum well region, as shown in Figure 9b to contribute to photoluminescence. Since the observed collection efficiency η_{coll} is reasonably good, the diffusion length L_d in GaN must be greater than the cap thickness L_{cap}=100nm.That means that the carrier distribution in the sample in vertical direction can be approximated as $n = n_0(1 - z/L_{cap})$, providing that all carriers recombine quickly enough in the quantum well. The upper limit on collection efficiency is:

$$\eta_{COLLECT} \le \frac{D/L_{CAP}}{D/L_{CAP} + s} + \frac{s}{D/L_{CAP} + s}\left(\frac{1}{\alpha L_{CAP}} - \frac{1}{e^{\alpha L_{CAP}} - 1}\right), \qquad (37)$$

where s is the surface recombination velocity and D is the ambipolar diffusion constant, the diffusion constant of the slower species, which are holes. If the absorption length was

smaller than the cap thickness, that is $\alpha L_{cap} \gg 1$ this equation would reduce to a simpler expression corresponding to having all carriers generated at the surface:

$$\eta_{COLLECT} \leq \frac{D / L_{CAP}}{D / L_{CAP} + s}$$

Combining Eqs. (33) and (37) yields an upper limit on the surface recombination velocity in GaN to be $S<0.28D/L\sim28000$ cm/s with diffusion constant assumed[27] to be 1 cm^2/s in undoped InGaN.

The optical model described above neglects reflections from the bottom surface of the sapphire substrate since most of those photons are reflected and absorbed outside of the optically pumped region, and can not be re-emitted. To verify this assumption we compared photoluminescence from a sample with the bottom surface and edges coated with the absorbing black wax to that of the same sample sitting on the white reflecting surface. As expected, results of these measurements did not differ.

The pump level for these experiments was 10mW onto a 25μm diameter spot, or ~1000A/cm^2. At lower pumping intensities the internal photoluminescence goes down, explaining why absorption and emission outside of the pumped region is so inefficient and can be neglected.

Fabrication of the miniature devices often involves dry etching. To see the effect of the dry etching on the surface recombination velocity we exposed the top surface of the one of the best samples to chemically assisted ion beam etching ($Ar^+ + Cl_2$). After etching about 10 nanometers of the cap layer away, the measured quantum efficiency dropped by a factor of 5, which corresponds to the surface recombination velocity $s=10^5$cm/s on the

damaged surface. However, subsequent short wet etch cleaning in the hot KOH which removed another 5-10nm of the AlGaN cap brought the sample's efficiency back to about 80% of the initial efficiency. That indicates that ion damage in nitride materials introduced by the dry etching can be effectively removed.

4.4. InGaAlP

In this case we studied samples consisting of 0.75μm thick $In_{0.5}(Ga_{1-x}Al_x)_{0.5}P$ (λ=615nm, λ=630nm) active region doped at $n=10^{17}cm^{-3}$ level sandwiched between n-type InAlP cladding layers grown on an absorbing GaAs substrate (Figure 10a). The sample was optically pumped with the CW 568nm argon-krypton laser which is not absorbed by the InAlP cladding layer. The iso-type double hetero-structure allowed us to be un-concerned about effects related to a p-n junction. Internal quantum efficiency of the as-grown double hetero-structure sample was measured to be 80%. After the top cladding was removed with the H_3PO_4:H_2O_2:H_2O(5:1:1), as shown in Fig. 10b, the surface of the active region was exposed to air. The PL signal, and hence internal quantum efficiency, dropped by a factor of 30. Since thickness of the active region is less than the typical diffusion length in this material system, and there is a potential barrier at the bottom of the active layer, the carrier density distribution is constant, even though electron-hole generation occurs mostly at the top interface (see Appendix). For that reason internal quantum efficiency or an as-grown structure and a structure with an exposed active region is simply determined by competition between the rates of radiative and non-radiative recombination. The efficiency of intact double hetero-structure is:

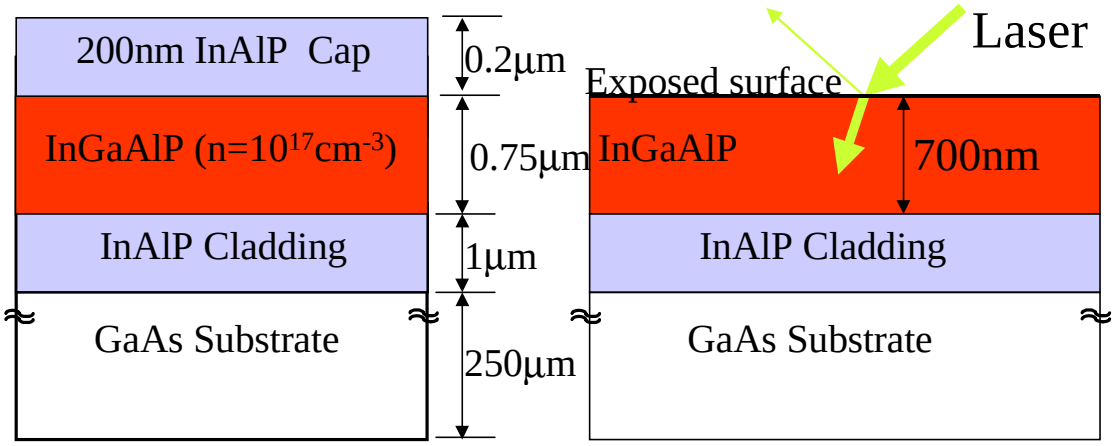

Figure 10. a) The InGaAlP sample consists of 0.7μm thick $In_{0.5}(Ga_{0.92}Al_{0.08})_{0.5}P$ (λ=630nm) active region doped at $n=10^{17}cm^{-3}$ level sandwiched between n-type InAlP cladding layers grown on absorbing GaAs substrate.b) When the top InAlP cladding layer is etched away, the nonradiative surface recombination on the exposed surface of the active region becomes the dominant recombination process.

$$\eta_{AS-GROWN} = \frac{1/\tau_R}{1/\tau_{NR} + 1/\tau_R} \qquad (38)$$

The efficiency when the InAlP cap of the double hetero-structure is etched away is:

$$\eta_{ETCHED} = \frac{1/\tau_R}{1/\tau_{NR} + 1/\tau_R + s/L}, \qquad (39)$$

where τ_R and τ_{NR} are radiative and non-radiative minority carrier lifetimes and L is the thickness of the active region. We can estimate the surface recombination velocity from the doping level of the active region $N_D=10^{17}cm^{-3}$ and a typical value of the radiative recombination constant[28] $B\sim4\cdot10^{-10}$ cm^3/s using the Equation (38). The recombination rates would be $1/\tau_R=BN_D=4\cdot10^7 s^{-1}$, $1/\tau_{NR}=10^7$ s^{-1}. Surface recombination velocity is easily obtained from (39) and equals to $s=10^5 cm/s$. This is about twice the surface

recombination velocity previously reported for InGaP[29]. Surface treatment with ammonium sulfide used in Ref. 29 did not show any increase in PL signal. The poor surface properties could be attributed to the presence of aluminum and its oxidation. Measured surface recombination velocity, although significantly higher than in GaN, is still an order of magnitude lower than that of a GaAs surface. Still there is a chance that some chemical treatment or re-growth technique might be established for the InGaAlP material system. Increasing the doping level may increase radiative recombination, thus making spontaneous emission more competitive with non-radiative recombination, as necessary for fabrication of microcavity LED's. In our PL measurements on the exposed active region, the surface degraded over a 30s period for an 8mW laser beam focussed in a 50μm diameter spot. Every time the laser beam was moved to a new location on the sample, PL refreshed, and then decayed again. At lower pump power, the surface degraded more slowly. This observation suggests a possibility of sealing or passivation of the surface before it gets oxidized.

4.5. InGaAs

Surface recombination velocity was studied on a 20nm n-type $In_{0.53}Ga_{0.47}As$ single quantum well (QW) structure with InP cladding layers grown on an InP substrate and separated from the substrate by an undoped 1μm InGaAs stop-etch layer as shown in Figure 11a. The quantum well donor impurity concentration was $n \sim 10^{18} cm^{-3}$. This structure was designed for the fabrication of a thin-film cavity-enhanced light-emitting diode, a process that involves making an array of holes in the QW structure and bonding

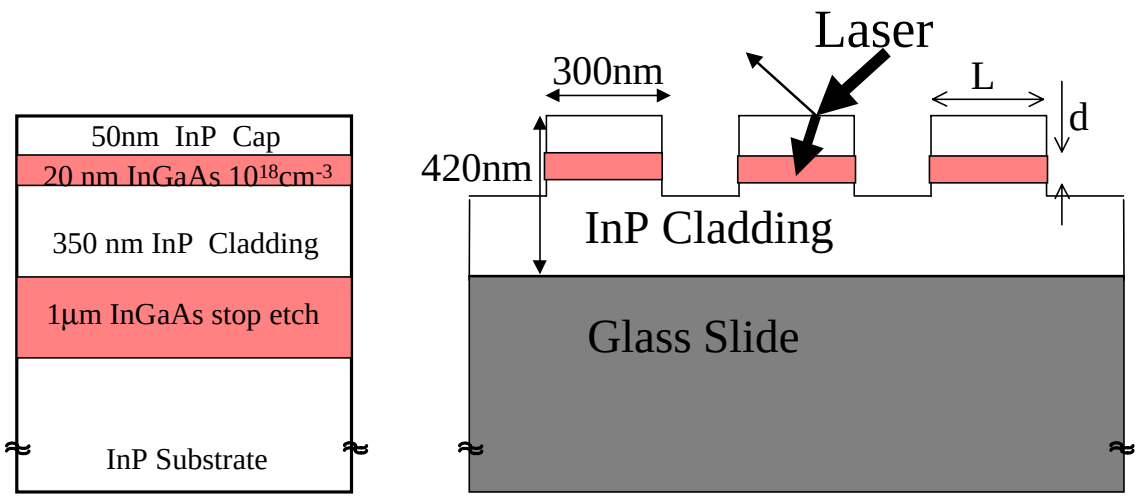

Figure 11. a) An n-type $In_{0.53}Ga_{0.47}As$ single quantum well structure with InP cladding layers was grown on a InP substrate and separated from the substrate by an undoped InGaAs stop-etch layer. b) A set of mesas of widths ranging from 0.12 to 2μm was etched so that the edges of the active region were exposed. The structure was bonded to a glass slide after the substrate removal process.

it on the glass slide[30]. We were interested in measurements of surface recombination velocity on the vertical walls produced by chemically assisted ion beam etching (CAIBE) and in finding chemical treatments in order to minimize it. A set of mesas with widths ranging from 0.12 to 2μm was etched as shown in Figure 11b so that edges of the active region were exposed. The overall double heterostructure was bonded to a glass slide after a total substrate removal process, as shown in Figure 4b. Internal quantum efficiency of the as-grown double hetero-structure sample was nearly 100%. Ratio of the photoluminescence from the mesa etched sample to the PL signal of intact double hetero-structure depends on the surface recombination velocity and the width of the mesa. As in

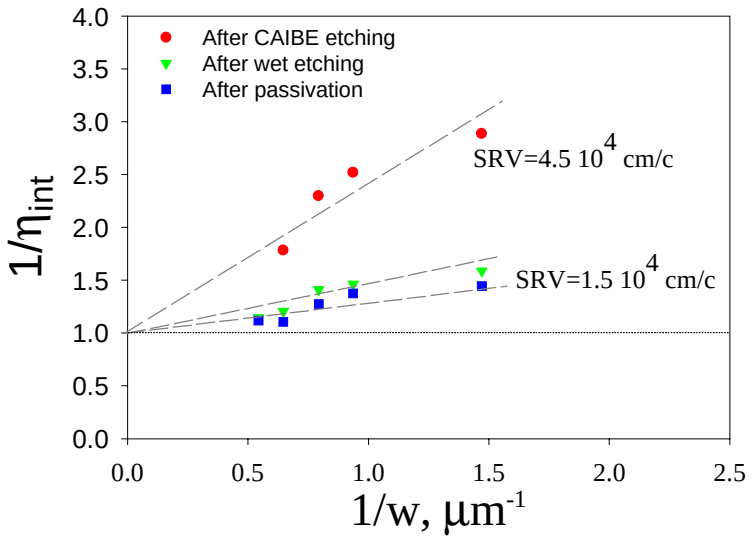

Figure 12. Inverse quantum efficiency plotted versus inverse mesa width. The slope of the fitted line is equal to $2s\tau_R$.

the InGaAlP case, the width of all mesas was smaller than a diffusion length, and the carrier density was uniform across the mesa. In this case the expression for quantum efficiency of the etched samples is very similar to that used for InGaAlP:

$$\eta = \frac{1/\tau_R}{1/\tau_R + 2s/w}, \tag{40}$$

where w is the mesa width. The factor of two in the denominator comes from two exposed surfaces instead of one for the InGaAlP case. Also, we neglected non-radiative recombination in the bulk since the PL measurements of the unetched material showed internal quantum efficiency of the sample to be close to 100%. Equation (40) can be transformed into

$$\frac{1}{\eta_{\text{int}}} = 1 + 2s\tau_R \frac{1}{w}, \tag{41}$$

so that slope of the $1/\eta$ vs. $1/w$ gives value of $2s\tau_R$ as shown in Figure 12. Fitting data into the equation is straightforward since the intercept in the Eq. (41) is fixed and equals to one. The value of the radiative constant "B" was assumed the same as in the InGaAlP case. We observed surface recombination velocity equal to $4.5 \cdot 10^4$cm/s after the mesas were etched using CAIBE technique (shown in circles in Fig. 12). After the surface damage was removed using the gentle wet etch in H_2SO_4:H_2O_2:H_2O=1:8:5000 solution (triangles in Fig. 12) SRV decreased to $1.7 \cdot 10^4$cm/s. Further improvement was observed after the 5 minute long passivation in a solution of ammonium sulfide $(NH_4)_2S$ (squares, SRV=$1.5 \cdot 10^4$cm/s). It turned out that surface damage depends on the ion energy of the etching process. The reported results correspond to 500V Ar^+ accelerating potential in CAIBE process. The ion damage seems to be significantly deeper when 1500V voltage is employed, resulting in larger surface recombination velocities and requiring more intensive cleaning.

4.6. Summary of material properties

In this chapter we studied surface recombination velocities in InGaN, InGaAlP and InGaAs material systems using absolute calibration photoluminescence measurements. Surface recombination velocity is shown to be less than 28000 cm/s in GaN, 15000cm/s in passivated InGaAs and 10^5cm/s in InGaAlP. We also showed that residual surface damage caused by dry etching could be removed by proper surface

treatment. These results suggested InGaAs to be the most favorable material system for nanofabrication of active devices based on photonic crystals.

5. Photoluminescence measurements on photonic crystals

5.1. Fabrication of thin film photonic crystals

Two MOCVD-grown $In_{0.47}Ga_{0.53}As$/InP single quantum well double hetero-structures of same composition but different thickness were used for these experiments. The samples' dimensions are shown in the table below.

	Structure 1	***Structure 2***
InP top cladding layer	***200nm***	***90nm***
$In_{0.47}Ga_{0.53}As$, $n=10^{18}cm^{-3}$, active region	***20nm***	***60nm***
InP bottom cladding layer	***200nm***	***90nm***
InGaAs stop etch layer	1000nm	1000nm
InP substrate	300μm	300μm

A standard substrate removal technique was used to fabricate thin films for the photoluminescence experiments:

The wafer was cleaved in square pieces about 5mm×5mm, and glued to the glass slide upside down using the UV-curable optical adhesive (Norland 73). The samples were etched with 70% hydrochloric acid for approximately 2 hours to remove the InP

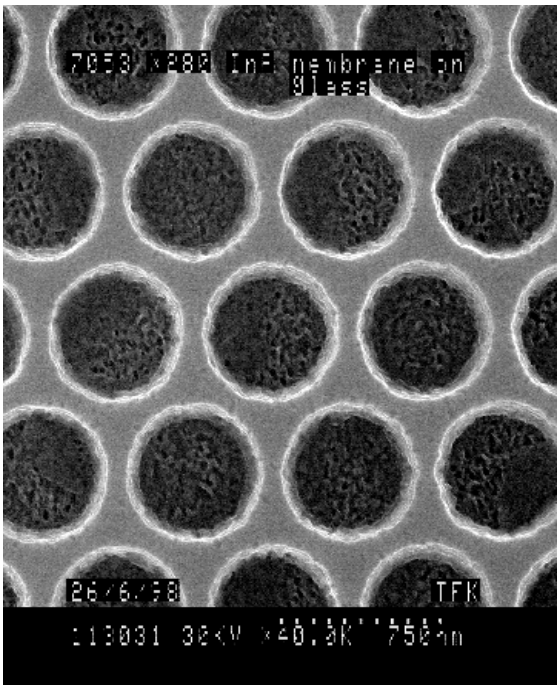

Figure 13. A triangular array of holes in the thin film on InGaAs/InP double hetero-structure. The spongy gray substance inside the holes is the optical glue. Lattice spacing is 720nm, film thickness is 420nm and hole diameter is 550nm.

substrate. HCl is a selective etchant for InP with respect to InGaAs. However a special care should be exercised in order to protect edges of the sample and prevent the etchant from attacking the InP cladding layer. For this reason it is better to remove the sample from the solution as soon as the active reaction ceases.

After the InP substrate is removed, the H_2SO_4:H_2O_2:H_2O (1:8:500) is used to remove the 1μm thick InGaAs stop etch layer. This solution is selective with respect to InP and does not attack the cladding layer. Its etching rate of InGaAs is approximately 15A per second, and it takes about 10 minlutes to remove it.

After the substrate removal is complete the sample's PL is tested using the setup described in the chapter on surface recombination velocity. Normally the quantum

efficiency of the material does not change during the substrate removal procedure and we end up with a less than half a micron thick, semitransparent film, reliably bonded to the glass slide. It would be useful to bond the sample to sapphire instead of glass for heat-sinking considerations, but that would be limited by the thermal conductivity ot the adhesive in any case.

A set of photonic crystal structures was etched into the thin film samples using electron-beam lithography and ion beam etching. Normally, each sample had numerous structures spanning a lattice constant range sufficient for the spontaneous emission band to overlap with both the photonic bandgap and with conduction band modes. In our case of emission wavelength centered at λ=1650nm, the photonic crystal's lattice constant was made to vary from a=550nm to a=900nm. Correspondingly, the center of the photon band gap varied from λ=1300nm to λ=1900nm. An SEM picture of a typical structure with a=720nm, t=420nm and r/a=0.4 is shown in Figure 13.

The etching is performed as follows: A layer of SiO_2 is deposited on the sample surface using plasma chemical vapor deposition. This will be the mask. Next a PMMA resist (350K molecular weight) for e-beam lithography is spun to a 200nm thickness, and a desired pattern is written using a Leika EBPG5 e-beam writer running at approximately 5MHz. The pattern is transferred from photoresist to SiO_2 mask using directional chemically assisted ion beam etching (CAIBE) with CHF_3 for 6 minute. Finally, the pattern is transferred into the semiconductor in the same CAIBE machine using CCl_4 at 200^oC with 200nm/min etch rate. The residual ion damage is cleaned, as discussed in the chapter 4 by a gentle wet etching in H_2SO_4:H_2O_2:H_2O (1:8:500) and subsequent surface

passivation in a stinking $(NH_4)_2S$ solution. The effect of passivation on the surface recombination velocity of InGaAs was discussed in the Chapter 4.

5.2. Experimental Setup for angle-resolved photoluminescence:

The setup used in our measurements is shown in Figures 14 and 15. A sample is pumped with a 780nm AlGaAs laser. A laser beam is focussed onto a photonic crystal by a microscope objective. Since InP is absorptive at the 780nm laser wavelength, about 60% of the light is absorbed in InP cap layers. All our photonic crystals were at least 70μm×70μm in area and 10X magnification objective focussed the beam on the sample. The same objective was used for imaging the sample by means of a beam-splitter (BS). The photoluminescence signal was collected on the oppposite side of the sample. A

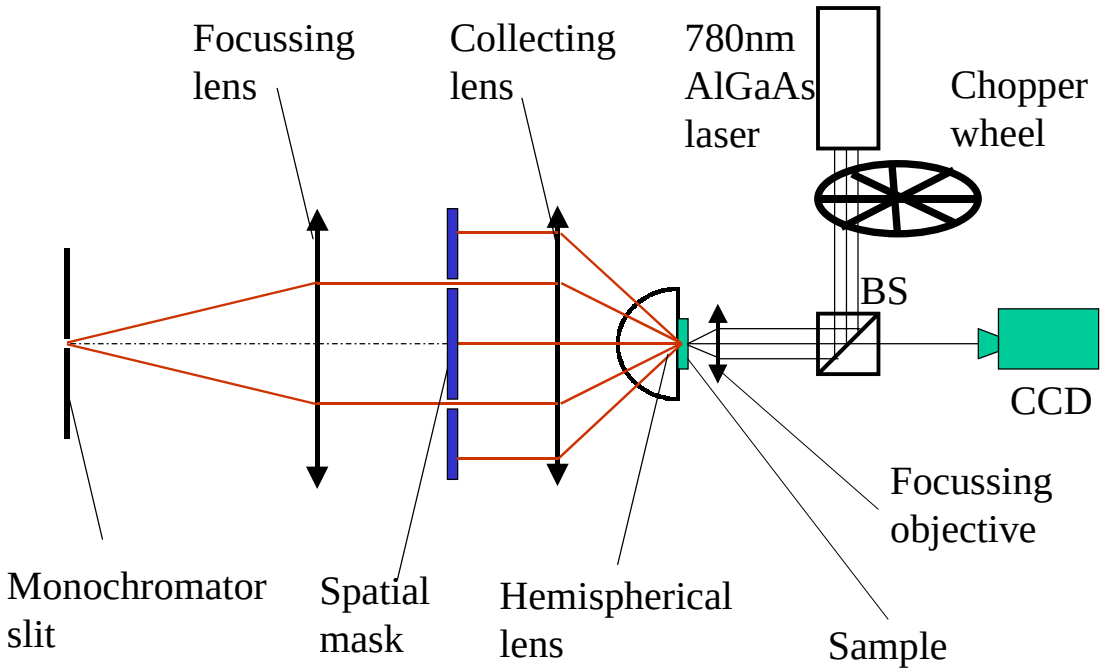

Figure 14. Experimental setup for angle resolved photoluminescence measurements. The sample is pumped with the 780 AlGaAs laser and spontaneous emission is collected on the opposite side. A spatial mask is used to select the emission at the desired angle.

sample was attached to a hemispherical lens to allow extraction of the photoluminescence signal from the glass at beyond the normal total internal reflection angle. Indeed, since all rays originating in the center of the hemisphere hit its surface at normal incidence, the rays are not refracted and transmission is maximized. A lens configuration shown in the Figure 14 was used to measure PL at angles closer than 45^o to normal. The PL signal was collected by a collimating lens, and, for angle-resolved measurements, was passed through the spatial mask shown in the Fig. 14. Only beams going in one particular direction are allowed to go through. As can be seen from the Figure, this direction is uniquely defined by the distance *r* between the slit and the optical axis of the system. In this way we can sample different angles and different directions of the escaping light. The selected fraction of photoluminescence is focused on the entrance slit of a SPEX Minimate 1681B monochromator controlled by SpectraMax spectrometer software. A nitrogen cooled germanium detector was used to measure the output signal in a standard lock-in amplifier configuration. This detector provided excellent sensitivity, and we had to attenuate the signal even after the it was resolved in wavelength and in angle. A modification of this setup shown in Figure 15 was used to make measurements of the PL at angles farther than 45^o from normal. An ellipsoidal reflector with 140mm and 70mm half-axes is used to collect the light and a focussing lens matches it to the f=3.9 monochromator. A full set of masks was used to select different angles and different directions of the Brillouin zone.

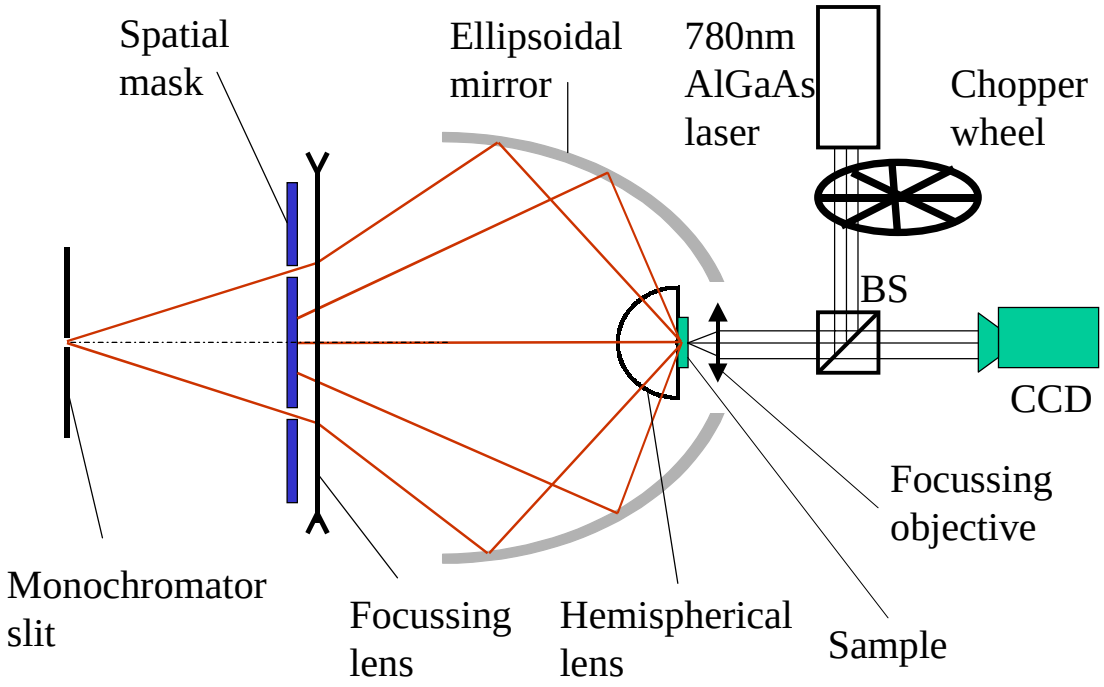

Figure 15. Experimental setup for angle resolved photoluminescence measurements. The sample is pumped with the 780 AlGaAs laser and emission is collected by an elliptical reflector. A spatial mask is used to select the emission at the desired angle.

The described experimentsl setup allows for measurements of the dispersion diagram of a photonic crystal's leaky modes, that is modes with frequencies lying above the light cone in glass indicated as a broken line in the band structure in Figure 2 in Chapter 3. Indeed, as discussed above, any eigenmode of a thin slab photonic crystal with the in-plane wave vector $\mathbf{k}_{\|}$ must satisfy Bloch condition for in-plane propagation

$$\mathbf{E}(\mathbf{r},t) = \mathbf{U}(\mathbf{r},t)e^{-i\mathbf{k}_{\|}\cdot\mathbf{R}}, \qquad (42)$$

where **U(r)** has the periodicity of a crystal. On the other hand, the wave function of the mode outside of the slab, in the air or in the glass must be asymptotically a plane wave.

$$\mathbf{E}(\mathbf{r},t) \sim e^{-i(\mathbf{k}_{\|}\cdot\mathbf{R}+\mathbf{k}_{\perp}\cdot\mathbf{r})}, \tag{43}$$

where $\mathbf{k}_{\|}$ is the out-of-plane component of the wavevector, so that the propagation angle is $\alpha = \arctan(\mathbf{k}_{\|}/\mathbf{k}_{\perp})$. Then, keeping in mind that for the modes above the line light $\omega(\mathbf{k}_{\|}) > \mathbf{k}_{\|}/cn$, we conclude that relation

$$\left(\frac{\omega(\mathbf{k}_{\|})n}{c}\right)^2 > \mathbf{k}_{\|}^2 + \mathbf{k}_{\perp}^2 \tag{44}$$

can not be satisfied for real ω and **k**. Thus the modes in the region above the light line have to be leaking and hence detectable. From the information on frequency versus emission angle we are able to reconstruct the band structure of the leaking modes.

In our setup the emission angle, α, into the glass is found and as α=atan(*r*/*f*), where *r* is the radius of the slits of the mask and *f* is the focal length of the collecting lens. Then, from the wavelength λ of the PL peak we can obtain the dimensionless frequency (i.e. frequency in units of *c*/*a*, *a* being the lattice constant and *c* being the speed of light) simply as *a*/λ and the value of $\mathbf{k}_{\|}$ in units of π/a as

$$\frac{2\pi}{\lambda}\cdot\sin\alpha\cdot\frac{a}{\pi} = \frac{2a}{\lambda}\sqrt{\frac{1}{1+f^2/r^2}}. \tag{45}$$

A similar geometrical consideration allows the extraction of data from measurements with the elliptic mirror with the use of the ellipse property

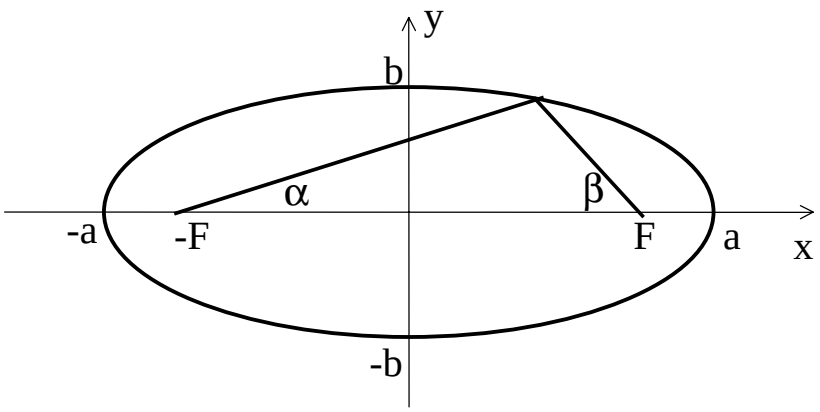

Figure 16. The angle of the incoming beam allows us to calculate the emission angle from geometrical properties of the ellipse

$$tg\,\alpha/2 \cdot tg\,\beta/2 = \frac{1-e}{1+e}, \tag{46}$$

where α and β are polar angles at focal points and $e = F/a = 0.85$ is the excentricity parameter of the ellipse, with $F = \sqrt{a^2 - b^2}$ being its focal length as shown in Figure 16. Equation (46) allows us to find the emission angle β from the collection angle α.

In the following sections, this method of calculation was applied to all data obtained using the angle-resolved PL measurement setup from Figures 14 and 15.

5.3. Overall photoluminescence measurements

All fields of a thin slab photonic crystal were measured using the PL setup described in chapter 4. This gave a quick way of estimating overall photoluminescence efficiency. Two sets of photonic crystals were studied: a triangular array of holes *r/a=0.4* and triangular array of holes with a small round defect in each every hole with a radius of a plug $r_d/a=0.25$. The latter was chosen for study as a of a di-atomic photonic crystal with a correspondingly complicated mode structure. Samples with lattice constant spanning the range from a=550nm to a=900nm were fabricated. The results of measurements for these lattices are shown in Fig 17. As one can see from the Figure 17, the photoluminescence efficiency increases with lattice constant. The pumping conditions were fixed and the results did not depend on orientation of the pumping beam with respect to samples. The dependence in Figure 17 represents exactly the behavior one

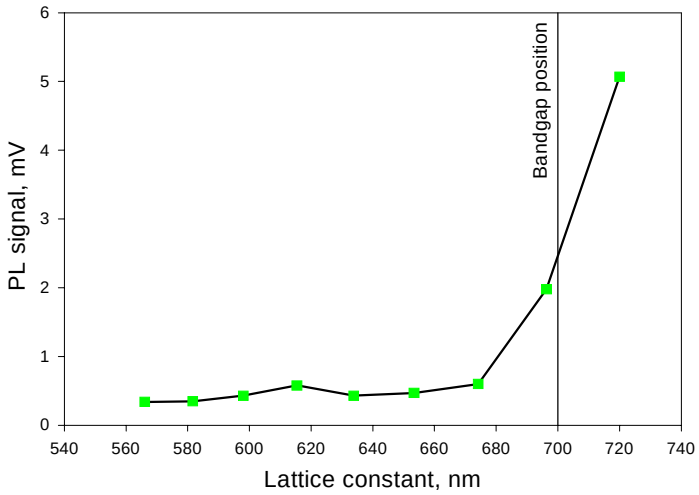

Figure 17. Photoluminescence from a thin slab photonic crystal with a triangular lattice. Thickness of a crystal is t=0.42nm.

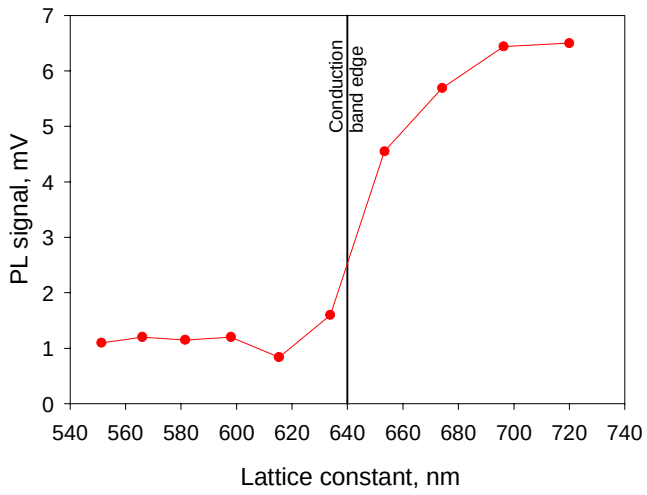

Figure 18. Photoluminescence from a thin slab photonic crystal with a triangular lattice with a small round defect in each every hole with a radius of a plug $r_d/a=0.25$. Thickness of a crystal is t=0.42nm.

would expect for emission into the leaking conduction band modes. Indeed, at small lattice constant, the semiconductor emission falls into the forbidden TE gap of the photonic crystal. The light is emitted into the TM guided modes and it can not be efficiently detected. When the spontaneous emission band overlaps with the forbidden TE gap for guided modes, emission rate is so small. However, as lattice constant of a photonic crystal becomes larger, the frequency of the photonic bandgap slides down and emission band starts to overlap with the leaking conduction band modes. Most of the photons are emitted into these guided modes of the crystal and then leak into the free space.

The photonic bandgap is at lower frequencies for the type of the crystal with plugs shown in Figure 18, since it has larger effective refractive index. For that reason, as can

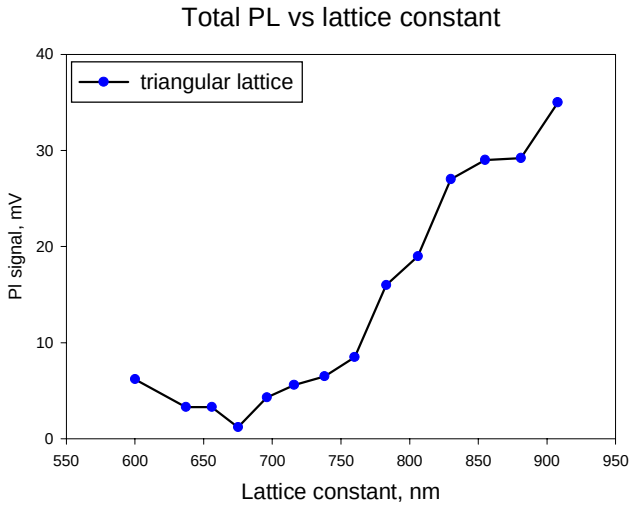

Figure 19. Photoluminescence from a thin slab photonic crystal with a triangular lattice. Thickness of the photonic crystal is t=240nm.

be seen from the Figure 18, the onset of a strong spontaneous emission happens at a smaller value of lattice constant a~640nm. The behavior of such photonic crystals was predicted by S.Fan *et al.* [19] for larger lattice constants but influence of non-radiative recombination, a factor crucial for the analyses at small lattice constants, was not taken into account in their work.

Since, as will be discussed later, the number of modes in our 420nm thick samples turned out to be too large to resolve, a thinner sample based on the same InGaAs/InP material system was fabricated. As can be seen from the Figure 19, the same trend is observed for a 240nm thick sample. The lattice constant spanned the range from 650 to 920nm. Since a thinner sample has lower effective refractive index, the increase of the photoluminescence intensity occurs at a larger lattice constant a~780nm. The dip at

a=670nm is most probably a fabrication defect. It's worth noting however that the slight increase in the PL efficiency at smallest lattice constants is repeatable. We attribute it to external scattering of the guided modes at the interface between the photonic crystal and the surrounding unetched area of the experimental film.

5.4. Spectral properties of PL from Photonic Crystals

Spectra of both types of photonic crystals were measured using the experimental setup shown in Figure 14. A lens with a numerical aperture N.A.=0.2 was used to collect light escaping close to normal and no masks were used. A set of typical angle-integrated photoluminescence spectra is shown in Figure 20. One can see the specific "peaky" features in the spectrum shown blue-shifting as lattice constant decreases. The same behavior is present in the Figure 21 for the second type of a lattice with plugged holes. It is typical for this second type of lattice to have more peaks in the spectrum. This is consistent with the denset band structure of this sample.

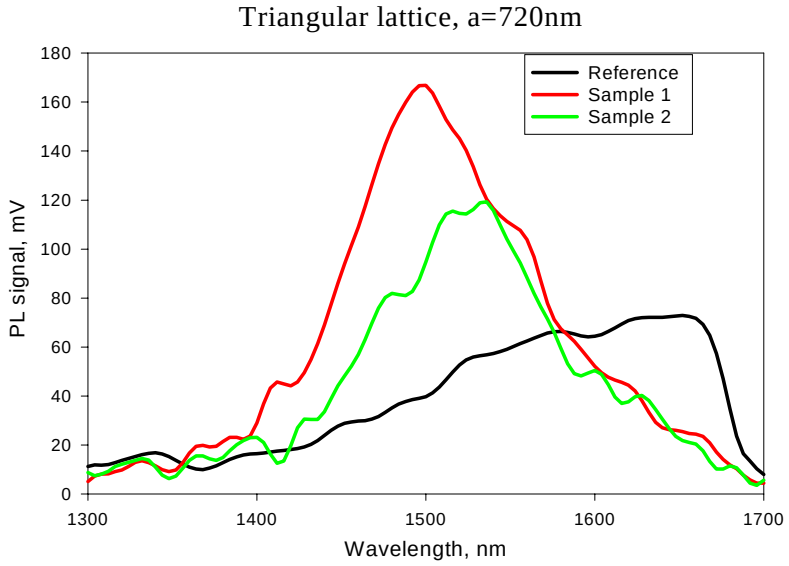

Figure 20: Angle-averaged photoluminescence of the bare lattice is considerably different from that of the reference sample. PL peaks are shifted according to the lattice constant.

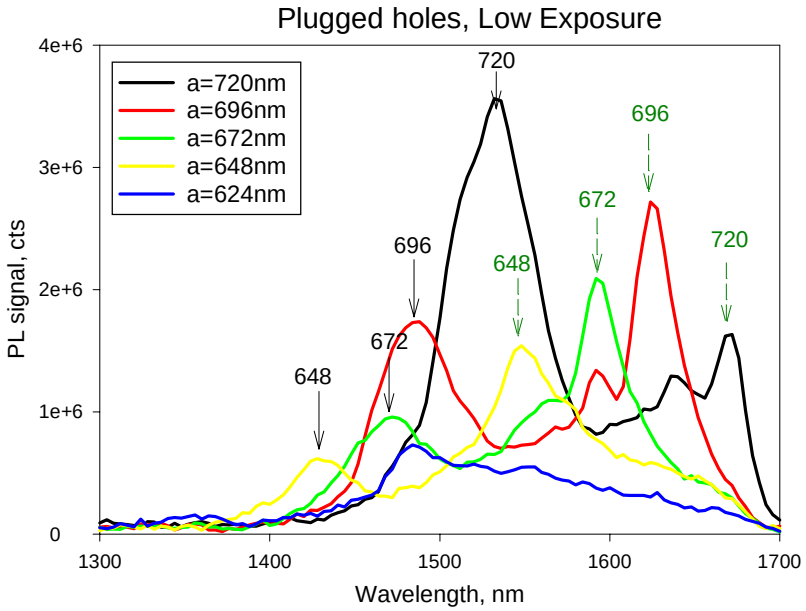

Figure 21: Evolution of the spectra of the lattice with a defect in every hole.

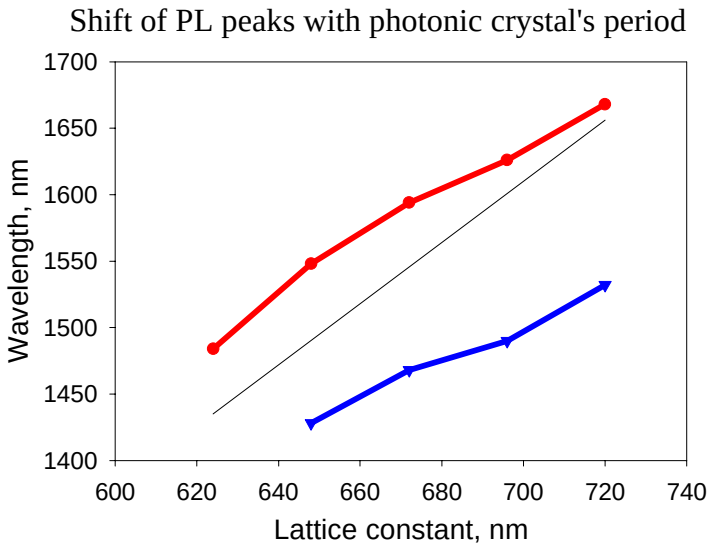

Figure 22: Shift of the photoluminescence peaks with the lattice constant.

It is worth noting also that these peaks are getting blue-shifted as lattice constant decreases. It is especially clear for the sample with plugged holes from Figure 21. The

wavelengths of the major PL peaks for this sample set are plotted versus lattice constant in Figure 22. The wavelengths versus lattice constant nearly follow a straight line. It can be seen also that the spectral shape evolves gradually, with respect to the lattice constant. The complicated structure of the PL spectra in Figures 20 and 21 is a good evidence of the spontaneous emission modification.

5.5. Band structure measurements on photonic crystals.

The 420nm thick sample was the first successfully fabricated photonic crystal with significant photoluminescence efficiency on which angular resolved spectral measurements were performed. We used the spontaneous emission spectral peaks versus angle to study the bandstructure of the photonic crystal. A typical sequence of spectrum corresponding to the various angles of emission with respect to the normal axis is shown in Figure 23 for masks selecting emission at 20, 24 and 28 degrees. Plotting values of the spectral peak positions versus angle mask allows us to re-plot the graph (see Figure 24) on the frequency versus in-plane $k_{||}$ using expressions derived earlier in the chapter. The dashed line represents the light line of the glass substrate. Naturally, all detectable bands

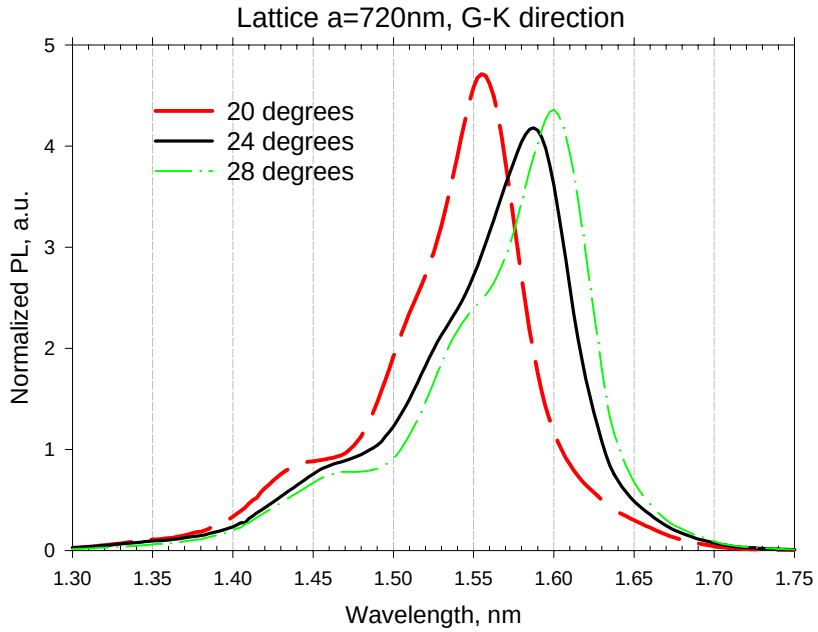

Figure 23: Spectra of photoluminescence corresponding to sequential masks.

above the light line correspond to leaky modes, and that permits us to measure them. All bands of this sample are consistently about 10% below their calculated frequencies. We attribute it to a discrepancy between the geometrical sizes assumed in the calculations and those of the samples. Also, the ion beam etching procedure normally produces slightly tapered holes. In this case that would also increase the effective refractive index of the structure and bring the bands of the dispersion diagram down. The recorded spectrum of the photoluminescence consists of the peaks corresponding to the leaky modes and a broad bell-shaped background corresponding to the emission into the 3D

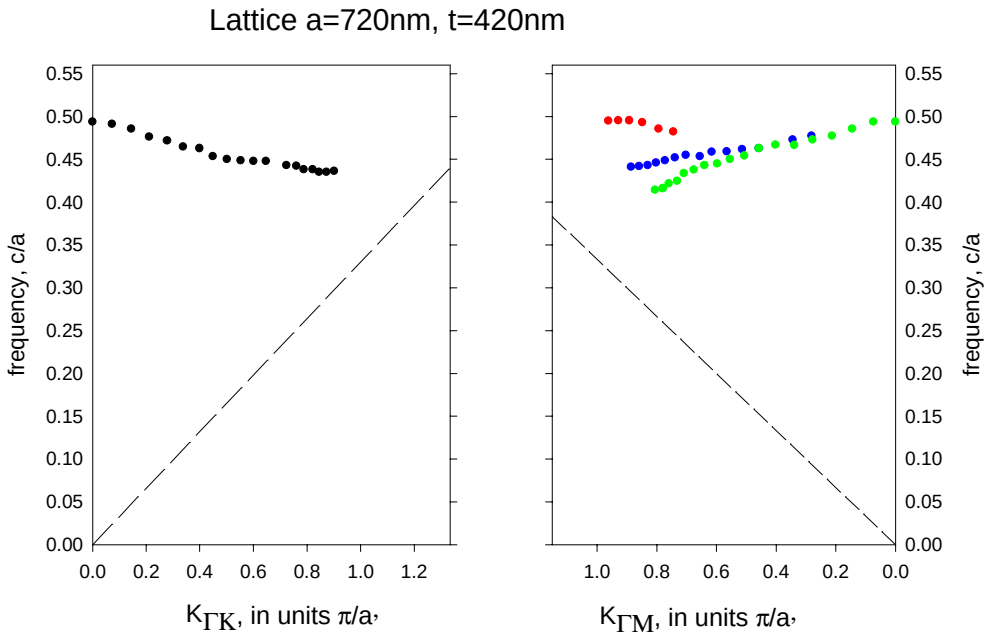

Figure 24. The measured bandstructure of thin slab photonic crystal with lattice constant a=720nm and thickness t=420nm.

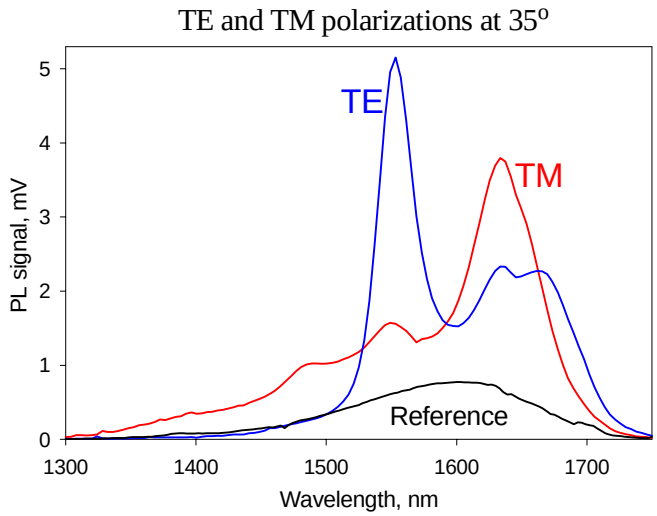

Figure 25. Some modes are well polarized while others are of mixed polarization.

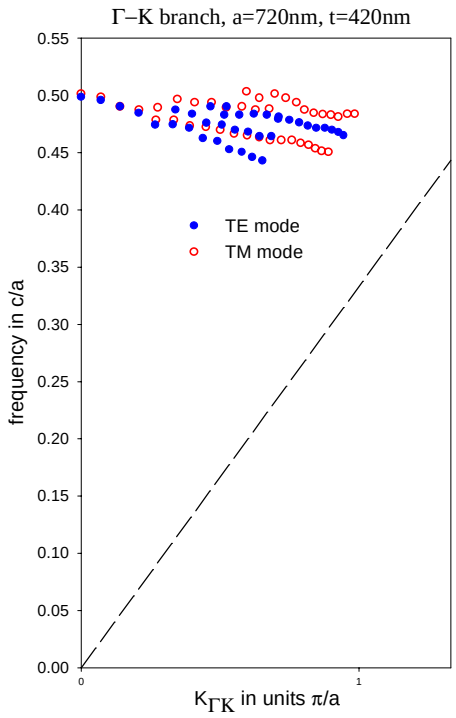

Figure 26: A branch of the dispersion diagram with the polarization indicated

continuum of extended modes. Coupling of the leaky modes, that is modes we are interested in, with the active region of the photonic crystal is determined by the internal structure of the mode. The farther is the mode from the light line the easier it is to detect. Also, some of the conduction band modes of the photonic crystal have their electric field concentrated in the air regions. Thus, electron-hole pairs can not emit efficiently into these modes and it is difficult to observe them.

Our electromagnetic simulations

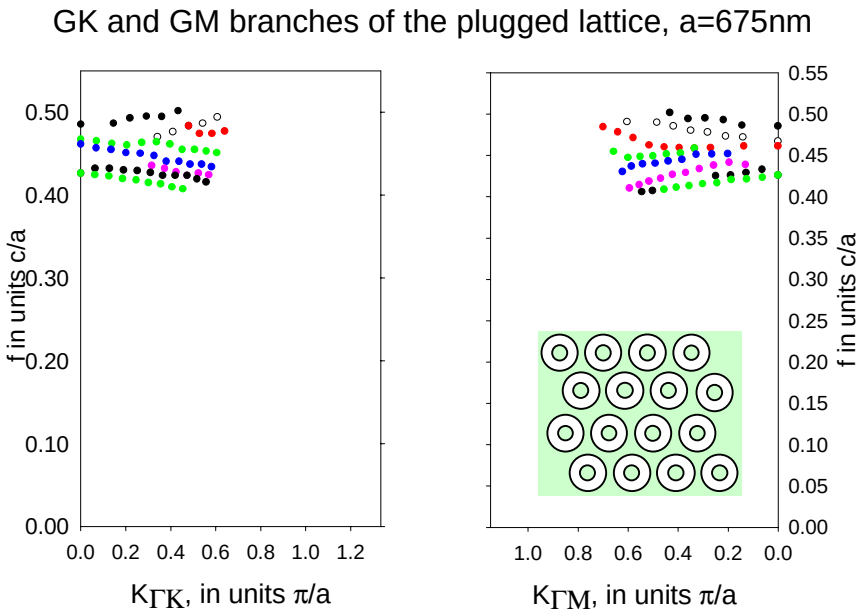

Figure 27. The band structure of a plugged lattice shows peaks evolving nicely with angle, which are nonetheless very difficult to match with the theory.

showed also, that, even though the modes of a thin film photonic crystal can not be classified as pure TE or pure TM, some of them have strongly dominating TE or TM components, while others are truly mixed. If so, the photoluminescence at large angles must be polarized depending on the dominant polarization of a corresponding leaky mode. We used a polarizing beam-splitter to select the different polarizations. As can be seen from Figures 25 and 26, the resolving ability of the setup increased considerably and the broad background turned out to be the consisting of a few clearly polarized (or sometimes mixed) peaks.

Samples with plugged holes presented another interesting subject of study. While the electromagnetic modes of a “traditional” photonic crystal can be subdivided into “air” modes and “material” modes, the plugged holes structure is somewhat analogous to a

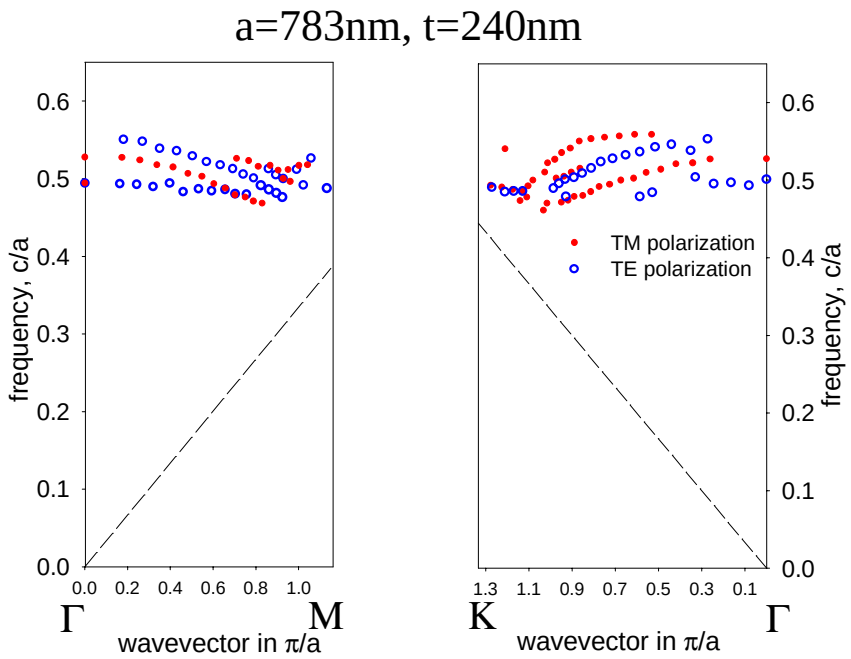

Figure 28. Experimentally measured bandstructure of a photonic crystal. Lattice constant a=783nm, radius of the holes r=260nm, thickness of the slab t=240nm.

diatomic crystal with an extra degree of freedom. It's interesting to see that modes in this crystal can be categorized as "vein", "plug" or "air" modes. For this reason the modal structure of these samples was considerably more complicated as can be seen from its partially measured band structure in Fig 27.

At this point it became clear that thick structures, as well as the structure with the plugged holes whose measured dispersion diagram is shown in Fig. 27 have very dense and complicated band structures. To compute the corresponding theoretical band structure with necessary resolution an enormous amount of computations time would be needed. Furthermore, the actual geometry of the experimental sample would have to be known with great accuracy. Instead, we decided to concentrate our study on the 240nm thick structure. As can be seen from the Figure 28, its dispersion diagram is much

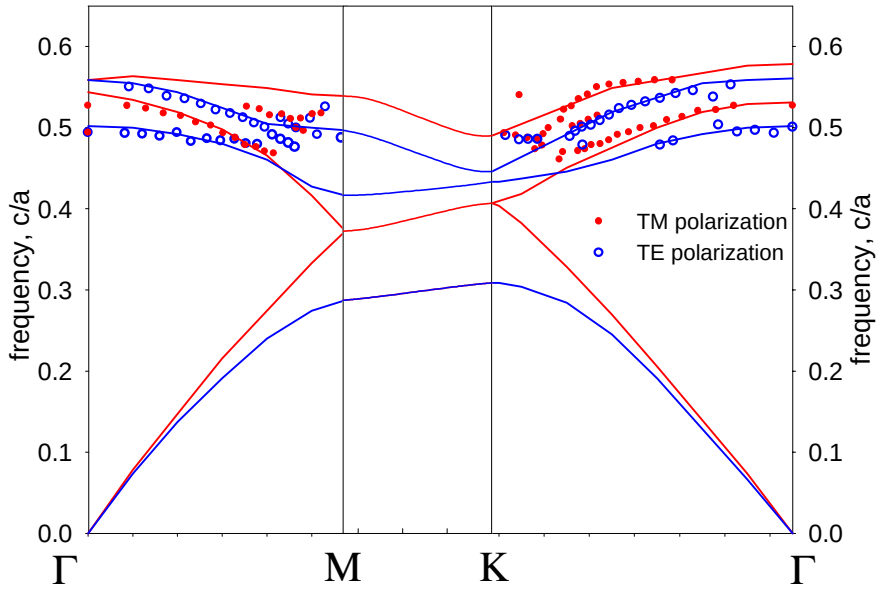

Figure 29. Theoretical bands for the photonic crystal from Figure 28. Red lines correspond to TM-like modes, blue lines are TE like modes.

sparser, hence facilitating both theoretical and experimental identification of modes. Comparing Figure 28 with the computed dispersion diagram for this structure shown in Figure 29, we see a good agreement in the shape of the curves as well as in their polarization. A triangle formed by the crossing of the lowest TE and TM conduction bands is a typical and repeatable feature in a several samples with different lattice constants. This is the first, to our knowledge, demonstration of the spontaneous emission directly into the photonic bands and a first measurement thereof. The fact that the measured band structure lies 3-4% below the computed values can be attributed to a slightly thicker film and the tapering of holes during the chemically assisted ion beam etching process, which were not taken into account in the computation. Measurements on the thinner structure revealed some very sharp peaks (compared to the emission linewidth

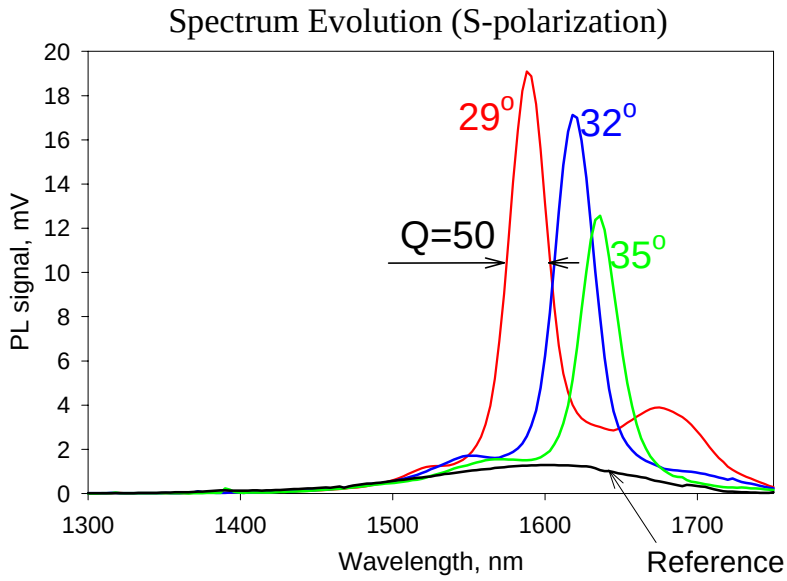

Figure 30. Measured angularly resolved spectra have relatively high Q

of the InGaAs, with a Q between 100 and 30, a feature that was not present in previous experiments. Typical spectra for such a structure are shown in Figure 30. Besides Q~50, another important feature of the figure is a very high peak to background ratio (around 15). In the following section we will argue that these are signatures of the Purcell enhancement realized without a cavity.

5.6. Resonant enhancement in thin-slab photonic crystals

It was shown in the chapter 2 that spontaneous emission in a small cavity happens faster than in the bulk material. Crucial parameters for the speedup were cavity Q and effective volume V_{eff} of the resonant mode:

$$\frac{\Gamma}{\Gamma_0} = \frac{3Q_m g(\lambda/2n)^3}{2\pi V_{eff}} \tag{47}$$

In the photonic crystals studied in the previous section, the measured Q's of modes were comparable to that of a dielectric cavity. Since these modes are large in volume, local field enhancement is much smaller. But since the band structure of upper modes is nearly flat as can be seen from both theoretical and experimental results (Figures 28 and 29), these modes pick up a large degeneracy factor, *g*, compensating the loss in the local field enhancement.

Now we will derive the enhancement of spontaneous emission in a particular direction:

Suppose we have selected a narrow solid angle $\sin\theta d\theta d\phi$ and a frequency range $d\omega$. Then, similarly to the derivation in Chapter 3, we have to compare the density of modes and local fields of the emission into a 3-d continuum of modes to that of the emission into the leaky guided modes.

The spontaneous emission rate is proportional to the local field of the mode $E^2(\mathbf{r})$ (normalized to $h\nu/2$) and to the number of modes ΔN emitting into the given solid angle in given frequency range.

For emission into the 3-d continuum of modes,

$$\mathbf{E}^2(\mathbf{r}) = \frac{\hbar\omega}{2nV} \ , \tag{48}$$

And number of modes emitting into the given solid angle is given by

$$\Delta N_{3d} = 2\frac{k^2 \sin\theta dk d\theta d\phi}{(2\pi)^3} V \ , \tag{49}$$

where k=ω/c is a corresponding wavevector and V=L^3 is the quantization volume.

For the case of emission into the leaky modes, the local field depends on the position of the emission dipole in the active region. We can assume that vertical distribution of the electric field is concentrated in a slab waveguide. Then, the average square of the electric field normalized by a single quantum in a given point is given by

$$\mathbf{E}^2(\mathbf{r}) = \frac{\hbar\omega}{2\int_{slab} \varepsilon(\mathbf{r}')\mathbf{E}_0^2(\mathbf{r}')d^3\mathbf{r}'}\mathbf{E}_0^2(\mathbf{r}) \approx \frac{\hbar\omega}{2(t/2)\int_{slab} \varepsilon(\mathbf{r}')\mathbf{E}_0^2(\mathbf{r}')d^2\mathbf{r}'}\mathbf{E}_0^2(\mathbf{r}) \ , \tag{50}$$

where *t* is the slab's effective thickness and $\mathbf{E_0}$ is the non-normalized electric field distribution of the mode. Integration in the last expression is performed over the center plane of the slab.

The number of modes emitting at this angle is given by a projection of the three-dimensional k-space onto the plane of guided mode wave vectors:

$$\Delta N_{3d} = 2\frac{k_{\|} dk_{\|} d\phi}{(2\pi)^2} A, \tag{51}$$

where $k_{||}=k\sin\theta$, $dk_{||}=k\cos\theta d\theta$ and A=L^2 is the area of the slab.

Averaging over the active region A_{active} in a unit cell would give the total radiation rate in a given direction. However, since the line width of the leaky mode Δω is much larger

than specified spectral resolution dω, only $\frac{2}{\pi}\frac{d\omega}{\Delta\omega}$ of the radiation will be in the spectral range. The 2/π pre-factor comes from the Lorentzian lineshape of the leaky mode, similar to the derivation in Chapter 3.

Thus, rate of background radiation would be given by

$$\Gamma_{3d} \propto \int_{active} \mathbf{E}^2(\mathbf{r})\Delta N_{3d} d^2 r = 2\frac{k^2 \sin\theta dk d\theta d\phi}{(2\pi)^3} V \cdot \frac{\hbar\omega}{2nV} \cdot A_{active} \tag{52}$$

And, in the same way, emission into the leaky modes is

$$\Gamma_{2d} \propto \int_{active} \mathbf{E}^2(\mathbf{r})\Delta N_{2d} d^2 r = \frac{\hbar\omega}{2(t/2)\int_{slab} \varepsilon(\mathbf{r}')\mathbf{E}_0^2(\mathbf{r}')d^2\mathbf{r}'} \cdot \frac{2d\omega}{\pi\Delta\omega} \frac{(k\sin\theta)(k\cos\theta d\theta)d\phi}{(2\pi)^2} \int_{active} A\mathbf{E}_0^2(\mathbf{r})d^2 r \tag{53}$$

Taking a ratio and simplifying we get:

$$\frac{\Gamma_{2d}}{\Gamma_{3d}} = \frac{1}{\pi} \frac{A_{slab}}{\int_{slab} \varepsilon(\mathbf{r}')\mathbf{E}_0^2(\mathbf{r}')d^2\mathbf{r}'} \cdot \frac{\int_{active} \varepsilon\mathbf{E}_0^2(\mathbf{r})d^2 r}{A_{active}} \cdot \frac{\omega}{\Delta\omega} \cdot \frac{\lambda}{nt}\cos\theta \,. \tag{54}$$

Introducing mode's Q=ω/Δω, and a parameter γ to characterize electric energy overlap with the active region:

$$\gamma = \frac{A_{slab}}{\int_{slab} \varepsilon(\mathbf{r}')\mathbf{E}_0^2(\mathbf{r}')d^2\mathbf{r}'} \cdot \frac{\int_{active} \varepsilon\mathbf{E}_0^2(\mathbf{r})d^2\mathbf{r}}{A_{active}} \tag{55}$$

enhancement of spontaneous emission rate at a given frequency can be transformed into a familiar structure of a Purcell number in 1 dimension:

$$\frac{\Gamma_{2d}(\omega)}{\Gamma_{3d}} = \frac{2\gamma}{\pi} Q \cdot \frac{\lambda}{2nt}\cos\theta \tag{56}$$

In semiconductors, the emission band is normaly wider than the cavity linewidth. For that reason Lorentizan in Equation (56) has to be convolved with the semiconductor emission spectrum, as it was done in derivation of Equation (24). This integrates out the $2/\pi$ in the Lorentzian and substitutes Q with the material's Q_m (10 for InGaAs in our case). Then spectrally integrated enhancement in a given direction becomes

$$\frac{\Gamma_{2d}}{\Gamma_{3d}} = \gamma Q_m \cdot \frac{\lambda}{2nt}\cos\theta \qquad (57)$$

In the structure we have studied, the active region covers approximately half of the sample area. In the optimal case, when all electric energy of the mode is concentrated in the semiconductor, the overlap parameter is simpl y $\gamma \approx 2$. This happens close to the Γ point of the Brillouin zone, as can be seen from the computed energy distribution plot in Figure 31. Then, expected peak enhancement, i.e the peak to background ratio of the spectra in Figure 30, in a direction close to the normal would be $\frac{\Gamma_{2d}}{\Gamma_{3d}} \le 2 \cdot \frac{2}{\pi} Q \cdot \frac{1650}{7 \cdot 240} \approx Q$,

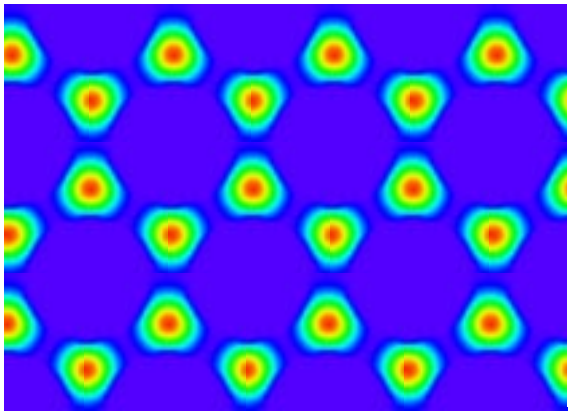

Figure 31. Electric energy distribution in the Γ point of the Brillouin zone. All energy is concentrated in the dielectric veins.

i.e. approximately the modal Q. The observed peak to background ratio is smaller, about 15 to 20. We attribute this discrepancy to two factors: First, the background may be higher due to the contribution of other modal peaks, and, second, the structure imperfections may cause some

additional scattering of the mode.

If the photonic bands could be engineered to be flat compared to the frequency variation across the Brillouin zone, this enhancement would be almost the same for all directions. As can be seen from the experimental and theoretical band structures of the photonic crystal that we considered, the variation of the lowest "conduction" band is approximately twice the spontaneous emission band. Then intergrated over all the angles, the enhancement becomes much smaller, between 3 and five. If the band can be made flat, the radiative lifetime can be made substantially shorter.

In the best of the thin slab photonic crystals, the photoluminescence efficiency was considerably greater than in unpatterned samples. Absolute efficiency calibration can be made by referencing the emission to the reflection (100%) froom a white surface. Such calibration generally show that InGaAs double heterostructures grown by raj Bhat, have an internal quantum efficiency near 100%.

An unpatterned thin film between two glass hemispheres has an optical escape probability of $2\frac{1}{4(n_f / n_g)^2} \sim 0.11$, where n_f=3.2 and n_g=1.5 are refractive indices of the semiconductor film and glass correspondingly. In our ultra-thin films, the effective refractive index is probably slightly smaller than that of the bulk material. Also, the high internal efficiency of the InGaAs active layer allows the photon recycling to boost the external efficiency of the film even higher. With all these benefits combined, we conservatively estimate that a thin film, when encapsulated in glass, can have 12-14% external efficiency. This sets an absolute efficiency scale for the photonic crystal samples shown in the Figure 32b, which were all measured under identical pump and collection

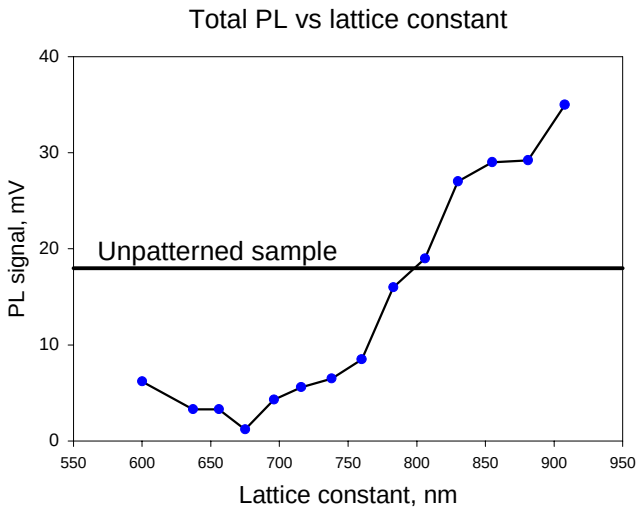

(a)

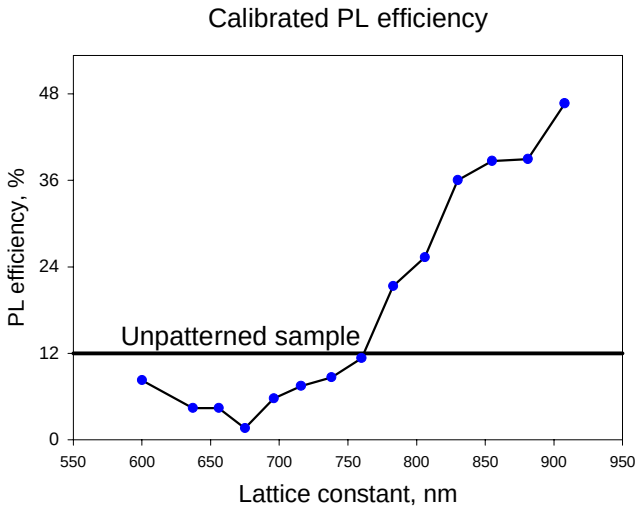

(b)

Figure 32. (a)Photoluminescence from a thin slab photonic crystal with a triangular lattice (raw data). Thickness of the photonic crystal is t=240nm. (b) the same with efficiency calibrated to the reference sample

conditions. The experimental photoluminescence signal versus lattice spacing is shown in Figure 32a . As can be seen from the graph, the PL strength from the photonic crystal samples with lattice constant ~900nm, where conduction band modes match the InGaAs

emission frequency, is twice as large as that from an unpatterned sample. Taking into account that there is only half as much surface area in the patterned PBG samples to absorb light (at least in the geometrical optics approximation), this gives the external efficiency of 48-56%.There are three factors influencing the measured external quantum efficiency of photonic crystal samples:

1. In principle, the extraction efficiency can be unity since all modes are leaky.

2. By drilling the holes through the active region, we introduce a non-radiative recombination. We will show below that non-radiative recombination rate N is comparable to the radiative emission rate R: $N/R \sim 1$, where R is the radiative emission rate in bulk semiconductor material in which there is no Purcell effect.

3. The radiative emission rate in the patterned film is enhanced by the Purcell factor F, a quantity we would like to determine: $R \rightarrow FR$.

Then, the external quantum efficiency of the sample emitting into the conduction band modes of the photonic crystal would be given by the fractional rates:

$$\eta = \frac{FR}{FR + N} = \frac{F}{F + N/R}, \tag{58}$$

which can be solved for the Purcell enhancement factor F:

$$F = \frac{\eta}{1-\eta} \cdot \frac{N}{R} \tag{59}$$

It follows from the Equation (59) that the knowledge of non-radiative recombination rate is necessary to determine the Purcell factor.

We can use the 600-700nm samples emitting into the forbidden photonic bandgap to estimate the non-radiative recombination rate. Indeed, as can be seen from the

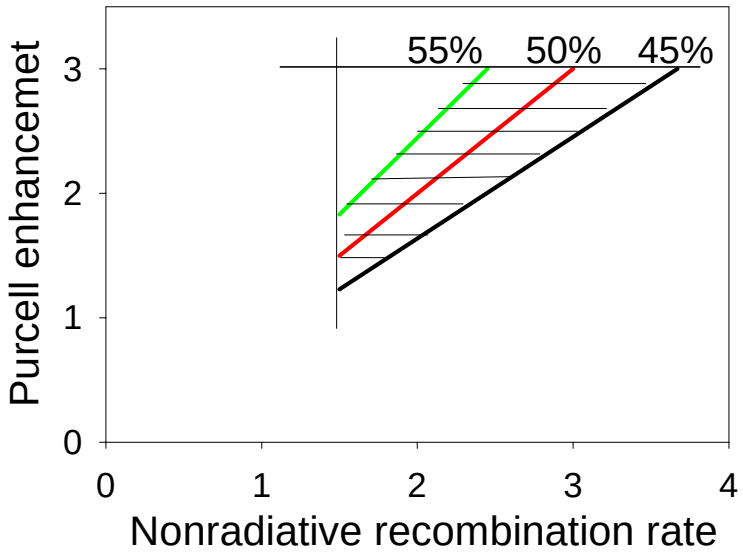

Figure 33. Dependence of the Purcell enhancement factor on the value of the non-radiative recombination rate N/R for different values of external efficiency η=45, 50, 55%. The shaded area limits the possible values of the Purcell enhancement factor. The Purcell factor is constrained by the lower limit on N/R=1.5 from the left, and by the maximum Purcell factor 3 in this kind of structure from the top.

Figure 18, the total photoluminescence signal is 5 times lower than in the unpatterned sample. Correcting for pumped area ratio, a factor of 2 as before, gives us 2.5 times drop in the external efficiency compared to the unpatterned continuous film, as shown if Fig 18a. Using a conservative assumption that the escape probability is the same as in unpatterned film, we obtain an estimate on non-radiative recombination rate N in terms of the radiation recombination rate R:

$$\frac{R}{R+N} < 0.4 \qquad (60)$$

from which follows N/R>1.5. This implies a nonradiative recombination velocity S>20000cm/s, since the absolute rate R is known to be $R=1/\tau=Bn$ with $B=5\ 10^{-10}cm^3/s$ and $n=10^{18}cm^{-3}$, which is consistent with out previous measurement on surface recombination velocity.

The factor 1.5 is a lower limit on the non-radiative/radiative recombination rate because the extraction efficiency of the sample with holes is more likely to increase due to the presence of additional surfaces. Plotted in Figure 33, is a family of curves showing the dependence of Purcell enhancement factor versus (N/R) for different efficiencies from Eqn. (59). As one can see from the Figure 33, the Purcell factor is constrained by our measurements to be above 1.5 but less than the ideal Purcell factor 3 which would occur in the ideal case.

Certainly, we will need to perform lifetime measurements on our samples to verfy the exact value of the Purcell factor for spontaneous emission into conduction band modes.

The expressions for Purcell factor obtained in this section resemble the results for the VCSEL-type structures, the only difference is in the number of resonant modes. In the VCSEL structures the resonator is comprised of a pair of mirrors while in our case the structure provides a standing wave due to its periodicity. Unlike the microcavities with tiny mode volume and correspondingly small active region that we considered in the Chapter 3, the flat photonic conduction bands relatively to the broad emission spectra at room temperature, makes the control over spontaneous emission technologically possible.

5.7. Summary of the photoluminescence measurements.

The results of the photoluminescence measurements on thin slab photonic crystals were presented in this chapter. The angle dependence of the PL spectral peaks was shown to follow the photonic bands of the structures. The band structure of the upper bands was measured using the angular resolved measurements. Up to 15-fold enhancement of the emission in a given direction was observed and explained in terms of the Purcell enhancement.

6. Thin slab photonic crystals for LED applications.

There is a significant gap between the high internal efficiency and poor external efficiency of light emitting diodes, (LED's). Depending on the optical design, the efficiency ratio can be as poor as $4n^2 \approx 50$, (where n=3.5 is the semiconductor refractive index). One may try to implement some new LED design features, that would allow a greater fraction of the internal light to escape. By reducing the parasitic internal optical absorption in LED's, one can extrapolate to an external efficiency >50%. Among the new features that have proved to help external efficiency are: epitaxial liftoff to separate the active epi-layers from optically absorbing substrates and surface nano-structures to induce a chaotic internal light-ray dynamics. Our previous work on LED's efficiency improvement is described in appendix A. It consisted of numerical simulation and optimization of photon escape probability in existing commercial LED structures, and the enhancement of light output from thin film InGaAlP LED structures using texturing. As a complementary study, enhancement of light absorption due to texturing of ultra-thin film solar cells is outlined in Appendix B.

In this chapter we will make an attempt to apply the properties of thin slab photonic crystals, as learned in the previous chapters, towards light-emitting diode design. It has been shown that all modes with frequencies above the light-cone are leaky. Certainly it is tempting to use this property to extract light from the high-refractive index material. In principle one can think of using the bare photonic crystal as a light emitting diode. However it will be difficult to attach contacts to such a delicate structure. Also, even

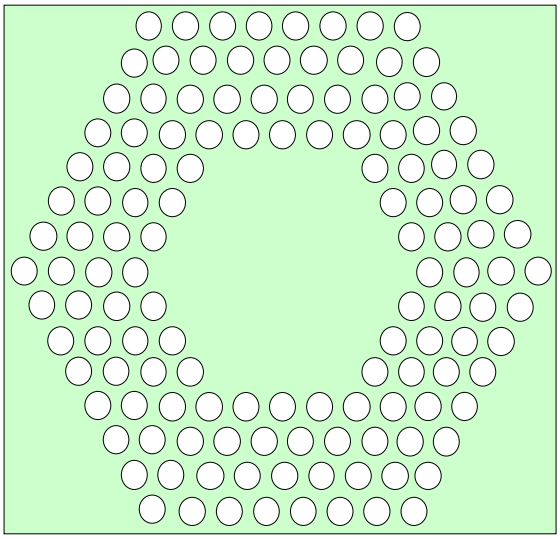

Figure 34. A schematic of an LED structures. The structure consists of an unetched region surrounded by a thin slab photonic crystal, which scatters guided light. into the space.

though the photoluminescence from the photonic crystals studied in Chapter 5 is larger than in a planar sample, it would be much better to have an active region free from the non-radiative surface recombination losses. In other words, it is a reasonable idea to separate regions where the light is extracted from those where the light is generated. The structure shown in Fig. 34 is a hexagon of unetched material surrounded by the photonic crystal. The light is generated in the center region, small $1/2n^2$ fraction of it is emitted and the rest is trapped in the waveguide. It is easy to estimate that the re-absorption length in the 0.4μm thick film, with a 200Å active region, is about 15μm. In high-quality materials, this length can be even larger due to the re-emission process. If the dimensions of the photonic crystal are chosen such that spontaneous emission band of the active

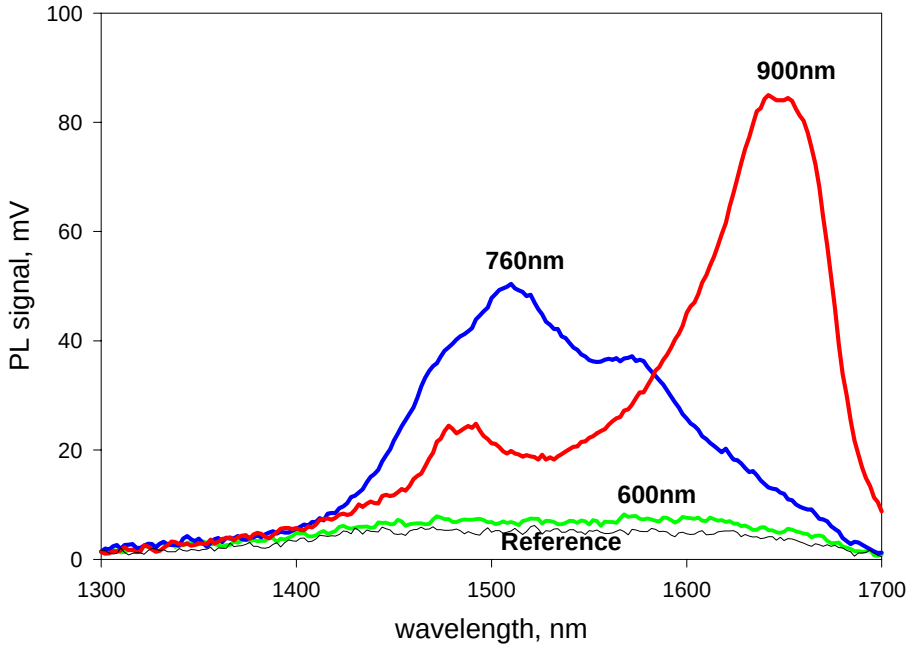

Figure 35. Angle-integrated spectra of the LED structure. The peak wavelength is red-shifted for larger lattice constants.

material overlaps with the leaking modes of the photonic conduction band the light can be efficiently scattered out of the semiconductor. The leakage length of the guided modes has to be shorter than re-absorption length in the photonic crystal. Voids reduce the effective absorption of the photonic crystal, and the leakage length of conduction band modes decreases as the bands move up away from the escape cone. Thus, for sufficiently large lattice spacing guided modes can escape before being re-absorbed.

In these experiments, we compared spontaneous emission from an unpatterned optically pumped region surrounded by a few rows of photonic crystal. The lattice spacing, *a*, of the photonic crystal was 600, 760 or 900nm. According to our band

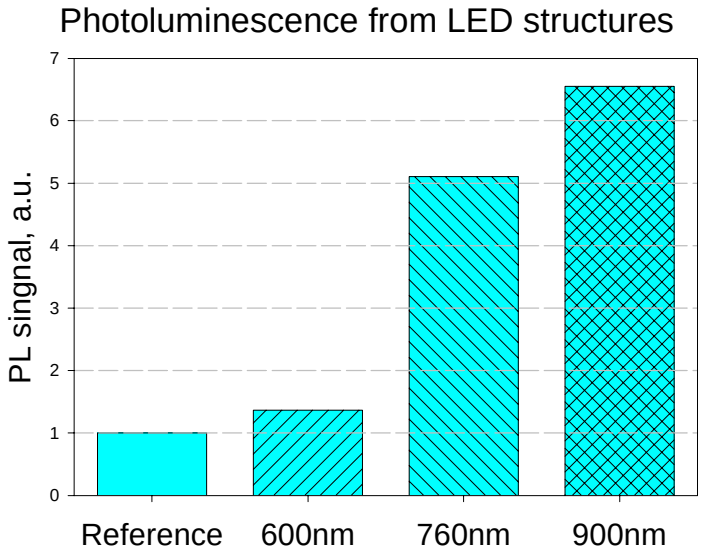

Figure 36. Comparison of PL efficiencies from LED structures with different lattice constants.

structure calculations, in the *a=600nm* sample, guided TM modes overlap with the emission band. For the *a=760nm* sample the emission band overlaps with both guided TM and leaking conduction band modes of the photonic crystal. For the *a=900nm* sample all spontaneous emission should couple to the leaky modes, and thus to free space. The PL spectra of these samples are shown in Fig. 35 along with the spectrum of an unetched reference sample. The photoluminescence acceptance angle was 0 to 45^{o} in the air.

The spectrum of the *a*=600nm sample resembles that of an unetched thin film and has almost the same intensity. Indeed, even though emission is into guided TM modes, there is no way for the light to escape. The PL signal from the sample with a=760nm is about 4 times larger. Shape of the spectrum is different, there are two distinct shoulders. This

measurement was done without angular resolution, so some finer spectral features may be missing.

Finally, the sample with the *a=900nm* hole spacing showed even higher overall efficiency. It is worth noting, that in this measurement, only the unpatterned center area was pumped, and thus pumping condition remained identical for all samples. The spectrally integrated areas are summarized in Figure 36. More than six-fold improvement in light extraction was achieved using the photonic crystal around the edges of an active semiconductor film. This result on periodic structures complements the previous work on random texturing described in Appendix B. One of the advantages of photonic crystals is that, due to the coherent scattering, they provide a shorter escape length. That means that this method can be used in materials with internal quantum efficiencies too low to tolerate re-absorption.

7. Summary

Let me summarize the work described in this thesis:

We studied experimentally and theoretically the modification of spontaneous emission in semiconductor photonic crystals at room temperature. Small material Q_m of semiconductors together with the large surface recombination velocities make observation of these effects an interesting and challenging task.

A quantum electro-dynamical model was developed to estimate enhancement of spontaneous radiation rates in photonic crystals and microcavities. Extensive numerical computations were employed to calculate the band structure of thin slab photonic crystals and modal properties of microcavities. The minimal effective mode volume, a parameter crucial for cavity enhancement of spontaneous emission was found to be $2(\lambda/2n)^3$ where λ is the resonant wavelength and n is the refractive index. A possible 5-fold enhancement of spontaneous emission rate (Purcell effect) was shown to be possible in InGaAs microcavities at room temperature under the most optimistic conditions.

Photoluminescence measurements were used in the search of the material system most suitable for fabrication of such a photonic crystal. It was shown that the InGaAs/InP and InGaN material systems are good candidates for opto-electronically active photonic bandgap structures.

Angularly resolved photoluminescence measurements were used to measure experimentally the band structure of conductions band of such a photonic crystal and overall enhancement of spontaneous emission.

Spontaneous emission enhancement in thin slab photonic crystals was demonstrated. It was shown that emission into the leaky conduction bands of the crystal has the same effect as cavity-enhanced spontaneous emission provided these bands are flat enough relative to the emission band of the material.

Structures described in Chapters 5 and 6 have a good potential to be used in real-world light-emitting diode designs. Issues of ohmic contacts and packaging were not addressed in this work, although these are important aspects of a final product fabrication.

Recommendations for novel LED designs were worked out based on the results of this study.

Appendix A: Modeling of Light-Extraction Efficiency of Light-Emitting diodes

This appendix concerns itself with device design and fabrication concepts which increase the efficiency of a light-emitting diode (LED), a performance parameter of quite general importance especially in portable applications. This sub-project was initiated at the request of the Hewlett-Packard opto-electronic division. Good efficiency potential is already present in these materials. In terms of luminescent quantum efficiency, at room temperature, direct gap double hetero-structures are rather unique substances. It has been known[31] for almost 20 years that good quality III-V double heterostructures can have high internal quantum yields, well over 90% efficient. Indeed, it had been recently shown[32] that these internal quantum yields can sometimes exceed 99% efficiency. The main problem in LED design has always been to convert the impressive internal quantum yields to external efficiency.

The reason for the discrepancy between internal and external efficiencies is the difficulty for light to escape from high refractive index semiconductors as illustrated in Fig. 1(a). The escape cone for internal light in a semiconductor of refractive index n=3.5 is only 16°, as imposed by Snell's Law. This narrow escape cone for spontaneous emission covers a solid angle of $\approx(1/4n^2)\times 4\pi$ steradians. Thus a mere 2% of the internally generated light can escape into free space, the rest suffering total internal

reflection and risking re-absorption. An unsophisticated LED design would be only 2% externally efficient, even when the internal efficiency is 100%.

There is no easy solution to the total internal reflection problem. For example, if an anti-reflection coating is applied to the semiconductor surface, then the escape cone would apparently be broadened. But then there would be a second escape cone from the coating material into free space as illustrated in Fig. 1(b). Some of the rays would escape from the semiconductor only to be trapped by the anti-reflection coating. The net effect of a 2-fold hierarchy of escape cones is that the same fraction $(1/4n^2)\times 4\pi$ steradians of the light manages to escape. The determining parameter is the overall refractive index ratio (n÷1) between medium in which the light is generated, and the medium where we want the light to end up, (free space).

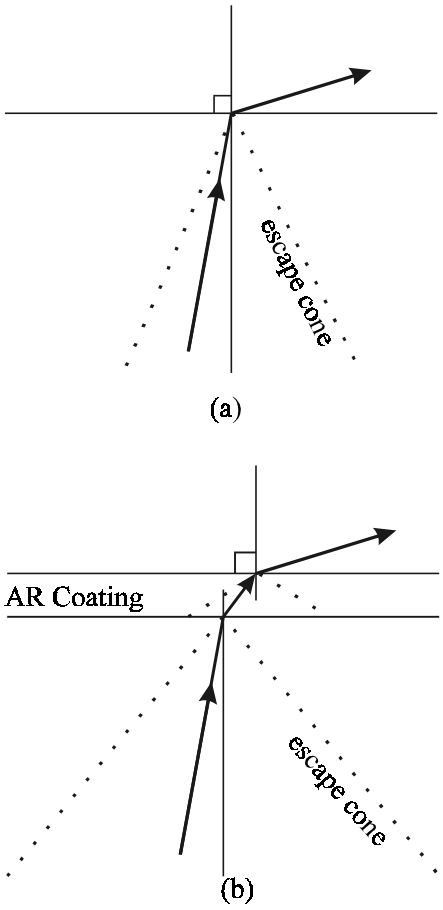

Figure A1: (a) Transmission of light within the escape cone. (b) In the presence of an anti-reflection coating, there are two successive escape cones, but net escape angle is the same as in (a).

It is paradoxical that total internal reflection can co-exist with an anti-reflection coating. Indeed the anti-reflection coating has no net effect on the

overall total internal reflection. An anti-reflection coating merely reduces the Fresnel reflectivity for those rays inside the narrow escape cone, rays which are capable of escaping in any case. On the other hand, those rays outside the escape cone are totally internally reflected irrespective of any thin coating on the surface.

To effectively address the problem of the narrow escape cone requires a change in the geometry of the high index material. Early on, it was recognized that a hemispherical dome[33] made of high index semiconductor material, centered on the LED, would allow all the light to exit the surface at normal incidence. Unfortunately, a lens made of low index material such as epoxy, is only partially and incompletely effective.

Until now, the cost of a hemispherical semiconductor lens has been such that they have not been used commercially. Instead, a different physical principle allows light to escape from inside an LED. This principle, of chaotic propagation of light, is illustrated in Fig. 2. The idea is that a light ray experiencing chaotic dynamics inside a semiconductor will eventually find the escape cone. Sometimes this form of optics[34] is called "Statistical Ray Optics", and it was originally developed for understanding the trapping of light inside solar cells. Today, all record-breaking solar cells make use[35] of this concept. An LED is an inverse solar cell, and similar ideas were put forth for LED's by Joyce et al[36] over two decades ago.

In a plane parallel semiconductor sheet light is spontaneously emitted beyond the angle of total internal reflection. Such internally reflected light bounces back and forth endlessly between the two surfaces, never escaping. If one of the surfaces is textured, the light ray direction is randomized with each reflection off the textured surface. Each such

random reflection allows a 2% probability that the light will happen to catch the escape cone on the next pass. In this way the light eventually escapes. Chaotic dynamics is simply restored by a deviation from perfect symmetry, allowing internally generated light to escape! The lesson is break the symmetry and you will help the LED efficiency. An intentional texture on the semiconductor surfaces of the LED is one of the simplest ways of helping the light to escape.

1. Statement of Problem.

The chaotic dynamics approach for allowing light to escape from an LED imposes certain design requirements. The most important is, the long internal path length required, before the light escapes. Given the $(1/4n^2)\approx 1/50$ probability of escaping per surface reflection, the internal path length is required to be at least 50 times larger than the thickness of the semiconductor. Thus the main requirement for high LED efficiency, once chaotic dynamics is achieved, is a very low parasitic absorption as the light scatters around internally in the device. Optical design for low parasitics emerges as one of the main requirements for LED efficiency. Indeed one of the worst practices is to build an LED on optically absorbing substrate, e.g. a visible LED on a GaAs substrate. There is a current trend toward transparent superstrates and transparent substrates, by strained hetero-epitaxy[37] and by wafer bonding[38] respectively.

The leading manufacturers such as HP have commercialized red LED's having external efficiencies above 20%, and occasionally reaching 30%. These high brightness LED's represent a major improvement over the original generation of LED's, but there is room for further optical sophistication in getting the light out of these materials.

2. Photon gas simulations

A model of optical processes in LED's was created that takes into account device geometry, light absorption in contacts and cladding layers, photon recycling, light randomization due to surface scattering and the benefit from encapsulation of the device into epoxy. Here we report results of the light extraction efficiency modeling using the photon gas method and Monte-Carlo simulations.

Based on the results of our modeling, an optimized LED design was proposed. Also, to determine parameters for the model, photoluminescence measurements of internal quantum efficiency were performed on the epi-layers used for LED fabrication.

A photon gas model[37] based on the statistical properties of the completely randomized photons in the semiconductor device, allows one to make estimates of the dependence of the LED light extraction efficiency. This will depend on quality of the active layer material and geometric parameters such as aspect ratio and thickness of active layer. We consider a square chip with dimensions width L and height H, with the active layer of thickness d in the middle and reflecting electrical contacts on the top and bottom surfaces covering area $A_{contact}$. Top and bottom surfaces are assumed to be polished while four side edges are rough saw-cut. This design is similar to that used by HP Opto-Electronics Division in fabrication of visible LED's based on InGaAlP quaternary alloys[38], with L~200μm, H~250μm and d~1μm.

The photon flux inside the LED is:

$$I=[\text{Density of photons inside LED}]\cdot\frac{c}{n},$$

where n is the refractive index of the semiconductor,

There are four ways for a photon to disappear from an LED:

a) For the portion of photon whose direction falls in the escape cone, the escape rate will be proportional to the surface area and the escape fraction $1/(4n^2)$:

$$A(\lambda) = \frac{(2L^2 + 4LH)T}{4n^2} I(\lambda)$$

b) There is a chance that photon traveling in the bulk of the device is absorbed in the cladding layers or in the current spreading window due to free carrier absorption in the volume:

$$B(\lambda) = L^2 H \alpha(\lambda) I(\lambda),$$

Where α_{fc} is free carrier absorption coefficient in the bulk

c) Some of the photons can be reabsorbed in the active region. Some part of the photons, proportional to the internal quantum efficiency, can be re-emitted. The balance produces electron hole-pairs which recombine non-radiatively:

$$C(\lambda) = \frac{L^2}{4\pi} \int d\Omega (1 - e^{-\frac{\alpha d}{\cos\theta}}) \cos\theta (1 - \eta_{int}) \sin\theta \cdot I(\lambda)$$

where T is average transmission coefficient (within the escape cone), $\alpha(\lambda)$ - absorption coefficient of the active layer and η_{int} - internal quantum efficiency.

d). Finally, since contacts are not very good reflectors, there will be losses due to absorption in contacts. The absorption rate due to this process is:

$$D(\lambda) = \frac{A_{contact}}{4\pi} \int d\Omega \cos\theta (1 - R_{contact}) \sin\theta \cdot I(\lambda)$$

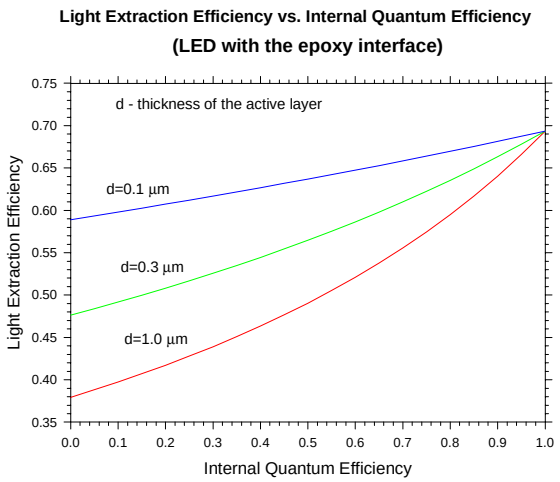

Figure A2: The total efficiency is the product of the internal quantum efficiency times the light extraction efficiency. However the light extraction efficiency is itself dependent on the internal quantum efficiency due to the inevitable re-absorption of some of the light. In thin LED's the re-absorption effect is less severe.

The light extraction efficiency $\eta_{extr}(\lambda)$ is the ratio of the desired rate to the sum of all rates.

$$\eta_{extr}(\lambda) = \frac{A(\lambda)}{A(\lambda) + B(\lambda) + C(\lambda) + D(\lambda)}$$

In a given device, different wavelengths have different escape probabilities, which means that result must be weighted by spontaneous emission spectrum $R(\lambda)$ which can be derived from the absorption spectrum using the Shockley-van Roosbroeck relation[39]. Thus extraction efficiency is given by

$$\text{Extraction Efficiency} = \frac{\int R(\lambda)E(\lambda)d\lambda}{\int R(\lambda)d\lambda}.$$

Simulation, using second method, the Monte-Carlo approach, takes into account details of the LED design, such as the properties of the surfaces of the device, position of the active layer within a device, reflectivity and configuration of contacts, etc. Furthermore, the second method allows determination of the light distribution pattern over the facets of the LED.

Analysis of the results of our modeling leads us to a number of conclusions:

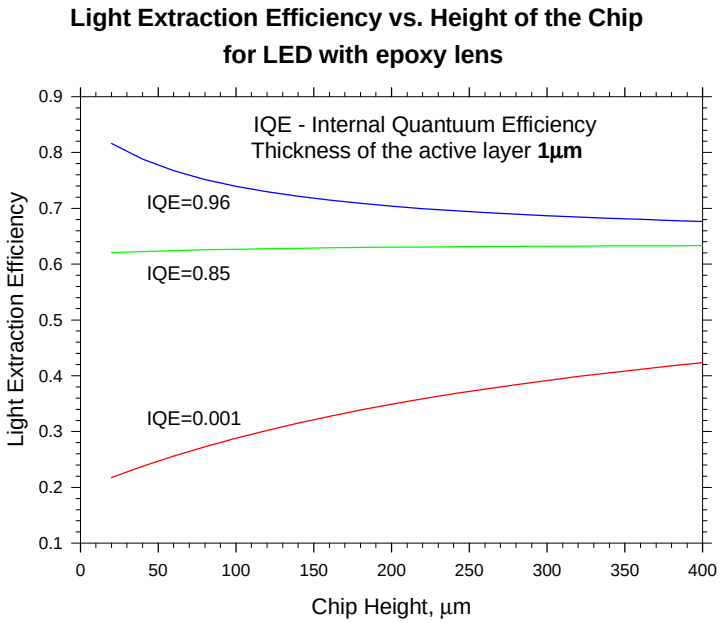

Figure A3: The extraction efficiency versus LED chip height. For the highest internal quantum efficiency (IQE) material, the LED should be a thin film, but for lower quality material a thick LED is better because the light escapes more readily from the edges.

Thinning down the active layer reduces considerably the re-absorption losses in the active layer, especially in material with low internal quantum efficiency (see Fig. 2). This can also shift the operating point of the device towards the high-level injection regime. However a thin active layer suffers if the double hetero-structure barriers are low as in InGaAlP. That effect was not taken into account in this model.

Quality of the active layer material determines whether the preferred device design should be thick or thin (see Fig. 3). For a high internal quantum efficiency device (>90%), one should minimize bulk absorption by making the device as thin as possible. (This requires that a light randomization mechanism such as nano-texturing be incorporated in the device, or that photon recycling be used for additional randomization

of light.). On the other hand, if the active layer has a low (<90%) internal efficiency, it's better to make a thick substrate device which allows the photons to see the device edges where four additional escape cones are present. This increases the photon to escape probability from the semiconductor on the very first surface bounce.

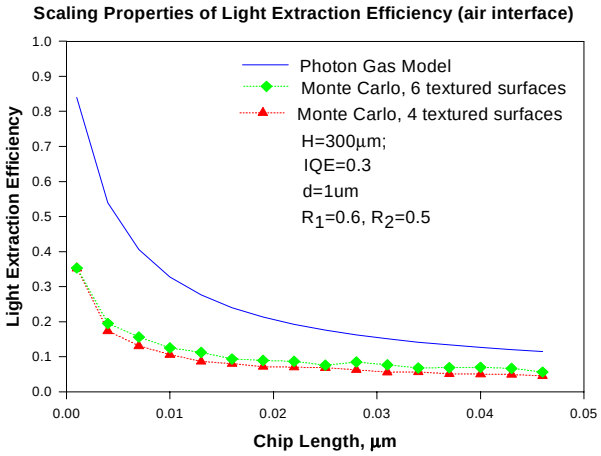

Figure A4: Scaling properties of the light extraction efficiency. When imperfect contacts are introduced into the LED design, photon gas model gives overestimated results for light extraction efficiency.

3. Monte-Carlo Simulations of light extraction efficiency

The photon gas model is a good approximation when the average photon path consists of many bounces inside the LED. When low quality contacts are introduced on the top and bottom surfaces of the LED, a comparison of the photon gas model with the Monte-Carlo simulation shows a difference (Fig. 4). Nonetheless the qualitative scaling

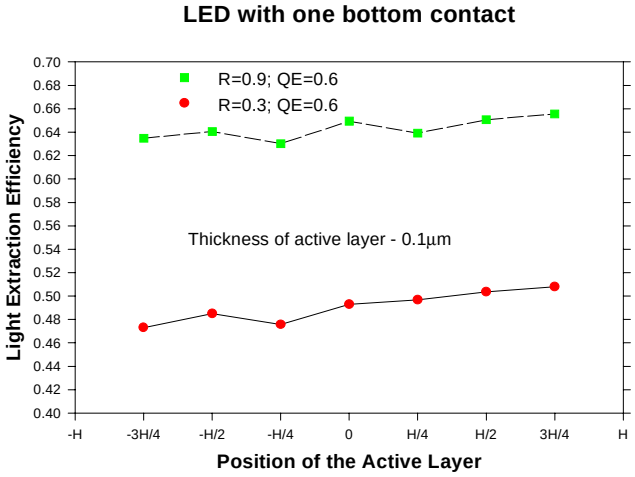

Figure A5: Dependence of light extraction efficiency on position of the active layer for a device with a sheet bottom contact and a small circular top contact

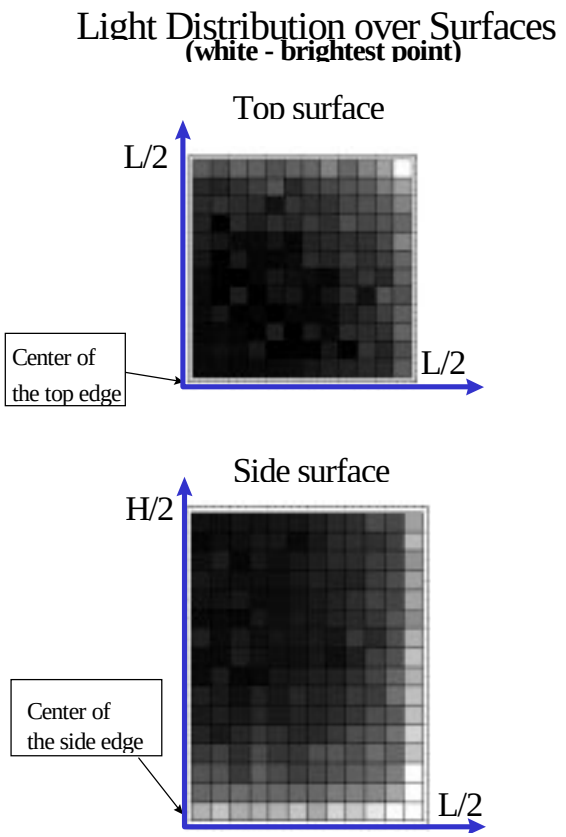

Figure A6: Monte-Carlo results. Top and side views of light escaping from an LED. The white areas have more light emission than the dark ones.

properties of the LED's light extraction efficiency is calculated correctly. From the point of view of light extraction efficiency, a smaller device area is preferable, since light randomization occurs only on the edges of the device.

Even though contacts cover only about 15% of the area of the device under consideration, the dependence of light extraction efficiency on the contact reflectivity is strong (Fig 5). Indeed, for a 50% reflective sheet contact, every probability of contact absorption causes ~7% loss, which is comparable with $6x(1/n^2)$~ 12%.

We considered the optimal position of the active layer for the device with sheet contact on the bottom and small circular contact on the top surface. Modeling (Fig 6) show that bringing the active region closer to the smaller contacts results in up to 6% improvement in the extraction efficiency. Of course, we can not make the active layer too close to the top surface, since we use that upper layer for current spreading.

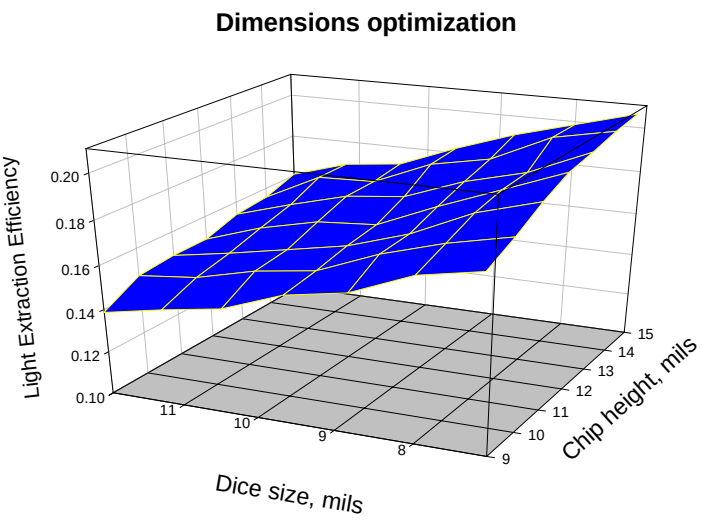

Figure A7: Variation of the size around commercial dimensions

Light output is higher near the edges of the surfaces adjacent to the roughened sides of the device. This is due to the fact that the texturing at the edges scatters some of the light directly into the escape cone. Obviously, better performance would be achieved if all the surfaces were textured, not only the edge surfaces. Obviously, one should go to great pains to design no optical obstructions anywhere near the edges and corners of the LED's facets because that's where the light is getting out.

The Monte Carlo simulation program was modified later to allow modeling of light extraction efficiency associated with additional texturing of the top and bottom surfaces of the LED and due to the introduction of the blocking layers under the top contact. Additional calculations were done to optimize the light extraction with respect to small variations of the device dimensions around their commercial values. Also, the results of measured internal quantum efficiency, presented earlier, were corrected to account for photon recycling.

Figure 7 represents the results of modeling light extraction efficiency of an epoxy encapsulated LED in the parameter plane of dice size and chip height. Calculations were

done for an LED with internal quantum efficiency 0.7, with circular top contact of radius 55 microns and reflectivity 0.6 and sheet bottom contact with reflectivity 0.5. Bulk absorption was taken to be 6 cm^{-1} and absorption in the active layer was taken to be 10^4 cm^{-1}. One can see that light extraction efficiency increases monotonically with the height of the chip and decreases with the length.

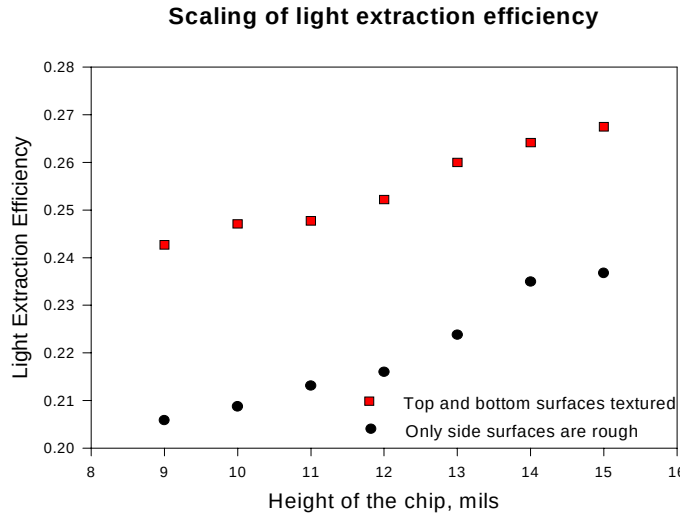

(a)

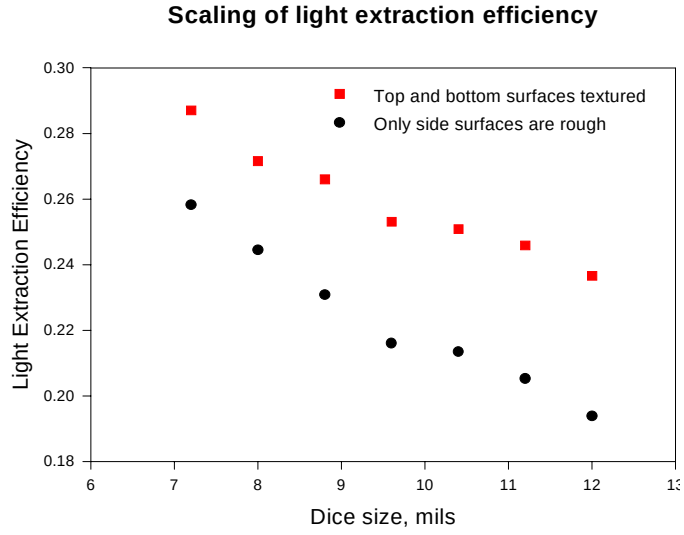

(b)

Figures A8(a,b) : Effect of additional texturing on light extraction efficiency

Figures 9a and 9b show the effect of additional texturing on the light extraction efficiency. If light can be scattered from the top and bottom surfaces of the device, it may significantly increase escape probability of photons. According to our modeling, this texturing can boost device efficiency by 10-15% of its initial value.

Finally, we studied the possible change in LED performance due to incorporation of current blocking layer under the top contact. However, modeling did not show any significant improvement in the light extraction efficiency if blocking layers can absorb light.

4. Conclusions

Light extraction efficiency of LED's were calculated using photon gas model and Monte-Carlo simulations. Recommendations were made to HP's Opto-electrocnic division for the design optimization, based on the results of the modeling.

Appendix B: Absorption Enhancement in Textured AlGaAs Films for Solar Cells

Introduction:

We have studied light randomization and the absorption enhancement in textured ultra-thin $Al_xGa_{1-x}As$ films, with a thickness corresponding to a few optical wavelengths. We call this the "wave limit" of light trapping as opposed to the geometrical optics limit that was studied before. A correlation between the degree of light randomization and trapping, with the scale length of the texturization geometry was found. The observed absorption enhancement corresponds to 90% randomization, or 90% of the best possible theoretical value. A modified photon gas model is proposed to calculate the light trapping and absorption at the band edge in the textured ultra-thin films.

It was proposed in late 1970s and early 1980's that light trapping by total internal reflection could be used to increase light absorption in semiconductor wafers. Several techniques were developed, such as natural lithography[40], metal islands[41] and anodical etch of the porous silicon[42] to texturize thin silicon sheets for light trapping. Yablonovitch[34] showed, that in the low absorption limit, total randomization of the light leads to the enhancement of absorption by the factor of $2n_f^2$**,** where n_f is film's refractive index. These results were confirmed experimentally by Deckman *et al*[43] by applying the natural lithography technique to amorphous silicon films. However, at the moment there is no theory for angular dependence of light scattering from surfaces

produced by this process because perturbation methods require that the ratio of roughness height to the wavelength be small[44] while the quasi-classical small slope approximation[45] require a relatively smooth surface.

In this paper we report results of our study of light randomization and absorption enhancement in ultra-thin GaAs/AlGaAs films with a thickness of only a few optical wavelength. This is the first study of light trapping in a direct gap semiconductor in the wave limit, where geometrical optics does not apply. The ultra-thin films were textured using the natural lithography while varying the density of cylindrical surface structures. A modified photon gas model, which successfully describes the absorption at the band edge will be presented.

The sample preparation method is by Natural Lithography: A GaAs/AlGaAs double hetero-structure wafer (see Table B1) is patterned with commercially available carboxylate modified 0.95μm polystyrene spheres. The sphere solution is first diluted with methanol to 1% concentration by weight and then surface deposited by dropping a small solution

Table B1. Structure of the GaAs/AlGaAs quantum well wafer

GaAlAs	0.32 μm	window layer
GaAs	0.20 μm	active layer
GaAlAs	0.44 μm	window layer

AlAs	0.05 μm	sacrificial layer
GaAs	>100 μm	substrate

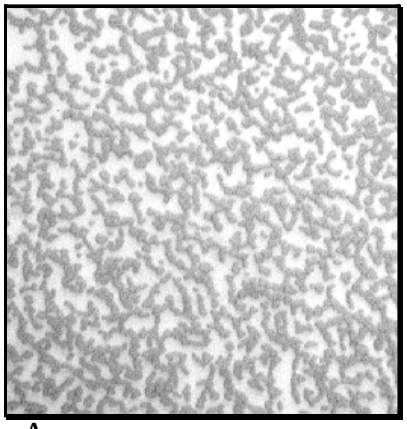

A.

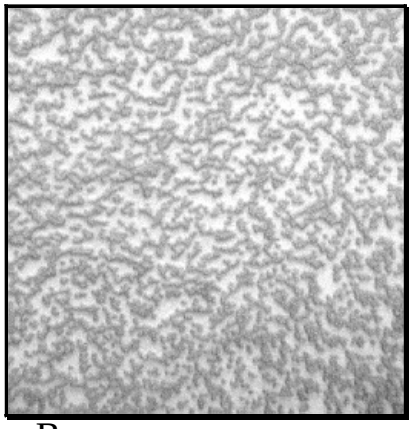

B.

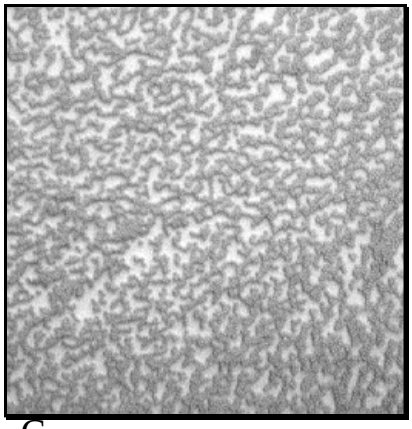

C.

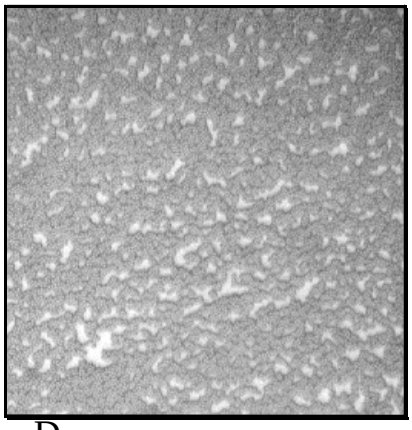

D.

Figure B1: Variation of sphere density with angular velocity. The concentration of polystyrene spheres solution in methanol solution is 1.5% by weight. The darker area represents spheres. The spheres tend to cluster at higher surface concentrations. A) Sphere distribution for 1800 rpm; B) Sphere distribution for 1700 rpm; C) Sphere distribution for 1600 rpm; D) Sphere distribution for 1550 rpm.

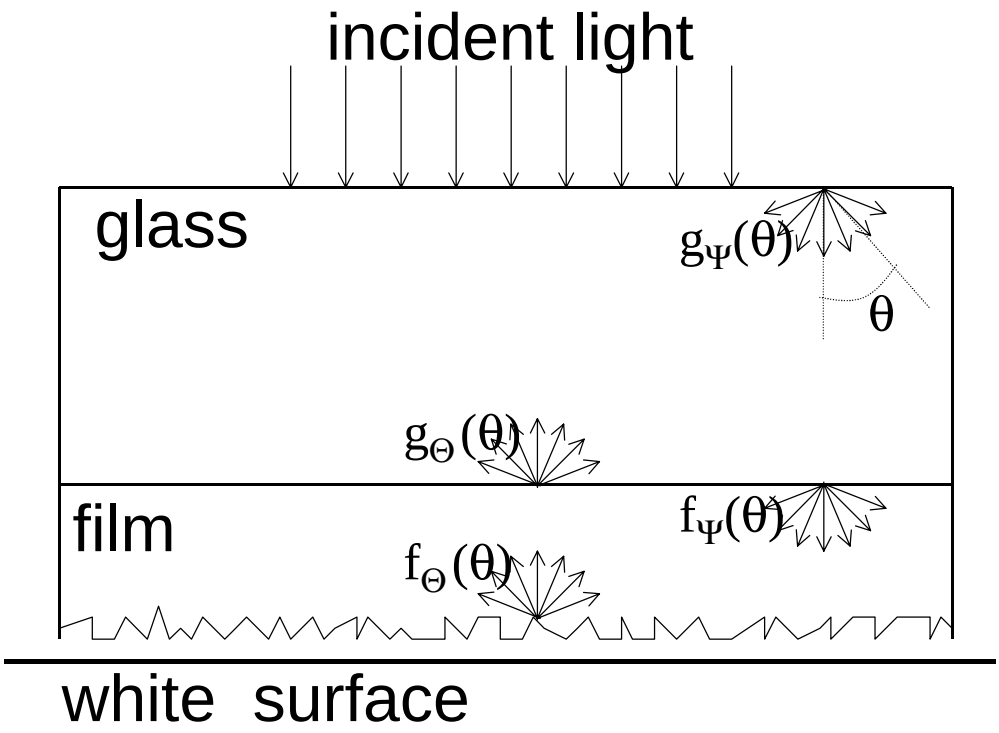

Figure B2: Experimental configuration and definition of the variables used in the modeling.

droplet on the wafer and spinning the wafer at 1500-2000 rpm. The wafer is spun to distribute the spheres across the surface, and to allow the methanol to evaporate. The sphere solution concentration and the revolution speed were varied until the conditions were found such that approximately 50% of the wafer area is covered by spheres. From Figure 1a-d, the effect of varying the angular velocity on sphere areal density can be seen (while holding constant the sphere concentration in solution). The resultant sphere density distribution does not vary significantly across the surface of a given sample. The key point is to avoid building up multiple layers of sphere, which totally coat the surface and provide no patterning. When the desired sphere distribution is obtained, the sample is etched using the chemically assisted ion beam etching process to transfer a

pattern, using the spheres as a lithographic mask. In our work the transferred pattern consists of 0.25μm high mesas, which is approximately 3/4 of the thickness of the top AlGaAs layer. Following etching, the top three epitaxial layers (~1μm) of the wafer, containing the active layer of the device, are removed from the substrate using the epitaxial lift-off procedure (ELO)[46]. The wax supported sample is then bonded to a glass slide with the untextured side against the glass by using a UV curable polyurethane adhesive. The spectral reflectance, R(λ), of the textured and untextured film was measured over a white surface using a standard integrating sphere setup. Then, absorbance of the sample simply becomes:

$$A(\lambda)=1-R(\lambda), \qquad (1)$$

since there is no transmission outside of the sphere. Samples were held horizontally by gravity so that no optically absorbing adhesive materials were necessary inside the sphere. In all our measurements, the probe beam was incident on the glass side with the semiconductor film on the rear, as shown in Figure 2. In this configuration specular reflections from the glass-air and the semiconductor/glass interfaces were identical for the textured and untextured samples. Thus, reflectivity at the front surface was unchanged, since the texturing was at the rear surface. In all the textured samples, an increase in absorption was measured in comparison with the untextured films (see Figures 3&4). The maximum theoretical absorption, which can be attained is ≈80% due to incident beam reflectivity from the glass/air (4%) and semiconductor/glass (16%) interfaces. The best results were attained for samples, which were coated by approximately 50% area coverage of polystyrene spheres and the corresponding

0.25μm high mesas. An absorbance increase from 45% up to ≈75% of a maximally achievable result occurs for the sample in Figure 4 near the band edge. In our best samples, the experimental value nearly reaches the maximum absorbance predicted by theory, as can be seen in Figure 5. The absorbance oscillations, which occur for photon energies above the bandgap, are due to Fabry-Perot fringes. The damping of these Fabry-Perot oscillations in the textured film is an additional evidence of light randomization produced through surface texturization. At energies below the bandgap, free carrier absorption is enhanced from <1% up to the level of ≈20%. Unfortunately, this produces heat rather then electron-hole pairs.We now describe the photon gas model:

Consider a system consisting of the semiconductor film of thickness *d* with absorption coefficient α and refractive index n_f attached to a glass slide with the index of refraction n_g (as in Fig. 2). One surface of the film (opposite to the glass) is textured and lies adjacent to the white reflecting surface so that incident monochromatic light enters the film after passing through the glass slide. We assume that all photons which reach the textured surface and white backing are scattered in all upward directions with distribution function $S(\theta)$, where θ is the polar angle. If scattering is perfectly Lambertian, $S(\theta) \propto \cos\theta$. Further, let us call $f_{\uparrow}(\theta)$ the flux density of photons in the film near the textured surface, which are traveling up at angle θ. Due to symmetry, $f_{\uparrow}$ depends only on θ. Also, let $f_{\downarrow}(\theta)$ be a flux of photons in the film near the film/glass interface, which are traveling down at angle θ. In the same manner, $g_{\uparrow}(\chi)$ and $g_{\downarrow}(\chi)$ are defined as the photon flux densities in the glass at the film/glass interface going up and

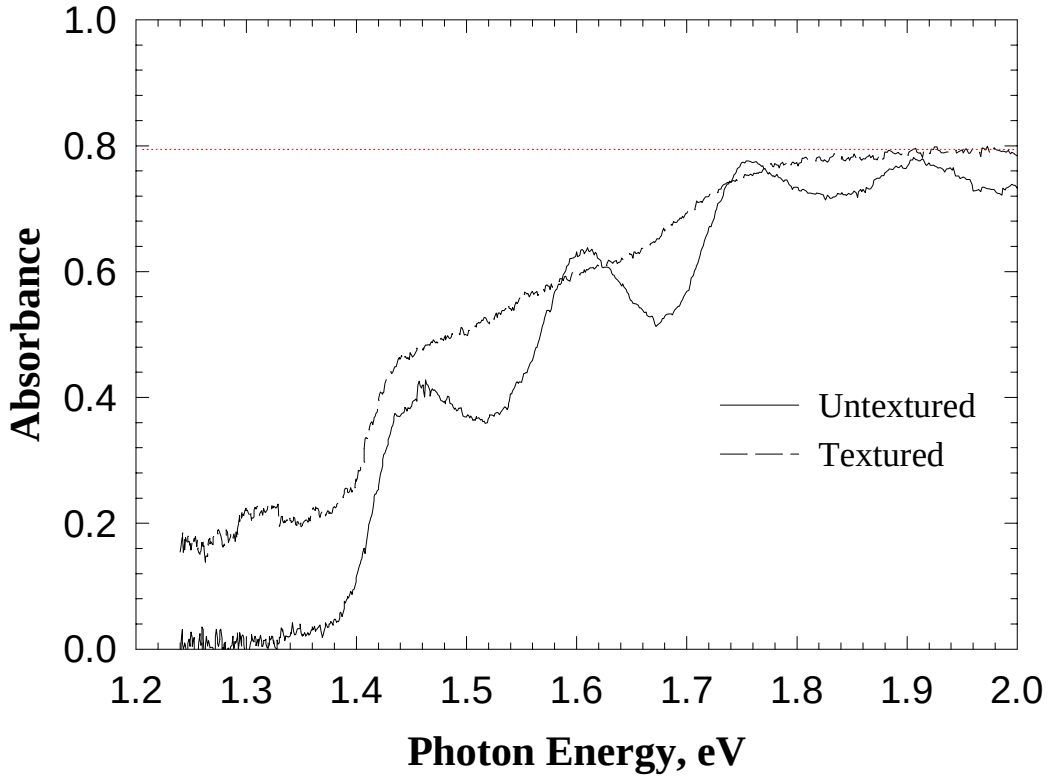

Figure B3: Sample with the sparse distribution of spheres. The light trapping absorption enhancement effect is minimal.

at the glass/air interface going down, respectively (Fig. 2). Reflection at the glass/air boundary gives a relation between $g_{\uparrow}(\chi)$ and $g_{\downarrow}(\chi)$:

$$g_{\downarrow}(\chi)=R_{ag}(\chi)g_{\uparrow}(\chi)\ , \qquad (2)$$

where $R_{ag}(\chi)$ is the reflection coefficient at the glass/air boundary given by the Fresnel formulae. Detailed balance at the glass/film interfaces results in the following relation:

$$g_{\uparrow}(\chi) = f_{\uparrow}(\theta)\exp(-\alpha d/\cos\theta)T_{fg}(\theta) + g_{\downarrow}(\chi)R_{fg}(\theta)\ , \qquad (3)$$

where χ and θ are related by Snell's law. This formula simply states that flux aimed upward in the glass is formed by reflection of photons in the glass from the film/glass

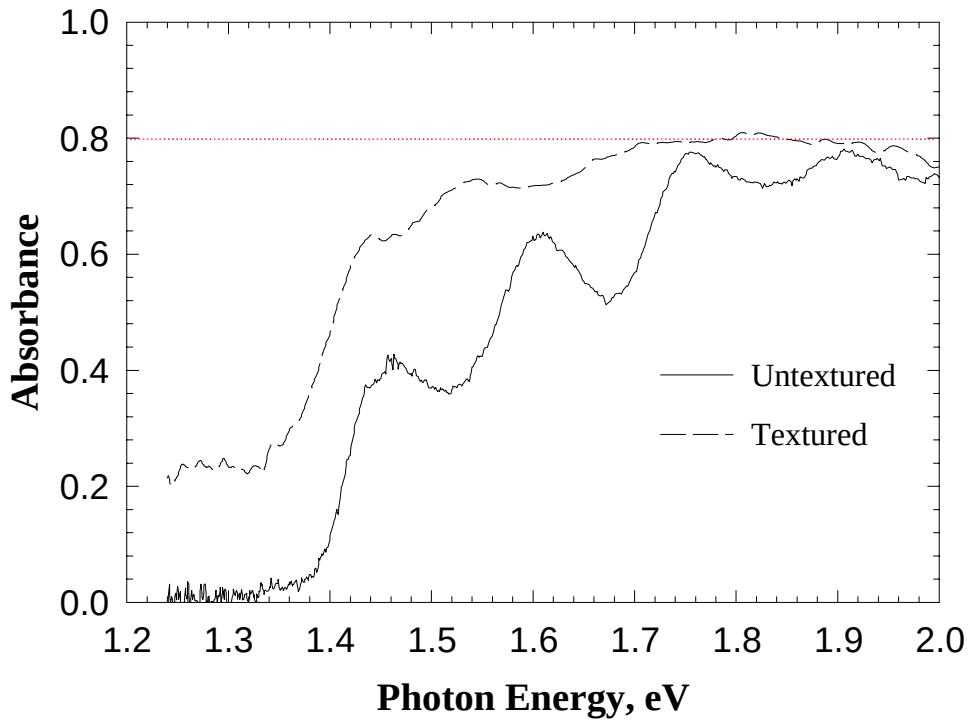

Figure B4: Sample with 50% of the surface area covered with spheres. A large absorption enhancement is obtained near the band edge.

boundary and by transmission of the film photon flux, attenuated in the absorbing film, through the same boundary. The same reasoning provides another relation for f↓(θ) in the semiconductor film: $f_{\downarrow}(\theta) = f_{\uparrow}(\theta)\exp(-\alpha d/\cos\theta)R_{fg}(\theta) + g_{\downarrow}(\chi)T_{fg}(\theta)$.

(4)

Also, the upward photon flux at the bottom surface is formed by the scattering of incoming flux and the downward flux of photons on the textured surface. If a monochromatic photon flux of intensity I is incident on the glass surface, to a good approximation $IT_{ag}(0)T_{fg}(0)(1+R_{fg}(0)R_{ag}(0))$ is transmitted into the semiconductor, and photon flux that reaches the textured surface has intensity

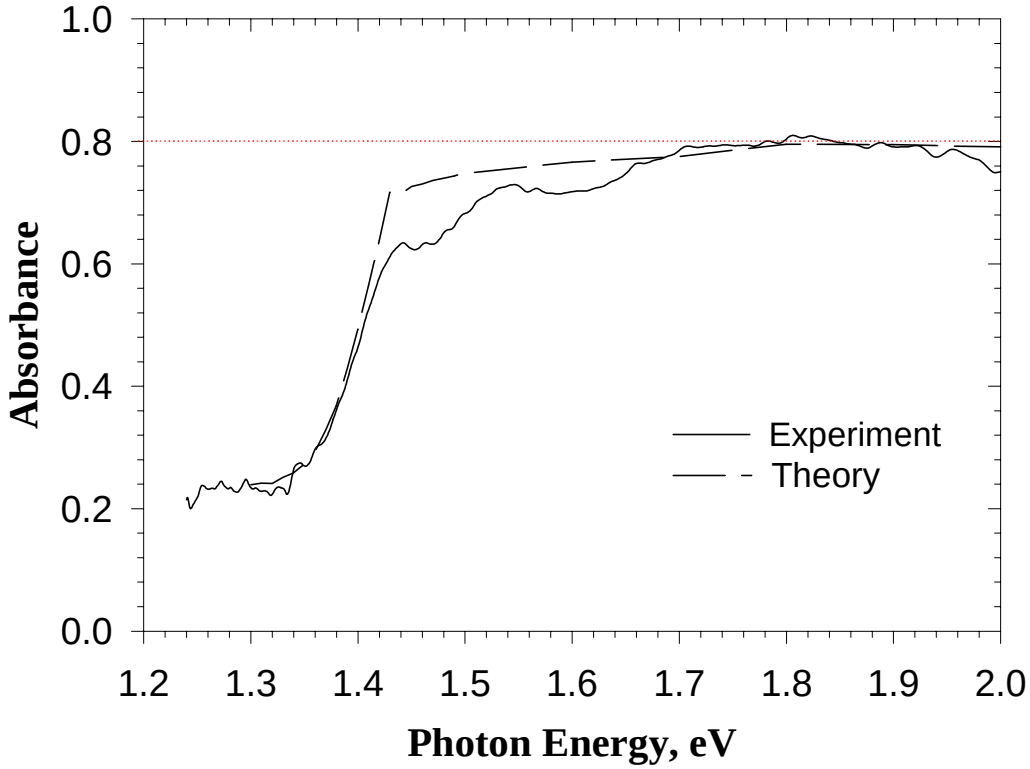

Figure B5: Comparison between the theoretical absorption for an optically textured film and the best values obtained experimentally.

$$I_{tx} = IT_{ag}(0)T_{fg}(0)(1+R_{fg}(0)R_{ag}(0))\exp(-\alpha d/\cos\theta),$$

(5)

Since there is no absorption on the bottom surface, the incoming flux must totally balance the outgoing flux. This gives the final equation for the system:

$$\int f_{\uparrow}(\theta)\cos\theta d\Omega = I_{tx} + \int f_{\downarrow}(\theta)\exp(-\alpha d/\cos\theta)\cos\theta d\Omega,$$

(6)

where integration is performed over 2π steradian. These equations can be solved for any assumed angular distribution of light scattering $f_{\uparrow}(\theta)=S(\theta)$ by integration of Eq. 6

over the solid angles. In the photon gas model in the work of Deckman *et al*[43], an average Lambertian length for absorption is used. This is not valid for the strongly nonlinear dependence of absorption on the propagation angle. Our theory, being more general, explicitly takes into account absorption of photons scattered at different angles. Instead of assumption of totally randomized photons, the model can deal with any angular dependence of scattering, such as Lambertian in this paper. It can also accommodate a dependence on incoming beam incidence angle. Instead of treating the freestanding film, the sample is treated as bonded on the glass or sapphire slide, thus taking into account a practical problem of the light trapping in the supporting slide.

Given this photon gas model, the amounts of reflected and absorbed light can be calculated. Knowing the absorption spectrum of the film and its dispersion, one can obtain the full spectral dependence of absorbance of the textured semiconductor film bonded to a glass slide. Since the samples we studied contained various $Al_xGa_{1-x}As$ alloy layers, the absorption coefficient α and the refractive index n_f in the above formulas are average values weighted by the thickness of the corresponding layers. The calculated absorbance dependence for perfect Lambertian texturing is presented in Figure 5 along with the experimental curve. Two curves show good agreement leading us to believe that in the samples which have approximately 50% of the surface area covered by 0.25μm high mesas at least 90% perfect light randomization has been achieved.

We have studied light randomization and absorption in AlGaAs films textured by means of natural lithography. A reproducible thin film fabrication process was

developed that provides 90% of ideally predicted band-edge absorption relative to our theoretical model. Since the 1μm diameter spheres are visible in the optical microscope, natural lithography with this sphere size is easy to monitor and optimize. Our technique is applicable for fabrication of thin film solar cells and LED's based on III-V compounds. Epitaxial lift-off technology allows us to fabricate very thin AlGaAs solar cells[47], making them lighter and cheaper and providing higher operating point voltages.

Apendix C: Some solutions of the diffusion equation.

We list here solutions of the diffusion equation, which we used to model carrier distribution profile in different configurations.

I. Collection efficiency. We consider a case when the incident light with photon flux density J is all absorbed in the cap region close to the surface characterized by the surface recombination velocity S and has to diffuse into the active region as in Fig C1. A situation like that takes place in the GaN experiment with a thin cap layer. The cap thickness is L, diffusion constant in the cap layer is D and recombination constant in the cap is τ. We define the diffusion length $L_d = \sqrt{\tau D}$ and diffusion velocity $v_d = \sqrt{D/\tau}$. The table below summarizes carrier distribution profiles and collection efficiency for some simple yet important cases:

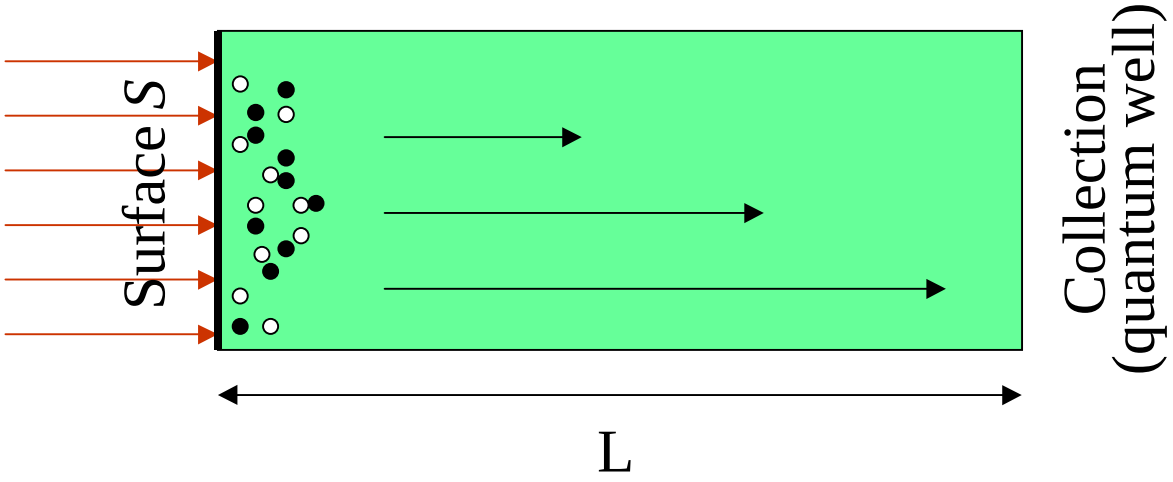

Figure C1: The carriers are generated close to the surface with surface recombination velocity S and diffuse towards the quantum well

	L>>L_d	L<<L_d
S<<v_d	η_{coll}~0 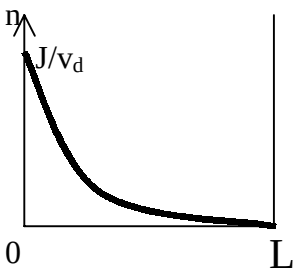	$\eta_{coll} = \frac{1}{1+\frac{L}{L_d}\frac{S}{v_d}}$ 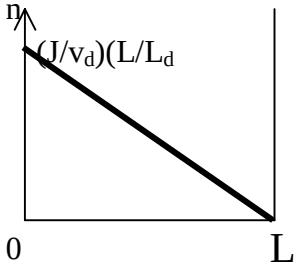
S>>v_d	η_{coll}~0 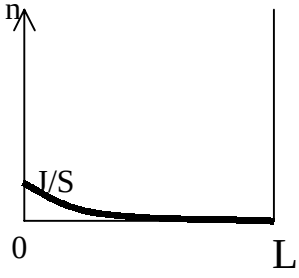	$\eta_{coll} = \frac{1}{1+\frac{L}{L_d}\frac{S}{v_d}}$ 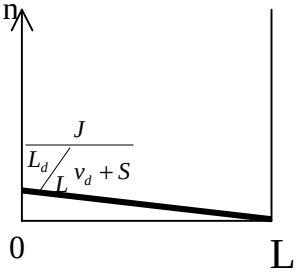

Table C1: Carrier distribution profiles n(x) and the corresponding collection efficiencies corresponding to the flux J absorbed close to the surface with surface recombination velocity S. The cap layer of thickness L is characterized by the lifetime τ and diffusion constant D. We introduce diffusion length $L_d = \sqrt{\tau D}$ and diffusion velocity $v_d = \sqrt{D/\tau}$.

II Internal Quantum Efficiency. We consider a case when the incident light with uniform photon flux density J is all absorbed in the active region as shown in figure C2. The photo-induced electron-hole pairs can either recombine radiatively at the exposed surface characterized by the surface recombination velocity S or radiatively in the active region. The active region thickness is L, the diffusion constant in the cap layer is D and the radiative recombination lifetime in the active region is τ. As before, we define the

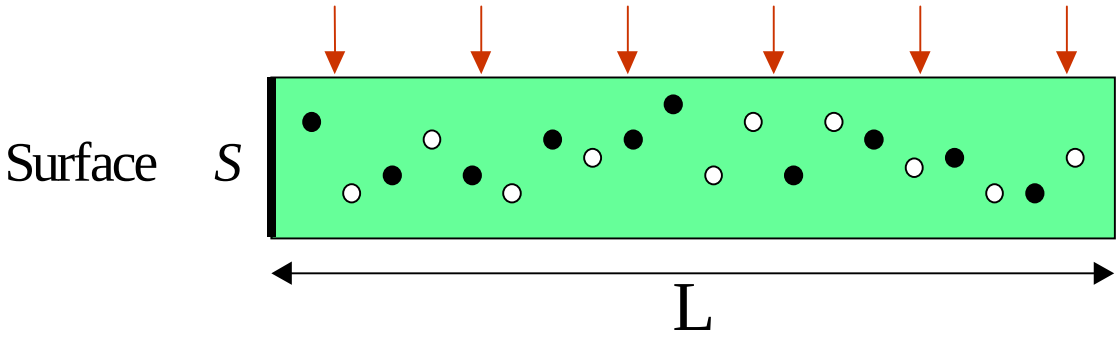

Figure C2: Carrier are injected uniformly, and can either recombine radiatively in the bulk or non-radiatively at the surface.

diffusion length $L_d = \sqrt{\tau D}$ and diffusion velocity $v_d = \sqrt{D/\tau}$. Carrier distribution profiles and corresponding internal quantum efficiencies are summarizes in the table C2 on the following page. All results can be readily used for the case with two open surfaces, e.g. InGaAs experiment, if surface recombination velocity S is substituted by 2S to reflect the presence of two open surfaces.

Table C2	$L>>L_d$	$L<<L_d$
$S<<v_d$	$\eta \sim 1$ 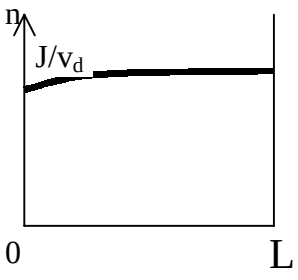	$\eta = \frac{1}{1+\frac{L}{L_d}\frac{S}{v_d}}$ 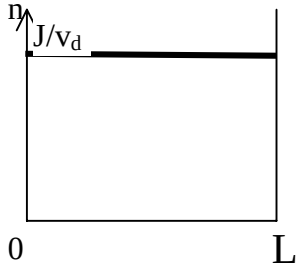
$S>>v_d$	$\eta = \frac{1}{1+\frac{L_d}{L}}$ 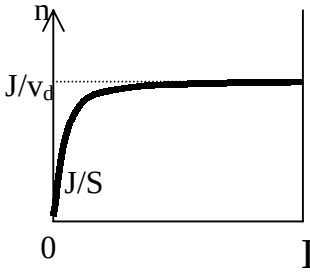	$\eta = \frac{1}{1+\frac{L}{L_d}\frac{S}{v_d}}$ 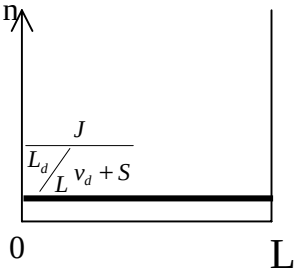

Table C2: Carrier distribution profiles n(x) and the corresponding collection efficiencies corresponding to the flux J absorbed uniformly in the active region with an open surface with surface recombination velocity S. The cap layer of thickness L is characterized by the lifetime τ and diffusion constant D. We introduce diffusion length $L_d = \sqrt{\tau D}$ and diffusion velocity $v_d = \sqrt{D/\tau}$.

References:

[1] P. Selenyi, Phys. Rev. **56**, 477-480 (1939)

[2] R.G.Hulet, E.S. Hilfer, D. Kleppner, Phys. Rev. Lett, **59**, 2955 (1955)

[3] E.M. Purcell, Phys. Rev. **69**, 681(1946)

[4] P. Goy, J.M. Raimond, M. Gross, S. Haroche, Phys. Rev. Lett. **50,** 1903 (1983)

[5] J. Gérard, B. Sermage, B. Gayral, B. Legrand, E. Costard, V. Tierry-Mieg, "Enhanced spontaneous emission by quantum boxes in a monolithic optical microcavity, "*Phys. Rev. Lett.*, 1998, 91(5), pp. 1110-1113.

[6] E. Yablonovitch, 'Inhibited spontaneous emission in solid-state physics and electronics,' *Phys. Rev. Lett.*,1987, **58** (20), pp. 2059-2062.

[7] Schubert, F., Wang, Y.-H., Cho, A.Y., Tu, L.-W., Zydzik, G.J.: 'Resonant cavity light-emitting diode,' *Appl. Phys. Lett.*, 1992, **60** (8), pp. 921-923.

[8] De Neve, H., Blondelle, J., Baets, R., Demeester, P., Van daele, P., Borghs, G.: 'High efficiency planar microcavities LEDs', International Conference on Physics of Semiconductors (ICPS), July 1996, Berlin, Germany.

[9] P. Milonni, 'The quantum vacuum: an introduction to quantum electrodynamics' (Academic Press, Boston, 1994).

[10] E.M. Purcell, 'Spontaneous emission probabilities at radio frequencies,' *Phys. Rev.*, 1946, **69**, pp. 681-686.

[11] M. Boroditsky, R. Coccioli, E. Yablonovitch, 'Analysis of photonic crystals for light emitting diodes using the finite difference time domain technique,' Photonics West 1998, January 28-29, 1998, San Jose, CA.

[12] J. Foresi, P. R. Villeneuve, J. Ferrera, E. R. Thoen, G. Steinmeyer, S. Fan, J. D. Joannopoulos, L. C. Kimerling, H. I. Smith, E. P. Ippen, 'Photonic-bandgap microcavities in optical waveguides,' *Nature* **390,** 6656, pp.143-145 (1997).

[13] The mode volume given in [12] is twice as large due to a different definition. We chose the definition in Eq. (26) as it agrees with the implicit definition given in Purcell, Ref. 10.

[14] K. Sakoda, "Numerical study on localized defect modes in two-dimensional triangular photonic crystals," *Journal of Appl. Phys.*, 1998, **84**(3), pp. 1210-1214.

[15] O. Painter, J. Vuckovic, A. Scherer, "Defect modes of a two-dimensional photonic rystal in a optically thin dielectric slab," to be published in *JOSA A*.

[16] G. Mur, 'Absorbing Boundary Conditions for the Finite-Difference approximation of the time-domain electromagnetic-field equations,' *IEEE Trans. Eletromagnetic Comp.*, 1991, **23** (4), pp. 377-382.

[17] S. Gedney, 'An anisotropic perfectly matched layer-absorbing medium for the truncation of FDTD-Lattices,' *IEEE Trans. Antennas Propagat.*, 1996, **44** (12), pp. 1630-1639.

[18] J.-P. Berenger, 'A perfectly matched layer for the absorption of electromagnetic waves,' *J. Comp. Phys.*, 1994, **114** (2), pp.185-200.

[19] S.Fan, P.Villeneuve, J.Joannopoulos, E.F. Schubert,' *Phys. Rev. Lett.*, 1997, **78**, pp. 3295-3298.

[20] M. Boroditsky, E. Yablonovitch, "Photonic crystals boost light emission", *Physics World*, 1997, **7**, pp. 53-54.

[21] R. De Smedt, 'Correction due to a finite permittivity for a ring resonator in free space,' *IEEE Transactions on Microwave Theory and Techniques*, 1984, **MTT-32**, (10), pp. 1288-1293.

[22] E. Yablonovitch, "Statistical Ray Optics", J. Opt. Soc. Am **72**(7), 1982, pp. 899-907

[23] H.R. Stuart, D.G. Hall, "Thermodynamic limit to light trapping in planar structures J. Opt. Soc. Am A, **14(**11), pp.3001-8.

[24] S. Keller, B. Keller, H. Maui, D. Kapolnek, A. Abare, U.Mishra, L. Coldren, and S. DenBaars, International Symposium on Blue Lasers and Light Emitting Diodes, Chiba University, Chiba, Japan, 1996

[25] C. Reese, M. Boroditsky, E. Yablonovitch, S. Keller, B.Keller, S. DenBaars, "Absolute internal quantum efficiency of InGaN/GaN quantum wells", 1996 CLEO Conference, Technical Digest, Anaheim, California, p. 141.

[26] J.F. Muth, J.H. Lee, I..K. Shmagin, R.M. Kolbas, H.C. Casey, B,P .Keller, U.K. Mishra, S.B. DenBaars, "Absorption coefficient, energy gap, exciton binding energy, and recombination lifetime of GaN obtained from transmission measurements," Appl. Phys. Lett. **71,** pp. 2572-2574 (1997); D. Brunner, H. Angerer, E. Brustarret, F. Freudenberg, R. Hopler, R. dimitrov, O. Ambacher, M. Stutzmann, "Optical Constants

of epitaxial AlGaN films and their temperature dependence," J. Appl. Phys., **82**, pp5090-96 (1997).

[27] I. Eliashevich, Y. Li, A. Osinsky, C. Tran, M. Brown, R. Karlicek, "InGaN blue light-emitting diodes with optimized n-GaN layer," to be published in Proc. Photonics West, Jan 23-29, 1999.

[28] E.Yablonovitch, T.J.Gmitter, R.Bhat, "Inhibited and enhanced spontaneous emission from optically thin AlGaAs/GaAs double heterostructures," Phys. Rev. Lett. **61**(22), pp. 2546-9 (1988).

[29] S.J.Pearton, F Ren; W.S.Hobson, C.R Abernathy; U.K. Chakrabarti, "Effects of wet and dry etching and sulphide passivation on surface recombination velocities of InGaPp-n junctions," Proc. IEEE 6th International Conference on Indium Phosphide and Related Materials, NewYork, USA: IEEE, 1994. p.186-9.

[30] M.Boroditsky, E.Yablonovitch, "Photonic crystals boost light emission", Physics World No. 7, 1997 pp.53-54.

[31] A. J. Nelson and R. G. Sobers, J. Appl. Phys. 49, 6103 (1978).

[32] "Ultra-High Spontaneous Emission Quantum Efficiency, 99.7% Internally and 72% Externally, From AlGaAs/GaAs/AlGaAs Double Heterostructures" I. Schnitzer, E. Yablonovitch, C. Caneau, and T. J. Gmitter, Appl. Phys. Lett. 62, 131 (1993).

[33] W. N. Carr and G. E. Pittman, Appl. Phys. Lett. 3, 173 (1963).

[34] E. Yablonovitch, J. Opt. Soc. Am. 72, 899 (1982). E. Yablonovitch and G. D. Cody, IEEE Trans. Elec. Dev. ED-29, 300 (1982).

[35] M. Green, M. Garcia-Parajo, F. Khaleque, and R. Murray, Appl. Phys. Lett. 62, 264 (1993).

[36] W. B. Joyce, R. Z. Bachrach, R. W. Dixon, and D. A. Sealer, J. Appl. Phys. 45, 2229 (1974).

[37] I. Schnitzer, E. Yablonovitch, C. Caneau, T.J Gmitter, J.Appl. Phys. Lett. 62, 131 (1993).

[38] "Very High-Efficiency Semiconductor Wafer-Bonded Transparent Substrate (AlGa)InP/GaP Light-Emitting Diodes", F. A. Kish, F. M. Steranka, D. C. DeFevere, D. A. Vanderwater, K. G. Park, C. P. Kuo, T. D. Osentowski, M. J. Peanasky, J. G. Yu, R. M. Fletcher, D. A. Steigerwald, M. G. Craford, and V. M. Robbins, Appl. Phys. Lett. 64, 2839 (1994).

[39] J. Pankove "Optical processes in semiconductors", Dover Publications, New York, 1975.

[40] Deckman, J.N. Dunsmuir, "Natural lithography," Appl. Phys. Lett **41**, 377-379 (1982)

[41] H.Stewart, D. Hall, "Absorption enhancement in silicon-on-insulator waveguides using metal island films," Appl. Phys. Lett **69,** 2327-29 (1996)

[42] A. Krotcus. V. Pacebutas, J. Kavaliauskas, I. Subacius, K. Grigoras, I. Simkiene, "Light trapping effect in silicon wafers with anodically etched surfaces", Applied physics A, **64**, pp.357-60, Springer-Vesrlag, April 1997.

[43] H.W.Deckman, C.R.Wronsky, H.Witzke, E.Yablonovitch, “Optically enhanced amourphous silicon solar cells,” Appl. Phys. Lett. **42**, 968-970(1982),

[44] P.M. van den Berg, T.J.Fokkema, “The Rayleigh hypothesis in the theory of reflection by a grating,” J.Opt.Soc.Am. **69**,27-31(1979).

[45] A.G.Voronovitch, Sov. “Small slope approximation in wave scattering by rough surfaces”, Sov. Phys. JETP 62, 65-70(1985).

[46] E. Yablonovitch, R. Gmitter, J.P.Haribson, R.Bhat “Extreme selectivity in the epitaxial lift-off GaAs films“, Appl. Phys. Lett. **51**, 2222-24(1987).

[47] X.Y.Lee, A.K.Verma, C.Q.Wu, M.Goertemiller, E.Yablonovitch, ”Thin film GaAs solar cells on glass substrates by epitaxial lift-off”, Procedings of 25th PVSC, May 13-17 1996, Washington D.C., pp.53-55.